

Probing the microwave response of novel Josephson elements

Inauguraldissertation

zur
Erlangung der Würde eines Doktors der Philosophie
vorgelegt der
Philosophisch-Naturwissenschaftlichen Fakultät
der Universität Basel

von

Roy Haller
aus Basel BS, Schweiz

Basel, 2021

Genehmigt von der Philosophisch-Naturwissenschaftlichen Fakultät
auf Antrag von
Prof. Dr. Christian Schönenberger
Prof. Dr. Martino Poggio
Prof. Dr. Attila Geresdi
Prof. Dr. Cristian Urbina

Basel, 15.10.2021

Prof. Dr. Martin Spiess
Dekan

Widmung

Diese Arbeit widme ich meiner geliebten Freundin Claudia für ihre stetige und immerwährende Unterstützung.

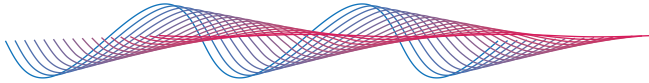
Contents

1. Theoretical Concepts	1
1.1. Superconductivity	1
1.1.1. Cooper pairs	1
1.1.2. Superconducting gap	2
1.1.3. Penetration depth and coherence length	3
1.2. Josephson junctions	4
1.2.1. Josephson effect	5
1.2.2. Andreev reflection	7
1.2.3. Andreev bound states	9
1.2.4. Current-phase relation	12
1.2.5. Josephson inductance	15
1.2.6. RCSJ-model	16
2. Probing the Josephson effect	21
2.1. Shapiro steps	21
2.2. Josephson radiation	24
2.3. rf SQUID	25
2.3.1. Phase-biasing	25
2.3.2. Screening effect	26
2.3.3. Inductive coupling to a resonator	28
2.4. Detecting Majorana bound states	28
3. Device Fabrication and Design	33
3.1. SIS tunnel junctions	34
3.2. SNS junctions	37
3.2.1. Cd_3As_2 junctions	37
3.2.2. InAs junctions	38
3.2.3. Graphene junctions	40
3.3. $\lambda/4$ -resonator	41
3.3.1. NbTiN sputtering	41
3.3.2. Design and patterning	42
3.4. RF SQUID loop	43
4. Measurement set-up	45
4.1. Preface	46

4.2.	Josephson radiation and Shapiro step set-up	46
4.2.1.	Optimizations	50
4.2.2.	Possible future improvements	52
4.3.	Reflectometry set-up	55
4.3.1.	Bonding	56
4.3.2.	Read-out	57
4.3.3.	Magnetic field pick-up	60
5.	Phase-dependent microwave response of a graphene Josephson junction	61
5.1.	Introduction	62
5.2.	Device structure	63
5.3.	Reflectometry	64
5.4.	Circuit model	66
5.5.	Current-Phase relation	68
5.6.	Phase-dependent loss	72
5.7.	Theory of Andreev Bound States	73
5.8.	Comparison with Theory	76
5.9.	Conclusion	79
6.	Josephson Radiation and Shapiro Steps	81
6.1.	Introduction	82
6.2.	SIS junction	84
6.3.	1D nanowire SNS junctions	90
6.3.1.	Cd ₃ As ₂ nanowire Josephson junction	90
6.3.2.	InAs nanowire Josephson junction	96
6.4.	2D/3D SNS junctions	100
6.4.1.	HgTe Josephson junction	100
6.4.2.	WTe ₂ Josephson junction	104
6.5.	Conclusion	108
7.	Conclusion and Outlook	111
	Bibliography	113
A.	Formal description of a $\lambda/4$-resonator	125
A.1.	Loaded $\lambda/4$ -resonator	126
A.2.	Influence of Z_{load} on f_0 and Q_{load}	128
A.2.1.	Inductively coupled load	128
A.2.2.	Consistency proof for analytical expressions	129
A.3.	Unloaded $\lambda/4$ -resonator	133
A.4.	Current within a $\lambda/4$ -resonator	135

B. Fitting routines	139
B.1. Resonance curve fitting	139
B.2. Curve fitting with screening correction	141
C. Temperature dependence of an rf SQUID	145
C.1. Theoretical predication	145
C.2. Experimental results	146
D. Extracting the charge carrier density	149

1 Theoretical Concepts



In this chapter, we describe the key phenomena investigated throughout this thesis, namely superconductivity and the Josephson effect, emerging when two superconductors are brought in close proximity.

1.1. Superconductivity

The phenomena of superconductivity manifests itself by the vanishing electrical resistance for direct current (dc) and the expulsion of magnetic flux in matter. Superconductivity appears in certain materials we call superconductors (e.g. Al, Pb, Nb, MoRe, NbTiN, ...), when cooled below their characteristic critical temperature T_c . In 1911, H. Kamerlingh Onnes discovered superconductivity by the observation of an evanescent resistance in mercury below $T_c = 4.2$ K [1]. The possibility to pass currents without dissipation enabled the development of powerful electromagnets used in magnetic resonance imaging, in particle accelerators or in cryogenic refrigerators for quantum research. Superconductivity is a quantum-mechanical effect, which enlarges as the systems size grows without physical limitation, meaning that the macroscopic wavefunction describing superconductivity extends over the whole superconducting system.

1.1.1. Cooper pairs

In 1957, Bardeen, Cooper and Schrieffer (BCS) introduced a microscopic theory based on an effective attractive interaction between electrons to describe superconductivity [2]. In conventional superconductors (e.g. Al, Ti, Pb, ...) this interaction can be described phenomenologically as follows: An electron moving in a lattice provokes a force on the positively charged lattice-ions, which leads them to be slightly displaced. As a consequence, an other electron in the system is attracted to this increased positive charge density, which results in an effective attractive interaction between the electrons as illustrated



Figure 1.1. Cooper pair formation. (a) A negatively charged electron distorts the positively charged lattice ions. (b) Another electron gets attracted to the increased positive charge density, which leads to an effective attractive interaction between the individual electrons.

in Fig. 1.1. Due to this phonon-mediated interaction, electrons of opposite momentum and spin pair up, and form a so-called Cooper pair. These Cooper pairs merge into a collective many-particle condensate wavefunction, which maintains phase coherence over macroscopic distances [3].

1.1.2. Superconducting gap

In contrast to normal metals, in which the density of states continuously evolves, there is an energy gap appearing for superconductors below T_c . The BCS theory predicts that the density of states for the quasiparticle excitations from the superconducting ground state obeys following relation [4]:

$$N_S(E) = N_F \frac{|E|}{\sqrt{E^2 - \Delta^2}} \theta(|E| - \Delta), \quad (1.1)$$

where the energy E is expressed with respect to the Fermi level E_F of the superconducting condensate, N_F is the density of states at $E = E_F$ when the system is in the normal state and θ is the Heaviside step function. The superconducting gap Δ defines the energy difference between the condensate and the quasiparticle spectrum, which diverges close to the gap edge as shown in Fig. 1.2. In general, the energy gap is shrinking with increasing temperature and vanishes rapidly around T_c . For the limit $T = 0$ the superconducting gap can be related to the critical temperature as $\Delta = 1.764 \cdot kT_c$, where k is the Boltzmann constant. For Al with a $T_c \approx 1.2$ K one obtains $\Delta_{Al} \approx 180 \mu\text{eV}$ [5].

One finds that for $T = 0$ all quasiparticle states with negative energies are filled, while for $T > 0$ the occupation distribution is given by the Fermi function. This means that beside Cooper pairs, there are always normal electrons present in superconductors as described by the two-fluid model [3]. An external time-varying electromagnetic field will act, on both the Cooper pairs as well as on these normal electrons, where the latter leads to dissipation due to impurity scattering. Consequently, the dissipationless character of superconductors might be valid for dc currents, but dissipation will occur in superconducting devices operating with alternating currents [6].

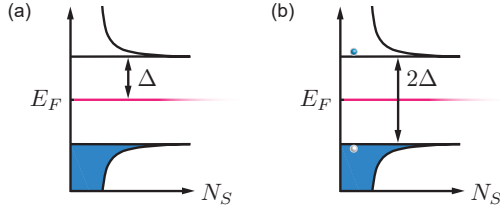


Figure 1.2. Quasiparticle density of states $N_S(E)$ in superconductors. The superconducting condensate (pink) is located at the Fermi level E_F . (a) In the ground state all quasiparticle states with negative energies are occupied. (b) Within the superconducting gap there are no states available for quasiparticles and their excitations (e.g. a single electron-hole pair) need to overcome the energy 2Δ .

1.1.3. Penetration depth and coherence length

The expulsion of magnetic field from the bulk of superconductors, i.e., the Meissner effect [7], is caused by reactive circulating supercurrents which flow on the surface. These currents exactly oppose the external magnetic field such that magnetic field lines are excluded from the bulk of the superconductor. Thus, for small magnetic fields superconductors are perfect diamagnets. The penetration depth λ_p describes the length scale for the exponential decay of the magnetic field. For Al the penetration depth reads $\lambda_p \approx 20$ nm [8].

The coherence length ξ is another important length scale to describe superconductors. It measures the distance for which the complex pseudowave function as introduced in the Ginzburg-Landau theory [9], regains its bulk gap value from a local region of suppressed superconductivity, occurring for example when a superconductor is contacted by a normal metal. In a microscopic picture, ξ can be interpreted as the averaged distance between the electrons of a Cooper pair. The coherence length in a pure superconductor is given by [4]

$$\xi = \frac{\hbar v_F}{\pi \Delta}, \quad (1.2)$$

where \hbar is the reduced Planck constant and v_F is the Fermi velocity. For Al, where $v_F = 2 \times 10^6$ ms⁻¹ and with the superconducting gap given in Sec. 1.1.2, one finds $\xi \approx 2$ μm. Note that the coherence length (counter-intuitively) increases as the superconducting gap decreases, (e.g., $T \rightarrow T_c$). If the superconductor is in the diffusive limit, which is the case when the elastic scattering mean-free path $l_{\text{mfp}} \ll \xi$, the coherence length reduces to

$$\xi_d = \sqrt{\frac{\hbar D}{2\Delta}}, \quad (1.3)$$

where $D = v_F l_{\text{mfp}}/2$ is the diffusion coefficient. The typical mean-free path $l_{\text{mfp}} \approx 100$ nm in Al yields a reduced coherence length $\xi_d \approx 500$ nm.

Ginzburg-Landau parameter

The ratio between the penetration depth and the coherence length defines the Ginzburg-Landau parameter:

$$\kappa = \frac{\lambda_p}{\xi}. \quad (1.4)$$

It was found by Abrikosov in 1957 [10] that superconductors exposed to magnetic fields behave radically different depending on whether κ is smaller or larger than $1/\sqrt{2}$. Superconductors with $\kappa < 1/\sqrt{2}$ are classified as type I, whereas for $\kappa > 1/\sqrt{2}$ they are assigned as type II.

For type I superconductors (e.g. Al, Ti, Pb, ...) the bulk is free from magnetic flux up to a critical magnetic field B_c . Similar to exceeding the critical temperature, superconductivity fully breaks down for $B > B_c$. The critical field for bulk Al reads $B_c \approx 10$ mT.

In contrast, type II superconductors (e.g. MoRe, Nb, NbTiN, ...) exhibit two phase-transitions: one at B_{c1} and another at larger magnetic fields B_{c2} . For $B < B_{c1}$, type II superconductors behave as perfect diamagnets similar to the type I materials. However for $B_{c1} < B < B_{c2}$ the bulk is penetrated by units of flux corresponding to a single flux quantum:

$$\Phi_0 = \frac{h}{2e} = 2.068 \times 10^{-15} \text{ Wb}, \quad (1.5)$$

where h is the Planck constant, and e is the electron charge. These so-called flux vortices are screened by local circulating supercurrents and are homogeneously distributed over the superconductor. The vortex density increases with increasing field strength while superconductivity fully breaks down when $B > B_{c2}$.

1.2. Josephson junctions

A Josephson junction (JJ) is defined as a weak link between two superconducting electrodes (S). These weak links can be formed by embedding a thin insulating layer (I), a short normal-conducting region (N) or a constriction (c) between two superconductors as illustrated in Fig. 1.3. All of these different architectures allow the flow of a supercurrent across the junction, even though the superconducting leads are actually interrupted or quenched. This miraculous effect is named after its discoverer B. D. Josephson [11], who theoretically predicted the phenomena in 1962.



Figure 1.3. Three different types of Josephson junctions: (a) SIS-junction, where often the intrinsic oxide layer of the material is used as a barrier, for example Al and AlO_2 . (b) SNS-junctions can be formed by incorporating a short normal metal or semiconductor section. (c) ScS-junctions are formed, when the dimensions of the constrictions are much smaller the coherence length.

In this section, we describe the diverse and astonishing electrical properties of JJs, which are the key for novel applications such as: **parametric amplifiers** (SIS) [12, 13], **single photon source** (SIS) [14], **microwave lasers** (SIS) [15], **superconducting qubits** (SIS) [16–18], **tunable microwave cavities** (SIS) [19], **voltage-standard devices** (SIS) [20], **magnetometers** (ScS) [21], **microwave bolometers** (SNS) [22, 23], to list just a few.

The dominant use of SIS-junctions in superconducting circuits is likely due to their high reproducibility and low dissipation. On the other hand, SNS-junctions consisting of semiconducting materials allow in-situ tuning of the coupling strength between the superconducting leads by electric gate-fields [24], whereas for ScS-junctions in break-junction configurations, highly transparent single channel JJs can be achieved [25].

1.2.1. Josephson effect

In order to get an intuitive understanding for the electrical properties of JJs, we will briefly follow a phenomenological approach [4]. We make use of the fact that the quantum-mechanical behaviour of a superconducting system can be treated as a complex wavefunction; one side of the junction is described by $\psi_1 = \sqrt{n_1}e^{i\varphi_1}$ and the other side by $\psi_2 = \sqrt{n_2}e^{i\varphi_2}$, where n_k refers to the density of Cooper pairs and φ_k is the phase argument. Note that both of these variables are time-dependent. If the two wavefunctions overlap, and a potential difference qV drops symmetrically across the junction. We can now relate the two wavefunctions using the Schrödinger equation

$$i\hbar \frac{\partial \psi_1}{\partial t} = \frac{qV}{2} \psi_1 - K \psi_2, \quad (1.6a)$$

$$i\hbar \frac{\partial \psi_2}{\partial t} = -\frac{qV}{2} \psi_2 - K \psi_1, \quad (1.6b)$$

where the constant K determines the coupling between the superconducting electrodes. After substituting the definitions ψ_k , multiplying Eq. 1.6a by $e^{-i\varphi_1}$

and Eq. 1.6b by $e^{-i\varphi_2}$ one obtains for the real part:

$$\frac{\partial n_1}{\partial t} = -2 \frac{K}{\hbar} \sqrt{n_1 n_2} \sin(\varphi), \quad (1.7a)$$

$$\frac{\partial n_2}{\partial t} = 2 \frac{K}{\hbar} \sqrt{n_1 n_2} \sin(\varphi), \quad (1.7b)$$

where $\varphi = \varphi_2 - \varphi_1$ is the phase difference across the junction. For the imaginary part one obtains

$$\frac{\partial \varphi_1}{\partial t} = -\frac{qV}{2\hbar} + \frac{K}{\hbar} \sqrt{\frac{n_2}{n_1}} \cos(\varphi), \quad (1.8a)$$

$$\frac{\partial \varphi_2}{\partial t} = \frac{qV}{2\hbar} + \frac{K}{\hbar} \sqrt{\frac{n_1}{n_2}} \cos(\varphi). \quad (1.8b)$$

DC Josephson effect

We observe from the real part (Eq. 1.7) that $\partial n_1 / \partial t = -\partial n_2 / \partial t$ and that the prefactor for the sine-functions, lets call it \tilde{K} , is a constant. Since, in general, current is proportional to the time derivative of the charge carrier density, we can expect that there is flow of Cooper pairs across the junction and a supercurrent is present. We can infer from Eq. 1.7 that this supercurrent will have the form

$$I_s(\varphi) = I_c \sin(\varphi), \quad (1.9)$$

which is known as the **dc Josephson relation**. Here, I_c is the so-called critical current, which is proportional to \tilde{K} and thus dependent on the properties of the superconductor and the interplay between the wavefunctions.

This demonstrates, that even in the absence of a voltage bias ($V = 0$), there is a phase-dependent supercurrent $I_s(\varphi)$ flowing across the junction. Once the current through the junction exceeds the critical current, for instance by current biasing the JJ with an external source, a voltage starts to appear.

AC Josephson effect

By subtracting Eq. 1.8a from Eq. 1.8b and assuming similar superconducting leads such that $n_1 \approx n_2$, we obtain

$$\frac{\partial \varphi}{\partial t} = \frac{\partial}{\partial t} (\varphi_2 - \varphi_1) = \frac{qV}{\hbar} = \frac{2eV}{\hbar}, \quad (1.10)$$

known as the **ac Josephson relation**, where the latter form corresponds to single Cooper pair transport ($q = 2e$).

We recognize from Eq. 1.10, that once there is a voltage present, the phase evolves in time as $\varphi = 2eVt/\hbar$. The inverse statement, that once the phase

evolves, there will be a voltage drop also holds true. Combining the ac and dc Josephson relation yields

$$I_s = I_c \sin(2\pi f_J \cdot t), \quad (1.11)$$

which describes the appearance of an alternating supercurrent with amplitude I_c and frequency

$$f_J = \frac{2eV}{h}, \quad (1.12)$$

with V the voltage between the superconducting leads. For example, when $V = 1 \mu\text{V}$, the supercurrent will oscillate with $f_J = 483.9 \text{ MHz}$. In general, the frequency depends on the effective charge q^* transferred across the junction ($f_J = q^*V/h$) and obviously on the voltage drop. Other than that, the Josephson frequency is purely defined by fundamental constants via the electron charge e and the Planck constant h . The fact that JJs convert a constant voltage bias to oscillating currents, makes these elements to highly non-linear objects in superconducting circuits.

Although this simplified derivation for the Josephson effects might provide a qualitative understanding in terms of overlapping wavefunctions, the description is not universal for all JJ flavors. The treatment above will exclusively specify the electrical properties of SIS-junctions. In order to describe SNS/ScS-junctions, a more elaborate approach is needed as will be discussed in the following.

1.2.2. Andreev reflection

In 1964, A. F. Andreev theoretically investigated the scattering properties at the interface between a superconductor (S) and a normal material (N) [26].

A conventional reflection at the interface would describe that an incident electron with energy E located within the superconducting gap retro-reflects again as an electron. This reflection of the electron is due to the absence of accessible quasiparticle states within the gap. Such a process is depicted in Fig. 1.4(a) and implies that there is no net-current across the interface.

However, what Andreev found is that normal currents in N can be converted to supercurrents in S. The microscopic process explaining this phenomena involves a so-called Andreev reflection, which is illustrated in Fig. 1.4(b): An electron with energy E impinging the gap interface forms a Cooper pair by recombination with a second electron at energy $-E$ of opposite spin and momentum. At the same time, a hole retro-reflects such that charge and momentum are conserved. The hole follows the trajectory of the incident electron and possesses its opposite spin. Additionally, the wavefunction of the retro-reflected hole picks up a phase $\varphi_{e \rightarrow h}(E, \varphi_k)$, which depends on the energy E of the incident electron and on the phase argument φ_k of the superconducting wavefunction.

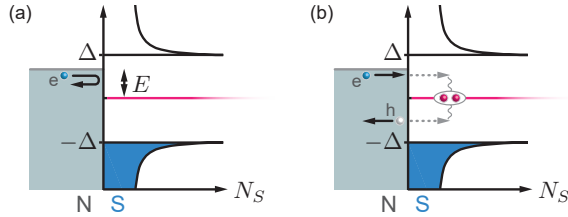


Figure 1.4. Reflection processes at an NS-interface. For electrons with $|E| < |\Delta|$ no quasiparticle states are available in the superconductor and the impinging electron is reflected. (a) Normal reflection: The electron reflects back to the normal metal region. (b) Andreev reflection: The incident electron forms a Cooper pair in the superconductor by the retro-reflection of a hole in the normal metal region and thus a net-current with $2e$ -granularity flows.

Superconducting proximity effect

Through time-reversal symmetry, the process sketched above is reversible: an impinging hole and a retro-reflected electron therefore result in the absorption of a Cooper pair in the normal contact. Consequently, Cooper pairs ‘leak’ into the normal conductor in the form of electron-hole pairs which locally induce superconductivity. This phenomenon is called the superconducting proximity effect. The proximity depth in diffusive normal conducting systems is given by the coherence length $\xi_p = \sqrt{\hbar D / (2\pi kT)}$, which for metals is typically on the order of a few μm .

Finite interface transparency

It was shown by the theoretical work of Blonder, Tinkham and Klapwijk [27], that the interface transparency determines the probability for Andreev reflections. For low transparencies most transfer attempts into the superconducting gap will undergo normal scattering at the interface, resulting in a suppressed conductance across the junction. However, when the normal lead energetically aligns with the quasiparticle continuum, a normal current can flow and hence the superconducting gap can be probed. Conversely, for maximally transparent interfaces the probability for Andreev reflections reaches unity, which results in a doubling of the conductance through the NS-junction for sub-gap conditions when compared to the quasiparticle transport regime outside the gap [28].

1.2.3. Andreev bounds states

We will now consider the device architecture of a normal conducting region embedded between two superconducting leads, thus forming an SNS-junction. In this situation, a supercurrent across the junction is provided by consecutive Andreev reflections at the NS-interfaces. The top part of Fig. 1.5(a) illustrates the transfer of a Cooper pair from the left to the right lead. The Cooper pair coming from the left is converted into a counter-propagating electron-hole pair at the first interface that is recombined to a Cooper pair in the right lead by a subsequent Andreev reflection at the second interface. The total phase acquired in this transfer process reads

$$\varphi_{\text{tot}} = \varphi_{\text{h}\rightarrow\text{e}}(E, \varphi_1) + \varphi_L + \varphi_{\text{e}\rightarrow\text{h}}(E, \varphi_2). \quad (1.13)$$

The first term refers to the phase pick-up at the left interface, the middle term refers to the dynamic phase accumulation while traversing the normal region of length L , and the last term refers to the phase pick-up at the right interface. The interface phase pick-ups depend on the energy E of the coupling electron as well as on the phase arguments of the superconducting wavefunctions, i.e. φ_1 for the left and φ_2 for the right lead and can be determined by matching the S-wavefunctions with the N-wavefunctions at the boundaries. Phase coherence across the junction is maintained, when $\varphi_{\text{tot}} = 0, \pm 2\pi, \pm 4\pi, \dots$. If this condition is satisfied, a so-called Andreev bound state (ABS) is formed, which is a discrete energy sub-gap state [29] that governs the Josephson coupling across the junction [30]. Due to symmetry reasons, ABS always have a partner that reflects the opposite transfer direction as depicted in Fig. 1.5(a).

Short junction limit

In the short junction limit, i.e., when the junction length is much smaller than the proximity depth ($L \ll \xi_p$), the dynamic contribution to the phase can be disregarded ($\varphi_L = 0$). Now, by solving the resonant condition for the phase, one finds that an ABS-pair consists of states with energies [31]

$$E_n^\pm(\varphi) = \pm \Delta \sqrt{1 - \tau_n \sin^2(\varphi/2)}, \quad (1.14)$$

where Δ is the superconducting gap in the leads, $\varphi = \varphi_2 - \varphi_1$ is the phase difference across the junction and τ_n is the transmission probability for a specific transfer channels. The number of possible transfer channels depends on material and the cross-sectional dimensions of the normal region. This can lead to the formation of multiple ABS-pairs, which are enumerated by the index n . One pair component has negative energy E_n^- and the other has positive energy E_n^+ . In Fig. 1.5(b) the ABS spectrum of a JJ with three possible channels of different transparencies is plotted. One recognizes that the mode-specific spectral gap $\delta E_n = E_n^+ - E_n^-$ is 2π -periodic in phase. The

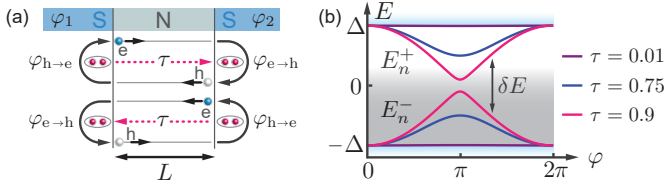


Figure 1.5. Andreev bound state (ABS) formation in an SNS-junction. (a) Schematic illustration of an ABS pair. Charge carriers undergo Andreev reflections at the NS-interfaces. If the total phase acquired within one full circle is a multiple integer of 2π , an ABS is formed. The upper schematic sketches the shuffling of a Cooper pair from the left to the right lead, whereas the lower shows its electron-hole symmetric partner that shuffles a Cooper pair from right to left. The two conditions have opposite energy $E_n^- = -E_n^+$. (b) The energy of an ABS depends on the phase difference $\varphi = \varphi_2 - \varphi_1$ across the junction, the channel transparency τ and the current direction. Here the ABS spectrum of short normal section ($L \ll \xi_p$) with three channels of different transparency is plotted.

spectral gap becomes minimal at $\varphi = \pm\pi \pm 3\pi, \dots$ ($\delta E_n(\pi) = 2\Delta\sqrt{1-\tau_n}$), whereas it is maximally open for $\varphi = 0, \pm 2\pi, \dots$ ($\delta E_n(0) = 2\Delta$). In order to drive an excitation across the spectral gap with a resonator operating at 3 GHz in a junction formed by Al leads with $\Delta = 180 \mu\text{eV} \hat{=} 44 \text{ GHz}$, the channel transparency needs to reach $\tau = 0.995$, which is typically very hard to reach.

Long junction limit

In the long junction limit ($L \geq \xi_p$) the solutions for the ABS energies become more complicated. Since the dynamic phase now needs to be considered, the number of valid ABS solutions for each possible channel, grows as the junction length increases. Additionally, the maximal energy gap of the collective ABS spectrum shrinks to a so-called minigap $E_g < 2\Delta$ [32]. For a long diffusive junction the minigap reads $E_g \approx 3E_T$, where the Thouless energy $E_T = \hbar D/L^2$ is the energy associated to the diffusion time though the normal conducting section [33].

Population

In a semiconductor picture, the ABSs can be viewed as energy levels which need to be populated to activate them as supercurrent carriers. If we consider a short JJ with only one channel, we will find four possible population configurations

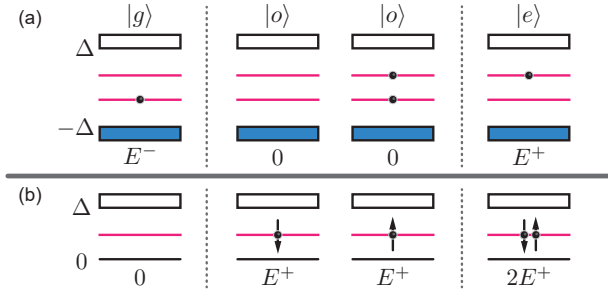


Figure 1.6. Single channel ABS populations. (a) Semiconductor picture. (b) Excitation picture ($+E^+$ compared to the semiconductor picture). (a)-(b) The left state depicts the ground state $|g\rangle$ with even parity. The two middle odd-parity states $|o\rangle$ are energetically degenerate and carry no net-current. The right state illustrates the excited state $|e\rangle$ and has even parity.

as depicted in Fig. 1.6 (a). The population can be equivalently treated as a spin-1/2 system, which is often referred to as the excitation picture as shown in Fig. 1.6 (b).

The ground state $|g\rangle$ with energy $E^- < 0$ and the excited state $|e\rangle$ with energy $E^+ > 0$ have the same parity implying that direct microwave induced transitions can be accessed. However, direct transitions from $|g\rangle$ towards the two odd-states $|o\rangle$ are prohibited due to their opposite parities. In order to change the parity, the coupling to the quasiparticle continuum needs to be involved. Note that the odd-states carry no effective net-current across the junction: In the one case there is no Cooper pair exchanged with the leads at all, whereas in the other case there is Cooper pair transport of equal opposite rate, averaging to a net zero supercurrent. Due to the degeneracy of the odd-states, the four populations reduce to three detectable configurations, which was impressively demonstrated in Refs. [25, 34]. If spin-orbit interaction is considered, the above description gains additional complexity due to the lifting of the odd-states as experimentally observed in InAs-nanowire JJs [35, 36].

If we neglect coupling to the environment, i.e., we assume there is no interaction with a microwave field and no quasiparticle exchange, the system is in equilibrium and the population configuration is limited to the ground and excited state. Due to the fermionic character of the ABSs, the weights are given by the Fermi-function $F(E^-) = 1 - F(E^+)$. In the zero temperature limit $F(E^-) = 1$ and for increasing the electronic temperature T , the weights will balance ($F(E^-) \rightarrow 1/2$), which is especially evident for ABS pairs close to zero energy.

1.2.4. Current-phase relation

In Sec. 1.2.3 we have shown that ABSs are phase-dependent and carry supercurrents across the junction. Now the question arises how much supercurrent they are actually able to provide. The answer to this can be found by making use of the electrical power in the system [31], which for a single ABS (e.g. the n^{th} -ground state) can be expressed as

$$P = \frac{\partial E_n^-}{\partial t} = \frac{\partial E_n^-}{\partial \varphi} \frac{\partial \varphi}{\partial t} = \frac{\partial E_n^-}{\partial \varphi} \frac{2eV}{\hbar} = I_n^- V. \quad (1.15)$$

The time-derivative of the phase is given by the ac Josephson equation (Eq. 1.10) with the charge of a Cooper pair. We can solve the last two terms of Eq. 1.15 for the current and obtain the supercurrent for an individual populated ABS:

$$I_n^\pm(\varphi) = \frac{2e}{\hbar} \frac{\partial E_n^\pm}{\partial \varphi}. \quad (1.16)$$

Consequently, the supercurrent of a single ABS is 2π -periodic in phase. The current is zero at the energy extrema that are located at $\varphi = 0, \pm\pi, \pm 2\pi, \dots$ for a conventional junction.

The total supercurrent I_s across the junction is the sum over all discrete contributions, which are provided by populated ABSs. In thermal equilibrium, the population of the ABS spectrum is given by the Fermi-function. For clarity, we separate the contributions from the E_n^- -states and the E_n^+ -states and we find

$$I_s(\varphi) = \frac{2e}{\hbar} \left[\sum_n \frac{\partial E_n^-}{\partial \varphi} F(E_n^-) + \sum_n \frac{\partial E_n^+}{\partial \varphi} F(E_n^+) \right] \quad (1.17)$$

Since the ABS energies are symmetrically located around the Fermi energy or by virtue the electron-hole symmetry we can state ($I_n^- = -I_n^+$), which reduces the above equation to:

$$I_s(\varphi) = \frac{2e}{\hbar} \left[\sum_n \frac{\partial E_n^-}{\partial \varphi} \{F(E_n^-) - F(E_n^+)\} \right]. \quad (1.18)$$

The combination of the Fermi-functions can be rewritten as

$$F(E_n^-) - F(E_n^+) = 1 - 2F(E_n^+) = 1 - \frac{2}{e^{E_n^+/(kT)} + 1} = \tanh\left(\frac{E_n^+}{2kT}\right). \quad (1.19)$$

With this we can express the total phase-dependent supercurrent that is the current-phase relation (CPR) as

$$I_s(\varphi) = \frac{2e}{\hbar} \sum_n \frac{\partial E_n^-}{\partial \varphi} \tanh\left(\frac{E_n^+}{2kT}\right). \quad (1.20)$$

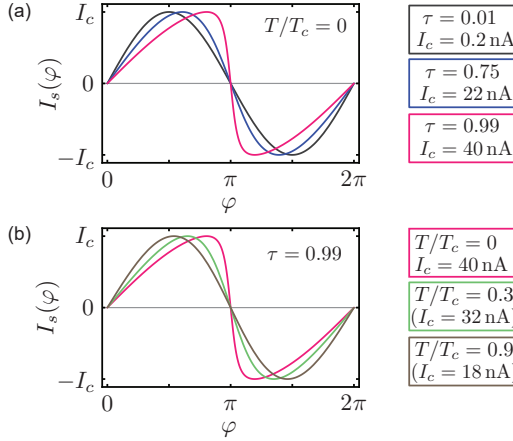


Figure 1.7. Current-phase relation of a single channel JJ in the short junction limit at equilibrium conditions evaluated with Eq. 1.21 and a superconducting gap $\Delta = 180 \mu\text{eV}$. (a) With increasing channel transparency τ , the CPR evolves from a sinusoidal to a forward skewed sinusoidal lineshape and the critical current I_c increases. Here, temperature broadening is neglected. (b) With increasing the electronic temperature the CPR becomes sinusoidal, even for highly transparent channels ($\tau = 0.99$). The critical current values are determined without considering the closing of the gap as the temperature increases.

By substituting the ABS energy given in Eq. 1.14 and evaluating the phase derivatives, one obtains [37]

$$I_s(\varphi) = \frac{e\Delta}{2\hbar} \sin(\varphi) \sum_n \frac{\tau_n}{\sqrt{1 - \tau_n \sin^2(\varphi/2)}} \tanh\left(\frac{\Delta\sqrt{1 - \tau_n \sin^2(\varphi/2)}}{2kT}\right), \quad (1.21)$$

which characterizes the CPR for the short junction limit. In Fig. 1.7 the CPR for a single channel with transparency τ is plotted for different transmissions in (a) and different temperatures T in (b) by considering a superconducting gap $\Delta = 180 \mu\text{eV}$. The CPR is 2π -periodic and is sinusoidal when $\tau \ll 1$ or when T is close to T_c . It becomes forwards skewed at low T for high transmissions and the critical current I_c defined as the maximal amplitude of the CPR increases.

Ambegaokar-Baratoff relation

By taking the limit $\tau_n \rightarrow 0$ in Eq. 1.21 one obtains the Ambegaokar-Baratoff relation [38] for the supercurrent

$$I_s(\varphi) = \frac{\pi\Delta}{2eR_N} \tanh\left(\frac{\Delta}{2k_B T}\right) \sin(\varphi) \stackrel{T \rightarrow 0}{=} \frac{\pi\Delta}{2eR_N} \sin(\varphi), \quad (1.22)$$

the prefactor of the sin-function in the right term can be identified as the zero temperature critical current, which is related to the normal-state conductance via the Landauer formula $G_N = R_N^{-1} = G_0 \sum_n \tau_n$, where $G_0 = 2e^2/h$ is the conductance quantum. The formalism reflects the tunneling limit of the ABS-picture governing the Josephson effect, and reproduces the dc Josephson relation obtained for SIS-junctions (Eq. 1.9).

Diffusive short junction limit

Until now we have consider an ABS spectrum with discrete states. However, when there are many possible ABSs leading to a dense spectrum we can rewrite Eq. 1.21 in the integral form

$$I_s(\varphi) = \frac{e\Delta}{2\hbar} \sin(\varphi) \int_0^1 \rho(\tau) \frac{\tau}{\sqrt{1 - \tau \sin^2(\varphi/2)}} \tanh\left(\frac{\Delta \sqrt{1 - \tau \sin^2(\varphi/2)}}{2kT}\right) d\tau, \quad (1.23)$$

where $\rho(\tau)$ is the distribution function for the transmission probabilities. In the diffusive limit, the distribution of the transmission eigenvalues can be calculated with random matrix theory [39, 40] and is found to be [41]

$$\rho(\tau) = \frac{\pi\hbar G_N}{2e^2} \frac{1}{\tau\sqrt{1-\tau}}, \quad (1.24)$$

which is known as the Dorokhov distribution [42]. As a consequence, for a diffusive system one expects channels with transparencies covering the full interval $\tau = [0, 1]$ to appear, with increased densities for small and large transmission probabilities [43]. This bimodal distribution is illustrated in Fig. 1.8 (a). In this limit, the minimal phase-dependent gap of the ABS spectrum is given by the ABS-pair with largest transparency ($\tau \rightarrow 1$) and hence reads $\delta E = 2\Delta|\cos(\varphi/2)|$. The integral given in Eq. 1.23 with the distribution given in Eq. 1.24 can be evaluated analytically for the zero temperature limit as [44]

$$I_s^{\text{diff.}}(\varphi) = \frac{\pi G_N \Delta}{e} \cos\left(\frac{\varphi}{2}\right) \operatorname{arctanh}\left[\sin\left(\frac{\varphi}{2}\right)\right], \quad (1.25)$$

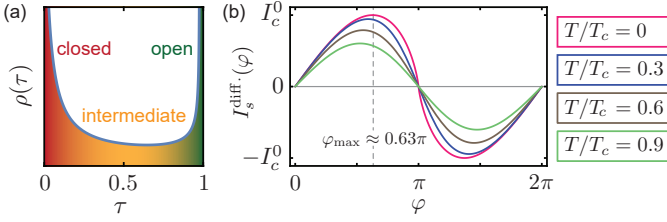


Figure 1.8. Diffusive junction model. (a) The Dorokhov distribution describes a bimodal probability density for channels with transmission τ . The probability peaks for closed and open channels. The illustration is adapted from Ref. [46]. (b) CPR of a short, diffusive junction as a function of temperature. The supercurrent I_c^0 denotes to the critical current at zero temperature. A temperature independent gap is assumed.

where G_N is the normal-state conductance. This relation describes the CPR of a short, diffusive junction at $T = 0$. The critical current in the zero temperature limit can be obtained by finding the maximum of Eq. 1.25 [45]

$$I_c^{\text{diff.}} \approx \frac{1.33 \cdot \pi \Delta G_N}{2e}, \quad (1.26)$$

from which we can estimate a critical current of ~ 380 nA for a normal-state resistance of 1 k Ω and a superconducting gap of 180 μeV . The maximum supercurrent is found at $\varphi_{\text{max}} \approx 0.627\pi$, corresponding to a skewness parameter $S = (2\varphi_{\text{max}}/\pi) - 1 \approx 0.255$. The temperature dependence of the CPR shown in Fig. 1.8 (b) is obtained by numerically solving the integral in Eq. 1.23. Similar to the single mode junction, the critical current and the skewness reduces with increasing temperature.

1.2.5. Josephson inductance

By considering the time derivative of the CPR and making use of the ac Josephson relation (Eq. 1.10)

$$\frac{\partial I_s}{\partial t} = \frac{\partial I_s}{\partial \varphi} \frac{\partial \varphi}{\partial t} = \frac{2e}{\hbar} \frac{\partial I_s}{\partial \varphi} V, \quad (1.27)$$

we observe that JJs effectively behave as inductors. We can identify the inverse Josephson inductance to be [47]

$$L_J(\varphi)^{-1} = \frac{2e}{\hbar} \frac{\partial I_s(\varphi)}{\partial \varphi} = \frac{2\pi}{\Phi_0} \frac{\partial I_s(\varphi)}{\partial \varphi}. \quad (1.28)$$

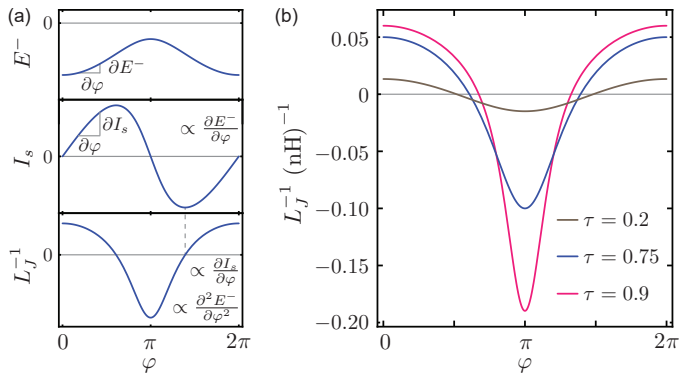


Figure 1.9. Josephson inductance. (a) Relation between the phase-dependence of a single Andreev E^- -state, the CPR (I_s) and the inverse Josephson inductance L_J^{-1} . (b) L_J^{-1} calculated by combining Eq. 1.28 and Eq. 1.21 for a single channel JJ at $T = 0$ with different transparencies and $\Delta = 180 \mu\text{eV}$.

Since the supercurrent is proportional to the change of the ABS energy as a function of phase, L_J^{-1} measures the curvature of the ABS (it contains the second derivative in the phase). The relation between these quantities is illustrated in Fig. 1.9 (a). The phase condition for $L_J^{-1} = 0$ corresponds to maxima in the supercurrent, which move towards $\varphi = \pi/2$ for lower transparencies as seen in Fig. 1.9 (b) while simultaneously, the ratio $|L_J^{-1}(\pi)/L_J^{-1}(0)|$ converges to 1. Both of these observations correspond to an increasingly sinusoidal CPR. To get a feeling for the order of magnitude of this inductance, we consider a sinusoidal CPR with a critical current of 100 nA, for which we obtain $L_J = \hbar/[2eI_c \cos(\varphi)] = 3.3 \text{ nH}$ at $\varphi = 0$.

Since in general, the inductance is a measure for how strongly an electric component opposes time-varying currents, the Josephson inductance becomes evident in ac circuits as we will be experimentally demonstrate in Ch. 5.

1.2.6. RCSJ-model

If the supplied current through a Josephson junction is larger than its critical current, a voltage drop occurs and the ac Josephson effects kicks-in. The crossover from the zero resistance state to the voltage state, and the corresponding electrical response can be described with the RCSJ (resistively can capacitively shunted junction) model [48]. The RCSJ-model models a Josephson junction as joined circuit elements consisting of an ideal JJ shunted by a resistance R and a capacitance C , as depicted in Fig. 1.10(a)-(b). The resis-

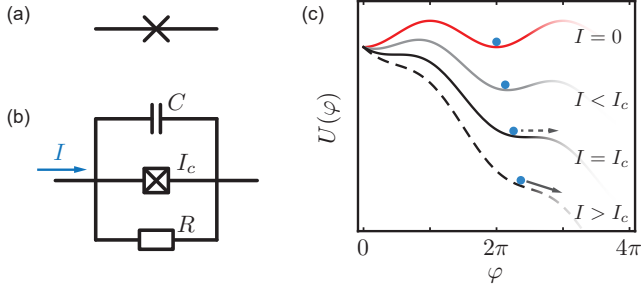


Figure 1.10. RSCJ-model and washboard potential. (a) Circuit symbol of a Josephson junction. (b) In the RSCJ-model a Josephson junction is described as an ideal Josephson element shunted by a resistor R and a capacitor C . (c) The tilt of the washboard potential increases with current bias as illustrated for different current regimes. The phase-particle (blue ball) starts to roll down the potential once the bias current is larger than the critical current ($I \geq I_c$).

tance R characterizes the ‘normal’ dissipation within the system, e.g., due to quasiparticle tunnelling events or an ex-situ shunt resistor. In general, R is dependent on the voltage V across the junction and suffers from thermal noise. However, in the following we will consider R as the normal-state resistance of the junction and treat it as a constant. The capacitance C on the other hand reflects the geometric capacitance between the two electrodes, which is especially prominent in tunnel junctions due to their relatively large geometry.

By assuming a sinusoidal CPR, and by expressing the three available parallel paths for the current using the dc and ac Josephson relations, we obtain

$$I = I_c \sin(\varphi) + \frac{\hbar}{2e} \dot{\varphi} / R + C \frac{\hbar}{2e} \ddot{\varphi}, \quad (1.29)$$

where I is the current bias on the system. The first term is the supercurrent across the Josephson junction, the second term captures the current through the resistor and the last term represents the current through the capacitance. The phase difference φ in this differential equation can be interpreted in a mechanical analogue as a damped motion of a particle with mass $(\hbar/(2e))^2 C$ moving along the φ -axis in an effective potential

$$U(\varphi) = -\frac{\hbar I_c}{2e} \cos(\varphi) - \frac{\hbar I}{2e} \varphi. \quad (1.30)$$

which has a distinct washboard shape which gets more tilted for increasing current bias as illustrated in Fig. 1.10(c). When $I < I_c$, the ‘phase particle’ is

trapped in a minimum of the washboard potential, therefore φ is stationary and hence the voltage drop is zero. If $I > I_c$ the phase particle starts to slide down the washboard and hence a voltage appears ($\dot{\varphi} \neq 0 \rightarrow V \neq 0$). This way, the RSCJ-model can produce the IV -characteristic of a JJ when C , R and I_c are known. By considering the RCSJ-model as a parallel RLC -circuit we obtain the plasma frequency $\omega_p = 1/\sqrt{L_J(\varphi=0)C} = \sqrt{2eI_c/(\hbar C)}$ and find its quality factor

$$Q_p = \omega_p RC = R\sqrt{2eI_c C/\hbar}. \quad (1.31)$$

The quality factor corresponds to the number of phase oscillations the phase particle undergoes before the amplitude decays by a factor¹ $1/e$ after it's released into a washboard potential wall at zero-bias [4]. The inverse quality factor can be considered as the 'damping parameter' and describes the perceived 'friction' of the phase particle. Counter-intuitively the friction increases as the resistance decreases.

Overdamped Junction

For $Q < 1/2$ the system is in the so-called overdamped regime. Once the sourced current exceeds the critical current, the phase particle moves down the potential but 'sticks' to the washboard potential. When further increasing the current, the time averaged voltage over the junction continuously increases, and slowly approaches the linear normal-state regime. When decreasing the current from above its critical value to below, the phase particle always follows the current bias and is immediately trapped in the washboard potential. The IV -characteristic is therefore non-hysteretic as seen in Fig 1.11(a). When thermal noise is neglected the IV -curve follows

$$\langle V \rangle = R\sqrt{I^2 - I_c^2}\theta(|I| - I_c)\text{sgn}(I). \quad (1.32)$$

It is worth mentioning that in a real experiment thermal noise² is always present and Ambegaokar and Halperin showed that in this case, the point where the junction switches to the normal state smooths out and a residual resistance remains even for $I \rightarrow 0$. This zero bias R_0 resistance can be related to the normal-state resistance as [49]

$$R_0 = \left[\mathcal{I}_0 \left(\frac{\hbar I_c}{2ekT} \right) \right]^{-2} R, \quad (1.33)$$

where \mathcal{I}_0 is the 0-order modified Bessel function. To illustrate this effect, if we assume a JJ with a critical current $I_c = 10$ nA and an electronic temperature $T = 100$ mK, one expects $R_0 \approx 0.11R$.

¹Here e is the Euler's number.

²This is an unavoidable source of disturbance, but one can optimize for it in an experimental scenario.

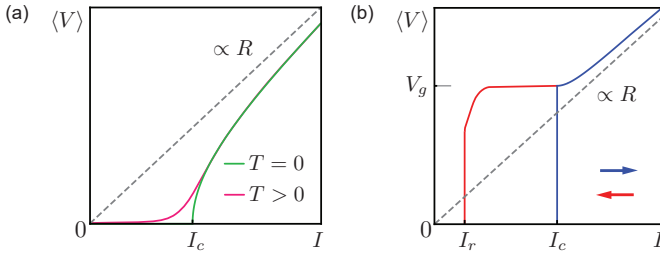
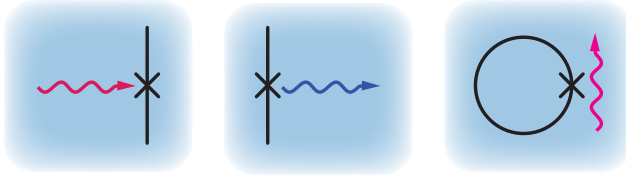


Figure 1.11. IV -curve of a Josephson junction: (a) in the overdamped regime with and without thermal noise, (b) in the underdamped regime with the up-sweep in blue and the down-sweep in red.

Underdamped junction

For $Q > 1/2$ the system is in the so-called underdamped regime. For an ideal tunnel junction where the current bias is increased to above the critical current, the voltage will jump discontinuously up to the energy gap voltage $V_g = 2\Delta/e$. When further increasing the current, the linear normal-state regime will be approached. Because the moment of inertia is large compared to the damping, the phase particle will not be immediately retrapped after reducing the current bias below I_c and one has to go below the so-called retrapping current $I_r \approx 4I_c/(\pi Q)$ to return to the superconducting state, resulting in hysteretic the IV -curve as shown in Fig.1.11(b). Unavoidable thermal fluctuations will cause premature switching from the zero- to the finite-voltage state, making the identification of I_c non-trivial.

2 Probing the Josephson effect



Let us consider a small piece of superconductor connected to four normal metal leads. When measuring this device in a four-probe configuration below T_c and I_c - both properties of the superconductor - we will measure a zero-resistance state. Once the current is increased above I_c , superconductivity will be quenched and one observes a finite-resistance state. The corresponding IV -curve of this rather trivial device will be similar to the one of a Josephson junction. This begs the question: how we can actually distinguish these two cases from each other? Although the answer is simple - one needs to measure the Josephson effect - the experimental realization is not trivial. In this thesis we have made use of three different high-frequency techniques to probe the Josephson effect in superconducting weak links, which will be briefly explained in this chapter.

2.1. Shapiro steps

A very straightforward proof for the Josephson effect is provided by measuring Shapiro steps. Shapiro steps emerge in the IV -curve of a JJ under influence of an ac signal [50, 51]. One can describe this effect from two different points of view: an analytical approach using the Josephson relations or by analyzing the circuit defined by the RCSJ-model. We first consider the analytical derivation, in which we consider a time-dependent voltage-bias across the JJ of the form

$$V(t) = V_{\text{dc}} + V_{\text{ac}} \cos(\omega_{\text{ac}} t), \quad (2.1)$$

where V_{dc} is the dc bias voltage, V_{ac} is the amplitude of the drive and ω_{ac} is the angular frequency of the irradiation signal. By integrating the ac Josephson relation using the voltage argument given in Eq. 2.1, the dynamics of the

superconducting phase difference are obtained

$$\varphi(t) = \frac{2e}{\hbar} \left\{ V_{\text{dc}} t + \frac{V_{\text{ac}}}{\omega_{\text{ac}}} \sin(\omega_{\text{ac}} t) \right\} + \varphi_0. \quad (2.2)$$

Inserting Eq. 2.2 into the dc Josephson relation yields

$$I_s(t) = I_c \sin \left[\frac{2e}{\hbar} \left\{ V_{\text{dc}} t + \frac{V_{\text{ac}}}{\omega_{\text{ac}}} \sin(\omega_{\text{ac}} t) \right\} + \varphi_0 \right]. \quad (2.3)$$

The ‘sine of a sine’ term can be expressed as

$$\sin \{ a + b \sin(x) \} = \sum_{k=-\infty}^{+\infty} (-1)^k \mathcal{J}_k(b) \sin(a - kx), \quad (2.4)$$

where $\mathcal{J}_k(b)$ is the k^{th} -order Bessel function of the first kind with argument b . With this, we obtain the expression for the time varying supercurrent [3]:

$$I_s(t) = I_c \sum_{k=-\infty}^{+\infty} (-1)^k \mathcal{J}_k \left(\frac{2eV_{\text{ac}}}{\hbar\omega_{\text{ac}}} \right) \sin \left(\left\{ \frac{2e}{\hbar} V_{\text{dc}} - k\omega_{\text{ac}} \right\} t + \varphi_0 \right). \quad (2.5)$$

From Eq. 2.5 it can be seen that the supercurrent becomes time-independent, whenever $\frac{2e}{\hbar} V_{\text{dc}} = k\omega_{\text{ac}}$ holds. This means that for $V_{\text{dc}} = k \frac{\hbar}{2e} f_{\text{ac}}$, where f_{ac} is the drive frequency, an averaged dc Josephson current appears, i.e. a Shapiro step [52]. Because the spacing between the Shapiro steps is only dependent on the frequency of the ac drive and fundamental constants, Shapiro steps are used in metrology to define the voltage standard [20, 53].

The same conclusion can be obtained in an illustrative way by making use of the RCSJ-model introduced in Sec. 1.2.6 and apply a combination of ac and dc current bias of the form $I = I_{\text{dc}} + I_{\text{ac}} \sin(\omega_{\text{ac}} t)$. The dc current bias I_{dc} generates a constant tilt of the washboard potential, while the ac current component I_{ac} induces oscillations around the mean slope. The phase particle stays confined in the potential as long as the maximal tilt is smaller than the critical current ($I_{\text{dc}} + I_{\text{ac}} < I_c$), which implies a zero voltage state. When $I_{\text{dc}} + I_{\text{ac}} > I_c$, the phase particle will slide down the potential. However, the ac bias provides a subsequent upwards motion of the potential that recaptures the phase particle. This scenario is depicted in Fig. 2.1(a). We can express the phase velocity as

$$\dot{\varphi} = \frac{\delta\varphi}{T} = \delta\varphi \cdot f_{\text{ac}}, \quad (2.6)$$

where $\delta\varphi$ describes the phase displacement. We expect a clear retrapping of the phase, when $\delta\varphi$ is synchronized with the 2π -periodic washboard landscape. Hence, the phase evolves periodically for $\delta\varphi = k \cdot 2\pi$, where k is the number of potential wells that are overcome in one cycle of oscillation. Consequently, the

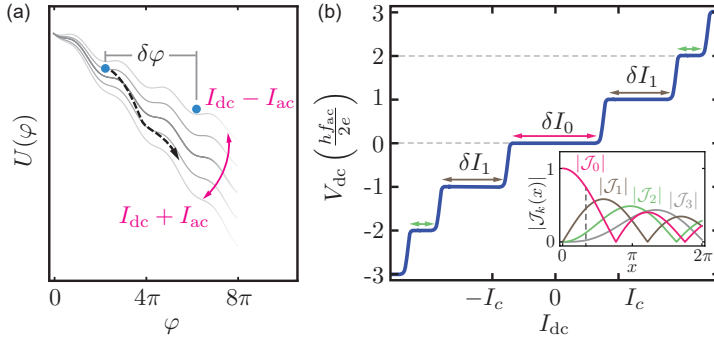


Figure 2.1. Schematic representation for the emergence of Shapiro steps. (a) The rf-drive generates an oscillating tilt of the washboard potential $I_{\text{dc}} \pm I_{\text{ac}}$. The phase particle evolves during the downwards motion of the potential and gets retrapped by the upwards motion. The illustration depicts a phase advancement of $\delta\varphi = k \cdot 2\pi$ with $k = 2$ that is responsible for the emergence of the second Shapiro step. (b) The IV -curve of an underdamped junction irradiated with frequency f_{ac} . Due to the synchronization, Shapiro steps appear at distinct voltage $V_{\text{dc}} = k \frac{\hbar}{2e} f_{\text{ac}}$. The width of the steps δI_k depends on the order as well as on the drive power and are described by Bessel functions. The inset depicts the four lowest-order Bessel functions, in which the dashed line refers to a specific drive amplitude. For this condition we find $\delta I_k > \delta I_{k+1}$.

phase velocity is clearly defined which results, via the ac Josephson relation, in a dc voltage across the junction:

$$\dot{\varphi} = \frac{2e}{\hbar} V_{\text{dc}} = k \cdot 2\pi f_{\text{ac}}. \quad (2.7)$$

Because the synchronization of the particle movement and oscillatory tilt of the potential is possible for a range of dc current values, a voltage step at $V_{\text{dc}} = k \frac{\hbar}{2e} f_{\text{ac}}$ appears in the IV -curve as illustrated in Fig. 2.1(b). The width of the voltage step is given by [24]

$$\delta I_k = 2I_c \left| \mathcal{J}_k \left(\frac{2eV_{\text{ac}}}{\hbar f_{\text{ac}}} \right) \right|. \quad (2.8)$$

Since the Bessel functions exhibit their first maximum for increasing order at larger argument, the Shapiro steps emerge hierarchically with the step $k = 1$ appearing before step $k = 2$ and so forth. For high rf-drive voltages V_{ac} , the Bessel functions become periodic and the amplitude slowly decays.

2.2. Josephson radiation

A more challenging technique to measure the Josephson effect is to detect Josephson radiation. From the ac Josephson relation (Eq. 1.10) we recall that a constant voltage bias across a Josephson junction yields an oscillating current signal, which allows the interpretation of JJs as radiation emitters. The radiative signal directly relates to the CPR, which in general can be represented by a Fourier series [54]

$$I_s(\varphi) = \sum_k (-1)^{k-1} A_k \sin(k\varphi), \quad (2.9)$$

with k being the harmonic orders and A_k the corresponding amplitude. The distribution of the amplitudes defines the shape of the CPR. For example, a CPR changing from a sinusoidal to a forward sawtooth shape modifies the amplitude ratios as $A_{k+1}/A_k = 0 \rightarrow k/(k+1)$. By inserting the ac Josephson relation in Eq. 2.9 we obtain the time-dependent supercurrent

$$I_s(t) = \sum_{k=1} (-1)^{k-1} A_k \sin\left(k \frac{2eV}{\hbar} t\right). \quad (2.10)$$

Hence the power spectral density (PSD), which is a measure for the frequency-dependent radiation intensity, spikes at frequencies $f_{\text{det}} = k \frac{2e|V|}{\hbar}$ [55–58] with the peak height given by the amplitude A_k . In the case of a sinusoidal CPR ($A_k = 0$ for $k > 1$), the PSD for a given detection frequency f_{det} only enhances at $V = \pm \frac{\hbar}{2e} f_{\text{det}}$ while in the presence of higher harmonics, the PSD peaks at voltages $V = \pm \frac{\hbar}{2e} f_{\text{det}}, \pm \frac{\hbar}{4e} f_{\text{det}}, \pm \frac{\hbar}{6e} f_{\text{det}}, \dots$ as illustrated in Fig. 2.2(a).

In a microscopic description, the Josephson radiation can be described as inelastic Cooper pair tunnelling from one superconducting lead to the other [59]. The superconducting condensates on each side of the junction have a single-valued energy, and under the influence of a voltage bias, the Cooper pair needs to dispose of this additional energy when transferring to the other side. This is done by emitting a photon to the environment as illustrated in Fig. 2.2(b) where the energy of this photon equals the energy of the Cooper pair located at a voltage difference V and hence reads $\hbar f_J = 2eV$. The higher-order contributions obtained for transparent junctions can be associated to correlations between single Cooper pair tunnelling events. This correlation can be interpreted as an effective charge q^* transferred in the tunnelling process. Consequently, the energy of the emitted photon can be generalized to be $\hbar f_J = q^*V$. Due to the $2e$ granularity of the supercurrent in conventional JJs, the following effective charges are possible: $q^* = 2e, 4e, 6e, \dots$ as depicted in Fig. 2.2(c).

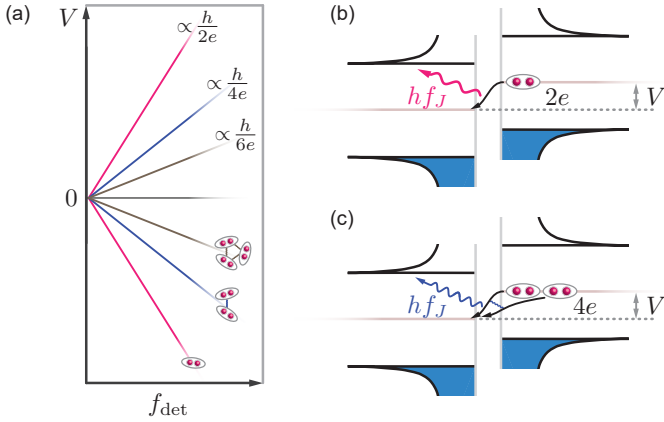


Figure 2.2. Josephson radiation. (a) Illustration of the expected positions of the spikes in the power spectral density (PSD) occurring when the Josephson radiation matches the detection frequency $f_{\text{det}} = f_J = 2eV/h, 4eV/h, 6eV/h, \dots$. The peak height depends on the CPR skewness, higher order processes are in general weaker and have a reduced slope compared to the $2e$ -emission. (b) Inelastic single Cooper pair tunnelling event. The addition energy of the Cooper pair $E = 2eV$ is emitted to the environment with a photon of energy $hf_J = 2eV$. (c) Higher-order inelastic Cooper pair tunnelling event. Two Cooper pairs with total addition energy $E = 4eV$ tunnel coherently and emit a photon of energy $hf_J = 4eV$ to the environment.

2.3. rf SQUID

Until now we have considered the Josephson effect based on the concept of the phase difference between two superconductors, but without considering the tunability of this parameter. If a single Josephson junction is embedded in superconducting loop, a so-called radio-frequency Superconducting QUantum Interference Device (rf SQUID) is formed. In contrast to a dc SQUID in which two JJs are incorporated, an rf SQUID can only be probed with alternating currents.

2.3.1. Phase-biasing

For rf and dc SQUIDS, the phase difference φ across the junctions can be tuned by applying magnetic flux through the loop. Here flux quantization is the key, which dictates that the total magnetic flux through a bare superconducting loop is quantized in integer units of the flux quantum to fulfill continuous

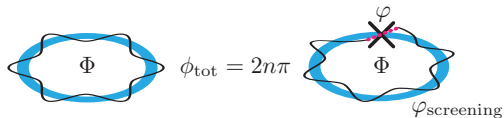


Figure 2.3. Illustration of a superconducting loop penetrated by a magnetic flux Φ . For a bare superconducting ring, the flux inside the loop is quantized to integer multiples of the flux quantum. In the case of an rf SQUID, the flux inside the loop adjusts the phase drop φ across the junction, while the supercurrent inside the loop gives rise to an additional phase. In both cases the total phase ϕ_{tot} acquired in the loop needs to be an integer multiple of 2π .

boundary conditions of the complex wavefunction [60, 61]. The total phase pick-up in an rf SQUID reads

$$\phi_{\text{tot}} = \varphi + \frac{2\pi}{\Phi_0} L_{\text{loop}} I_s(\varphi) - \frac{2\pi}{\Phi_0} \Phi \stackrel{!}{=} 2n\pi, \quad (2.11)$$

where the first term is the phase across the JJ, the middle term refers to the screening field produced by the phase-dependent supercurrent $I_s(\varphi)$ flowing inside the loop with inductance L_{loop} , and the last term evaluates the gauge-invariant phase difference determined by the magnetic flux Φ trying to penetrate the ring. It is important to note that the loop inductance consists of a geometric contribution L_{geo} and a material contribution L_K arising from the kinetic inductance of the superconductor, and hence leads to $L_{\text{loop}} = L_{\text{geo}} + L_K$ [62]. The magnetic flux can be expressed as $\Phi = B \cdot A$, where A is the inner area of the loop and B the external magnetic field perpendicular to the plane of the SQUID. The sum of phases needs to be a multiple of 2π to fulfill the periodic boundary conditions in the superconducting wavefunction as illustrated in Fig. 2.3. By setting $n = 0$ in Eq. 2.11 and by introducing the external phase $\varphi_{\text{ext}} = \frac{2\pi}{\Phi_0} \Phi$ we obtain [63]

$$\varphi = \varphi_{\text{ext}} - \frac{2\pi}{\Phi_0} L_{\text{loop}} I_s(\varphi), \quad (2.12)$$

which describes the phase across the junction while considering the screening field. Since the screening field is determined by the supercurrent carried across the JJ which, in turn, depends on φ , (i.e., the CPR), Eq. 2.12 is an expression without closed-form solution – a so-called transcendental equation.

2.3.2. Screening effect

The non-linearity between the external phase φ_{ext} and the internal phase φ is known as the screening effect. We observe from Eq. 2.12 that the non-linearity

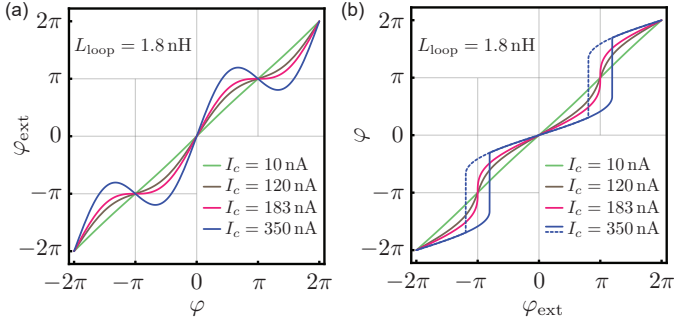


Figure 2.4. Illustration of the screening effect. (a) The external phase as a function of internal phase. For low critical currents the relation is nearly linear, but becomes more and more non-linear for increasing I_c . For the chosen loop inductance $L_{\text{loop}} = 1.8 \text{ nH}$, the crossover to the hysteretic regime appears for $I_c = 183 \text{ nA}$ (pink). (b) The internal phase (across the junction) as function of external phase. The relation is found by inverting the curve shown in (a). In the hysteretic regime, the phase conditions $\varphi = \pm\pi, \pm 3\pi, \dots$ are not accessible and the value of the phase can take on two values depending on the sweep direction: when sweeping from φ_{ext} from left to right one stays on the blue branch while one traverses the dashed branch upon reversing the direction.

becomes more and more pronounced for larger supercurrents and larger loop inductances. The transcendental screening equation Eq. 2.11 can be solved either graphically or numerically. In Ch. B.2 we present a routine to numerically solve the screening formula. Here we briefly discuss the graphical solution by considering a sinusoidal CPR of the form $I_s(\varphi) = I_c \sin(\varphi)$. We can express and plot the external phase as a function of internal phase $\varphi_{\text{ext}}(\varphi)$, which is a sine-function imposed on a linear dependence as shown in Fig. 2.5(a). By inverting the function around the mean slope one obtains $\varphi(\varphi_{\text{ext}})$, which is the desired quantity to extract the internal phase from experimental parameters. This treatment is depicted in Fig. 2.5(b). The inverted function becomes hysteretic when $\partial\varphi_{\text{ext}}/\partial\varphi < 0$. By evaluating this derivative with the CPR given above, reorder the result and minimizing the cosine-term, we obtain the threshold condition for entering the hysteretic regime

$$L_{\text{loop}} I_c > \frac{\Phi_0}{2\pi}. \quad (2.13)$$

Once the hysteretic regime is entered the phase φ can no longer be adjusted arbitrarily. Especially, the phase biasing conditions $\varphi = \pm\pi, \pm 3\pi, \pm 5\pi, \dots$ become inaccessible.

2.3.3. Inductive coupling to a resonator

Since in an rf SQUID configuration, the JJ is in parallel with a superconducting lead, there is no way to measure the device with dc techniques. Therefore, one generally couples the rf SQUID inductively to a resonant tank circuit [64]. As we have seen in Sec. 1.2.5, the inductance of a JJ can be tuned with the phase and phase-biasing the rf SQUID therefore results in a shift of the resonance frequency of the coupled tank circuit. Moreover, the frequency broadening of the resonance provides information on the dissipative mechanisms in the rf SQUID.

Although reading out rf SQUIDS is more involved compared to dc SQUIDS, it has the following advantages: i) only one Josephson junction needs to be controlled, ii) the device can be galvanically isolated, iii) the system can be probed fast and iv) is sensitive to fluctuations in the supercurrent.

Combining the sensitivity of high quality superconducting resonators with rf SQUIDS forms the basis for flux qubits [65–67] and Andreev qubits [34, 36, 68, 69]. The previously mentioned hysteretic phase response of the rf SQUID is the working principle of the flux qubit where the two internal phase values – attributed to a supercurrent either working with or against the external field – form the computational subspace. The working principle of an Andreev qubit on the other hand, is based on the discreteness of the ABS energies. If we consider a JJ with only one single transverse mode and neglect poisoning events, which would introduce parity switches, the system is a pure 2-level quantum object. The two states have distinct inductance values and hence can be probed via the shift of the resonance frequency.

2.4. Detecting Majorana bound states

The measurement techniques presented above are applicable for detecting the features of so-called Majorana modes, which are predicted to appear in topological Josephson junctions [70, 71]. These electronic states obey non-abelian exchange statistics that could be used to realize a perturbation-protected braiding-based quantum information processor [72], and therefore gained tremendous attention in the field of mesoscopic physics. Similar to the Andreev bound states (ABS), the Majorana bound states (MBS) energies depend on the phase across the junction and on its transparency [73]

$$E_{\text{topo}}^{\pm} = \pm\sqrt{\tau}\Delta \cos(\varphi/2). \quad (2.14)$$

The distinctive property for MBS, in contrast to ABS, is that the two states of opposite energy have a different parity, allowing them to cross each other at $\varphi = \pi$. In turn, this leads to a 4π -periodicity as seen from Eq. 2.14 where the MBS undergoes a ground state transition at the crossing point. The decay to this new ground state involves the exchange of a quasiparticle from

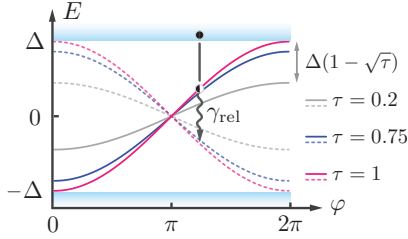


Figure 2.5. Energy dispersion of Majorana modes as a function of phase φ for different transparencies τ . Majorana bound states undergo a ground state transition at $\varphi = \pi$. The relaxation requires the exchange of quasiparticle due to the opposite parity of the states, as indicated by solid and dashed lines respectively.

the continuum to induce a parity switch. The relaxation time of this process γ_{rel} is determined by the dynamical coupling to the quasiparticle environment, and therefore defines the lifetime of Majorana excitations [74]. Since the relaxation processes seemingly restore the 2π -periodicity, the detection of the 4π -periodicity in topological Josephson junctions requires out-of-equilibrium rf measurements at frequencies faster than the equilibration time [75]. Note that the 4π -periodicity adds an additional term to the generalized CPR Fourier series

$$I_{\text{topo}}(\varphi) = A_{\text{topo}} \sin(\varphi/2) + \sum_k (-1)^{k-1} A_k \sin(k\varphi), \quad (2.15)$$

where A_{topo} refers to the supercurrent contribution emerging from MBS. In the remainder of this section we will briefly sketch the features expected for MBS in the previously explained measurement schemes.

Shapiro steps

Returning to the ac biased RCSJ picture as explained in Sec. 2.1, an added 4π -periodic contribution would introduce an even-odd effect in the washboard potential, where subsequent potential wells have slightly different heights. It is theoretically predicted (and is intuitive) that this leads to different trapping properties for the phase particle, which manifests itself as an even-odd dependence of the Shapiro step current-plateau sizes [76, 77]. The observation of this topological feature in the Shapiro step pattern has been claimed for different material platforms: Nb-InSb-Nb nanowire junctions exposed to in-plane magnetic fields [78], Nb-Cd₃As₂-Nb nanowire junctions [79], V-Bi₂Se₃-V 3D-topological insulator junctions [80] and Nb-HgTe-Nb 2D/3D-topological insulator junctions [81, 82].

In general, Shapiro step measurements involve the frequency mixing of the Josephson radiation and the external drive signal, which leads to a complex frequency-dependent electromagnetic environment that might depend on the device architecture far beyond the junction itself. Furthermore, the evolving phase can introduce Landau-Zener transition, suffer from quantum tunnelling events, and thermal excitations. The requirement for observing the 4π -contribution is that the phase adjustment-time needs to be shorter than the lifetime of the MBS, which demands high quality devices [83, 84]. In addition, the fact that the resistance in the RCSJ-model depends on the phase, the frequency and the voltage bias, makes it particularly tedious to deduce topological features from Shapiro step measurements.

Radiation

Another possibility to probe the presence of Majorana states is provided by directly measuring the radiation signal of the junction. Due to the 4π -periodicity it is predicted that the junction emits photons at half the frequency of the trivial $2e$ -signal and is referred to the fractional ac Josephson effect [85, 86]. In this case, the junction radiates at a frequency $f_J = eV/h$, in addition to the conventional $2e, 4e, 6e \dots$ contributions. This implies a $1e$ -granularity of the supercurrent across the junction: a feature which can be interpreted as sequential single electron tunnelling events. In a microscopic picture this process can be understood as the Majorana state storing one electron on one side of the junction, until another electron is transferred. This pair of electrons then recombines into a Cooper pair that will be absorbed in the condensate. Now, the Majorana state is empty and capable of hosting a next single electron, and the cycle repeats. The width of the radiation peak Γ is inversely proportional to the lifetime of the MBS ($\Gamma \propto \gamma_{\text{rel}}^{-1}$).

The signature of $1e$ -radiation has been claimed to be detected on a resistively shunted HgTe junction using off-chip measurement techniques [57] and on an InAs nanowire junction formed by locally removing the epitaxial Al shell. In the later experiment, the radiation was measured by using an elegant on-chip detection technique, incorporating a second Josephson element. The fractional Josephson effect appeared after applying parallel magnetic fields on the order of the expected phase transition point [87].

Although the detection of the fractional ac Josephson effect using radiation is more direct compared to analysing Shapiro step patterns, the observed features have still to be interpreted carefully. For example, the photonic interaction with environmental cavity modes can lead to up- and down-conversion of the radiation signal, which might interfere with the pure radiation signal. Furthermore, the IV -characteristics and the radiation amplitude of JJs depends on the surrounding impedance [59], which is in general frequency dependent and might be modified by magnetic fields [58].

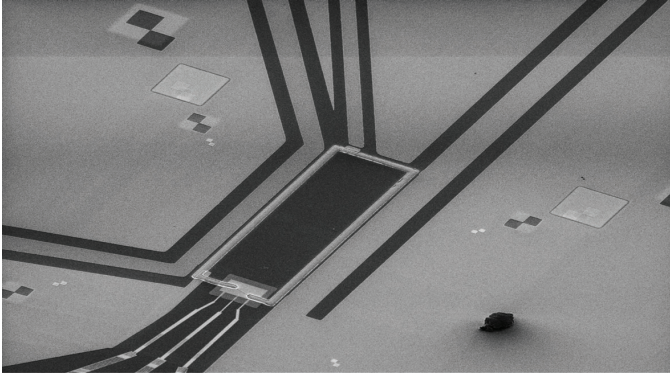
rf SQUID

The most diverse platform to probe Majorana states is likely provided by coupling an rf SQUID consisting of a single mode topological Josephson junction to a resonant tank circuit. This architecture allows to monitor the full complex impedance of the circuit in real time and provides access to the random telegraph signal of the Josephson current [88]. The resulting noise signal at the phase condition $\varphi = \pi$ should have a distinct character for topological junctions when compared to trivial ones for two reasons. First of all, the MBSs in topological junctions can only be populated in two configurations where both carry a current of opposite direction. In a trivial, single mode junction, the ABSs can be occupied in four different configurations, where none of them carry a current ($\varphi = \pi$). Second, in topological Josephson junctions, direct microwave induced transition are prohibited by parity, whereas in trivial junctions some transitions are accessible with electromagnetic field. Consequently, the internal dynamics between the two flavors should be distinct, which in turn, results in a different in supercurrent fluctuation [89–91]. However, we would like to stress that rf SQUIDS always suffer from small phase variations, either coming directly from the coupling to the tank circuit, or from having external sources that give rise to flux noise. Hence, for a highly transparent ABS spectrum there will be similarly large current fluctuations as there would be provided by MBS, due to the close overlap of the spectra apart from $\varphi = \pi$. The dissipation¹ of an rf SQUID consisting of a multichannel Bi nanowire embedded in a W-ring has been measured by the coupling to a superconducting resonator [92]. Although no shifts of the resonance frequency were observed, the shape of the loss peak and its temperature evolution have been claimed to be the signature of a topological Andreev level crossing. We are only aware of this particular experiment declaring non-trivial phase-dependent supercurrent fluctuations.

It is worth to mention that the observed feature is highly disputed in terms of evidence for MBS. One major concern is the possible appearance of many channels with occasionally near-unity transport probabilities, which can mimic the features of MBS. We will show in Ch. 5 that we can quantitatively reproduce the shape and temperature evolution of the dissipation peak with a trivial junction based on a short, diffusive graphene weak link.

¹The fluctuation-dissipation term directly relates the supercurrent fluctuations to the dissipation in the system.

3 Device Fabrication and Design



In this chapter we describe the fabrication processes for realizing the Josephson junctions that are investigated throughout this thesis and discuss the architecture of the resonant tank circuit for probing rf SQUIDs. In Sec. 3.1, we will focus on tunnel junctions formed with the native oxide in-between two overlapping Al regions. In Sec. 3.2 we direct our attention to Josephson junctions based on nanowires. First, we describe the realization of Josephson junctions by Cd_3As_2 nanowires, contacted with superconducting leads. Second, we present the formation of a Josephson junction in InAs nanowires, where its Al half-shell is locally removed to define the weak link. Additionally, the methods used to manufacture the graphene rf SQUID discussed in Ch. 5, are explained together with the fabrication and the design of the coupled superconducting co-planar transmission line $\lambda/4$ -resonator.

The title image presents a nanowire Josephson junction on top of a complex gate architecture embedded in a SQUID loop. The surrounding co-planar structures probes and manipulates the junction. The Josephson effect emerged in the device was weak and will not be discussed.

3.1. SIS tunnel junctions

One way to form a Josephson junction (JJ) is provided by generating a superconductor-insulator-superconductor (SIS) stack, in which the insulating layer is thin enough such that tunnelling between the superconducting leads is possible. An elegant method to realize this type of structure is achieved by making use of the native oxide formed on the lead material. In the following, we describe the fabrication of double angle shadow evaporated Al/AlO₂/Al tunnel junctions, which due to their robustness and reproducibility are widely used in Josephson circuits.

Shadow evaporation

Niemeyer and Dolan [93] developed the idea of an evaporation mask that is suspended above the substrate, which can be used as a shadow mask. In our case the mask consists of a thin suspended resist bridge, which is fabricated with e-beam lithography (EBL) using two different resists on top of each other. The bridge is evaporated under two accurately chosen angles to create an overlap between the subsequent layers, as illustrated in Fig. 3.1(a). With this technique one can fabricate junctions with an overlap down to a few nanometers. If the evaporation angles are $\pm\alpha$, the overlap σ can be estimated by

$$\sigma = 2h \cdot \tan(\alpha) - b, \quad (3.1)$$

where h is the distance between the substrate and the shadow mask, and b is the width of the resist bridge.

Substrate preparation and resist bilayer

We prepare the intrinsic Si/SiO₂ (500 μm /170 nm) substrate by first immersing it in acetone and placing it in a ultrasonic bath for 10 min. This step is repeated with isopropanol (IPA) and followed by a 5 min long UV-ozone¹ plasma. After cleaning the substrate, we spin coat PMMA/MA with a thickness of 600 nm. After baking the first layer, a second resist layer with a thickness of 200 nm PMMA is coated and the bilayer is baked again.

Since PMMA/MA is more sensitive than PMMA to exposure to the electron beam used in the subsequent EBL process, one obtains an undercut after exposure. The undercut geometry is studied with scanning electronic microscope (SEM) imaging in a cross section of a test sample, which is covered with a thin film of Al to avoid charge accumulation. The apparent sharp side profile shown in Fig. 3.1(b) is produced by immediately cleaving the chip after pre-cooling in liquid nitrogen. The shape and magnitude of the undercut depends on the acceleration voltage and generally increases with increasing exposure.

¹UVO-Cleaner[®] Model 42-220

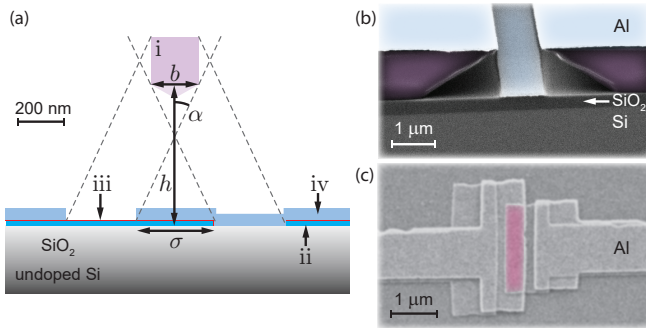


Figure 3.1. (a) Illustration of the double angle shadow evaporation technique with: (i) a 200 nm wide suspended bridge, (ii) a first aluminium (Al) layer (20 nm), (iii) a thin insulating AlO_2 layer, (iv) a second Al layer (50 nm). With a suspension height $h = 600$ nm and evaporation angles $\alpha = \pm 25^\circ$ an overlap $\sigma = 300$ nm is predicted. (b) SEM image of the undercut structures, which enables the fabrication of suspended resist bridges. The resist (violet) consists of a PMMA/MA (top) and PMMA (bottom) stack. (c) SEM image of Al/ AlO_2 /Al Josephson junction. The tunneling region is highlighted in pink.

In order to avoid deposition on the undercut walls, the evaporation angles are adjusted accordingly.

Oxygen cleaning

After the EBL, the sample is developed in a 1 : 3 mixture of methylisobutylketone and IPA (MIBK) for 1 min at 25°C which is followed by 10 s rinsing with IPA and a blow-dry step. On the substrate surface a thin layer of resist residue will remain, which in the vicinity of the junction contaminates the oxide barrier, changing its chemical composition and physical properties [94]. This process leads to a varying junction resistance over time. To minimize the contamination, the sample is cleaned with reactive ion etching using an oxygen plasma.²

Junction design

In the fabrication process, the bridge is the key element for realizing the tunnel junction. We were able to reproduce stable bridges designed with a length of $\sim 3 \mu\text{m}$ and a width of 200 nm. The overlapping area A , which is indicated in Fig. 3.1(c) by the pink shading, can be adjusted with the evaporation angles

²Oxford[®] Plasmalab 80 Plus

and defines the normal state resistance $R_N \propto 1/A$ and hence controls the magnitude of the critical current. Since one side of the bridge is kept wider than the other, the overlapping area is constant, even for slight misalignments during the evaporation. The order of the evaporation angles is chosen such that the wider contact overlaps the smaller one, which prevents the junction edges from further oxidation. This fabrication process and design can be further utilised to create array structures and SQUID loops, in which the critical current can be tuned by an externally applied magnetic field as demonstrated in Ch. 6.

Evaporation

Next, the sample is prepared for the evaporation process and oxidation step. The thin Al layers are deposited in our BesTec system, which is ultrahigh-vacuum evaporator with adjustable sample holder stage. The oxidation of the first Al layer is realized by exposing the structure to an oxygen atmosphere in the load-lock.

For the double angle shadow evaporation, the sample stage orientation is required to be accurately adjustable. In the evaporator, the sample stage can be mechanically tilted described by y and rotated described by x with manipulators on top of the evaporation chamber. In addition, there is a main rotation axis described by z . All adjustments on the orientation can be done, while maintaining the vacuum conditions in the evaporation chamber. The zenith position for the Al target is reached when $y = 99.875$, $x = 0.125$ and $z = 137^\circ$. The device is mounted on the sample holder such that the evaporation angle can be changed by the tilt. A deviation in the tilt from the zenith position of Δy requires an additional correction in the x -axis of $\Delta x = -\Delta y/2$. The evaporation angles are chosen to be $\pm 22.5^\circ \approx \pm 0.25 = \Delta y$, which leads to following tilt coordinates for the two sequential evaporation steps:

$$y = 99.625, x = 0.25 \quad \text{and} \quad y = 0.125, x = 0$$

The Al target is thermally evaporated at 1100°C , while cooling the chamber and the sample stage to increase the film quality. An Al layer of 20 nm is deposited at the first tilt position. After the oxidation process, which is described in the next subsection, a second aluminium layer of 50 nm is evaporated at the other tilt angle.

Oxidation

After the evaporation of the first Al layer, the sample is transferred into the load-lock for the oxidation step. The load-lock chamber connects via a small pipe to a gas bottle filled with oxygen of 5.0 purity and the gas flow can be regulated by a manual inlet valve. We isolate the load-lock by closing the valve,

which is located at the exhaust of the turbo pump. The turbo is switched off and the venting is disabled. After 30 min the number of revolutions goes to zero and the load-lock leaks up to a pressure of $\sim 4 \times 10^{-2}$ mbar. One has to consider, that in this time the sample gets already oxidized a little. Now oxygen is poured in by opening the inlet valve until an oxidation pressure of 1 mbar is reached. The gas flow rate is very hard to control by the inlet valve. Many turns on the valve wheel have to be done until the gas starts to flow into the load-lock. To decrease this flow again, the wheel has to be turned back nearly all the way. The time until the oxidation pressure is reached can vary by a few minutes. After closing the inlet valve, the pressure stays constant during the 10 min of oxidation. The oxidation parameters ($t_{ox} = 10$ min and $P_{ox} = 1$ mbar) are adapted to ensure isotropic, reproducible, self-limited AlO₂ layers with a thickness of ~ 3 nm. The oxidation process is stopped by turning on the turbo again and by opening the exhaust valve. When the load-lock pressure has decreased again to a few 10^{-6} mbar, the sample is transferred back into the evaporation chamber to deposit the second Al layer.

3.2. SNS junctions

In the following sections we describe the fabrication of JJs made of a small segments of semiconducting materials embedded in-between two superconducting leads. In contrast to SIS junctions, the coupling between the superconductors can be tuned in-situ in these devices by changing the charge carrier density inside the normal conducting region with electric fields from a nearby gate. We will first detail the fabrication incorporating Cd₃As₂ and InAs Al shell nanowires (NWs). The experimental results of these types of devices are provided in Ch. 6. JJs formed by NWs are especially interesting, since due their low dimensional side profile they can host single transfer modes desirable to suppress cross-mode scattering. At the end of this section we will provide a brief description for the realization of the multi-mode graphene-Al JJ presented in Ch. 5.

3.2.1. Cd₃As₂ junctions

The Cd₃As₂ nanowires investigated here were grown at the DGIST Research Institute in Hyeongpung, Korea by the vapor transport method [95] and were provided by Minkyung Jung. We pre-pattern base structures by standard EBL techniques [96–98] in combination with the deposition of Ti/Au (5 nm/45 nm) to define bonding terminals surrounding a marker grid on top of a p-doped Si/SiO₂ (500 μ m/305 nm) substrate. The nanowires are transferred by the cleanroom wipe technique explained in the following [99]. A sharp wipe tip is first carefully tapped onto the growth chip using an inverse tweezer. Then the loaded nanowires are tapped off by eye-measures in the center of each base

structure. Using an optical microscope, we selectively locate the nanowires that appear most thin, which have typically diameters of ~ 70 nm. The nanowires are contacted in a quasi-four-terminal configuration in the Balzers evaporation system. After an in-situ Ar-milling step performed during 27 s for removing the native oxide of the wire, Ti/Al (3 nm/200 nm) leads are deposited by e-beam evaporation. We separately optimized the design and the EBL parameters to achieve a source drain spacing of ~ 100 nm. The lift-off in acetone is performed at 60°C and limited to 25 min to prevent damaging of the wire as recommended by Minkyung Jung. After flushing the device with a syringe to remove remaining metal flakes, the device is rinsed with IPA and blow dried with N_2 .

Top gates

We developed a recipe to fabricate highly effective top gates. In contrast to standard fabrication routines, in which the gate dielectrics are grown over the whole sample area by atomic layer deposition (ALD), we designed a local deposition method for ALD films. We make use of the extensive undercut provided in PMMA/MA resist structures. Deep in the undercut, where the ALD layer is weakest it has a predetermined breaking point, which can be triggered during the lift-off procedure. For dc device architectures, the advantage of this method is not directly apparent, however the impact of our development becomes evident by thinking of a resonant structure surrounding the device. The standard procedure would cover the entire surface of the resonator, which would create charge defects in its proximity and hence lowers its quality. With our achievements we can protect the sensitive resonator, and simultaneously make use of the advantages provided by top gates.

We cover the Cd_3As_2 nanowires with a 20 nm thick layer of HfO_2 ,³ which is a dielectric material with high relative permittivity ($\epsilon_r \approx 24$) to optimise the capacitive coupling of the gates to the nanowires. A subsequent top gate electrode deposited across the isolated source drain contacts finalizes the device. These structures typically sustain top gate voltages up to 10 V.

3.2.2. InAs junctions

During our research we had the opportunity to work with the famous InAs nanowires that are covered with an epitaxially grown Al shell in an in-situ process [100]. These nanowires are grown at the Niels Bohr Institute by Prof. P. Krogstrup using molecular-beam epitaxy and provided by Prof. J. Nygård. In contrast to the standard fabrication of nanowire JJs, in which the superconducting electrodes are provided by a separate material deposition step as described in Sec. 3.2.1, here the weak links are defined by locally removing

³Deposited with a Savannah 100 from Cambridge NanoTech Inc. at 220°C .

the Al shell. It has been demonstrated that the atomically sharp boundaries between the inner InAs core and the outer Al shell governs a highly transparent interface with transmission probability near unity [54, 101]. Two flavors of Al shelled InAs nanowires are processed: a ‘full shell’ NW with a ~ 30 nm thick Al mantle covering all facets of the InAs core, which has a diameter of ~ 70 nm, and a ‘half shell’ NW with a ~ 6 nm thick Al layer covering three facets of the InAs core. In the following we will limit our discussion on the latter type.

Micro-manipulator deposition

In order to reduce damage of the growth chip (as one would do using the paper-tip pickup method), we pick up a single NW with glass needles and position it on the desired location of the final chip using a micro-manipulator. This technique allows for instance to place the NW across a pre-defined bottom gate structure. Here, the gates together with the bond terminals are patterned with standard EBL in combination with the deposition of Ti/Al (5 nm/20 nm) layers on top of a Si/SiO₂ (500 μ m/170 nm) substrate. The gate structure is locally covered with a 20 nm thick HfO₂ isolation layer, which enables direct access to the bonding regions.

MF321 Al etching

With the half- and full-shell nanowires, a JJ can be formed by selectively etching the Al shell surrounding the InAs wire, which is a challenging process, especially for the removal of short segments. Together with C. Jünger we established a wet etching recipe based on the information received from Dr. M.T. Deng from the University of Copenhagen. The proper formation of such etch defined JJs is not trivial at all and is discussed in detail in Ref. [102]. In short, the etch mask is formed by using an adhesion promoter in combination with a low viscosity MMA based resist called EL6 from the company MicroResist. The etch windows are EBL defined lines, terminated by larger area openings to increase the rate of flow at the junction during the etching and stopping processes. The TMAH based optical developer MF321 acts as soft etchant with an etch time of 75 s for the half shell Al and 85 s for the full shell Al. The process is stopped by heavily shaking the sample held by tweezers in two subsequent DI water baths for a total flushing time of 50 s. The recipe can be applied to nanowires dispersed on SiO₂ surfaces, as well as for nanowires located across HfO₂ covered bottom gate structures. We would like to point out that the etch results are very sensitive to the ageing of the etchant, and the usage of MF321 shall be omitted after it exceeded its expiring date.

Sputter-deposited NbTiN contacts

The final goal for the InAs half shell junctions is to embed them in a rf SQUID and measure the response of the coupled tank circuit, while exposing the junction to large in-plane magnetic fields of the order of ~ 500 mT, at which a transition to the topological phase is expected. The SQUID loop and the contacts need to sustain those fields, which limits our choice of material to superconductors of type II, or very thin type I, whereas the latter requires elaborated contacting methods. We developed a reliable contact recipe that starts with an Ar-plasma followed by in-situ sputtering NbTiN (130 nm) leads.⁴ Since it is desirable to fabricate the loop and the contacts in one deposition step, we employed the bilayer resist presented in Sec. 3.1 to create an undercut structure that minimizes lift-off problems for the inner loop area. Because the Ar-plasma is rather directional in our system but the sputtered deposited material creeps underneath the contact regions, the contact to the Al shell - if facing towards the target - should always hit the sweet spot where the native Al oxide is removed but where the Al shell itself is still intact.

3.2.3. Graphene junctions

The graphene Josephson junction, which will be investigated in Ch. 5, were fabricated by David Indolese in a collaboration with Dr. Romain Danneau and Dr. Rainer Kraft from the Institute of Nanotechnology at the Karlsruhe Institute of Technology (KIT). The graphene Josephson junction (JJ) is made of a van der Waals heterostructure, which consists, from bottom to top, out of a thick graphite sheet, a bottom hexagonal boron nitride (hBN) with thickness $d = 47.5$ nm, a monolayer graphene and a top hBN (21 nm). We separately prepare the stack by a standard polycarbonate-assisted pick-up technique [103] and place it next to the current anti-node of the resonator that will be discussed in Sec. 3.3. Details about the stacking routine is provided in the supplementary material of Ref. [104]. At the end of this process, the whole device is placed for 1 h in dichlormethane to dissolve polycarbonate residuals to prepare the stacks surface for the following fabrications steps. Interestingly, dichlormethane treatments are used in the fabrication of optical resonators to glaze the surface and to remove excess unbonded fluorescence molecules [105]. This fabrication step might have advantages impacting the surface chemistry of the resonator, resulting in a particularly high internal quality factor as reported in Ch. 5.

⁴AJA[©] ATC Orion 8

Contacting and Shaping

The graphene is contacted and enclosed by a thermally evaporated Ti/Al (5/90 nm) lead, which forms the rf SQUID. Access regions for the self-aligned side contacts [106] are structured with EBL in combination with a CHF_3/O_2 etching step. The contacts to the graphene and the loop are fabricated simultaneously at KIT [107]. The BesTec evaporator at KIT has a specially large ratio between source-diameter and source-sample-distance, which is providing substantial undercut deposition. After contacting, the graphene stack is shaped to a width $W = 1 \mu\text{m}$ using a positive PMMA resist mask in combination with a CHF_3/O_2 etching step. This process step is equivalent to the one described above.

3.3. $\lambda/4$ -resonator

In order to investigate the dynamics of JJs, we follow the approach of coupling an rf SQUID inductively to a tank circuit [25]. In our experiment, the rf SQUID is coupled to the current anti-node of a superconducting $\lambda/4$ -resonator. The resonant structure consists of a meandered co-planar transmission line, which is shorted to ground on one side and interrupted by a coupling capacitance on the other. The capacitive side is coupled via a launcher to the reflectometry set-up. In the following, we will focus on the experimental realization of a NbTiN based $\lambda/4$ -resonator, for which a detailed formal description can be found in Ch. A. The hybrid rf SQUID resonator devices are fabricated by first sputtering a NbTiN film on a bare wafer as described in Sec. 3.3.1. Next, the resonator structure is patterned with a dry etch technique, which will be described in Sec. 3.3.2, and finally the junction element is transferred onto the device and embedded in a superconducting loop as described in Sec. 3.4.

3.3.1. NbTiN sputtering

In the last four years in a group effort, we have developed a sputtering recipe to fabricate ultra-high quality NbTiN films to form magnetic field resilient microwave resonators. Since the film quality is crucial for the sensitivity of the resonators, we deposit NbTiN films on large scale (typically a quarter of a 4 inch wafer) to pre-characterize the film before further fabrications steps. The undoped Si/SiO₂ wafer (500 $\mu\text{m}/170 \text{ nm}$) is thoroughly cleaned with following steps just before the deposition:

- 10 min sonication in deconex[®] 12 basic/DI-water solution (1:100)
→ flush with DI-water
- 10 min sonication in DI-water → blow-dry
- 5 min baking at 120 °C

- 10 min sonication in acetone
- 10 min sonication in IPA → blow-dry
- 5 min UV-ozone in UVO-Cleaner[®] Model 42-220

The wafer is then immediately built into the load-lock chamber of the AJA[®] ATC Orion 8 sputtering machine. We customized our machine by the installation of a substrate shutter, which allows to condition the chamber before sputtering the main film. After inserting the wafer from the load-lock into the sputtering chamber, typical base pressures of $\sim 8 \times 10^{-9}$ Torr are achieved. We form a NbTiN compound by using a NbTi-target (70/30 at%, 99.995% purity) while N₂ is added to the Ar sputtering gas. We position the wafer as close as possible to the NbTi target to minimize particle scattering. The target is off-centred, opening a 20° angle to the zenith axis of the wafer at a distance of 30 cm. Before deposition, the chamber and the NbTi-target are conditioned. During the conditioning steps the substrate shutter protects the wafer from material deposition. We pre-sputter Ti (35 sccm of Ar at 4 mTorr with (DC) 100 W for 20 min) to remove oxygen residuals in the chamber. After terminating the Ti pre-sputtering, we pump on the chamber until pressures $< 1 \times 10^{-9}$ Torr are reached, which typically takes ~ 20 min. Then we sputter NbTi+N₂ (50 sccm of Ar, 3.5 sccm of N₂ at 2 mTorr with 275 W (DC)), while letting the substrate stage rotate. After 4 min of sputtering time, we open the substrate shutter to begin the deposition on the wafer for in total 375 s, which results in a film thickness of ~ 80 nm. The N₂-flow was optimized separately to achieve a stoichiometric compound of NbTiN.

After the deposition, we characterize the film quality in a 4 K liquid He dipstick measurement. For this we typically pattern $\lambda/4$ -resonators of different lengths coupled to a central feedline in a hanger arrangement using optical UV-lithography in combination with a dry etch step discussed in Sec. 3.3.2. From the transmission measurements we can correlate the resonance frequency to the length of the resonators and extract a lower bound for the internal quality factor of the film. Since the kinetic inductance of the film nearly saturates at 4 K,⁵ we can accurately design the resonance frequency of the final structure, which will be measured at ~ 20 mK in a dilution refrigerator.

3.3.2. Design and patterning

Our device structure is designed to aim for a resonance frequency ~ 3 GHz, which is the central frequency of our reflectometry set-up. We plan for a characteristic impedance of $\sim 50 \Omega$ to achieve efficient coupling to the measurements side as well as to the rf SQUID [108]. The meandered co-planar

⁵This is because 4 K is well below the critical temperature of NbTiN (80 nm), which is typical ~ 14 K.

transmission line is designed with a central conductor width of $12 \mu\text{m}$, a clearance of $6 \mu\text{m}$ to the surrounding ground plane and a total length of 7.54 mm . The dimensions of the finger capacitor are aimed for providing a coupling capacitance of $\sim 4 \text{ fF}$. At the shorted end, the spacing between the central conductor and the ground plane is enlarged to create an open area for the SQUID loop. Additional leads, such as a flux line to create an on-chip magnetic field for phase basing the SQUID loop, a supply line for the gate and a pulse line⁶ are guided towards the opening. The supply lines do have on purpose a different aspect ratio to provoke an impedance mismatch for minimizing loss channels for the resonator. From the measurements and calculations presented in Ch. 5 and Ch. A, we deduce for this architecture a resonance frequency $f_0 \approx 3.098 \text{ GHz}$, a characteristic impedance $Z_r = 69.5 \Omega$ and a coupling capacitance $C_c = 4.7 \text{ fF}$.

After cleaning the film with acetone and IPA, we spin coat PMMA and pattern the structure with standard EBL. Using an oxygen plasma, resist residuals in the developed regions are decomposed. The exposed NbTiN regions are dry etched using Ar/Cl₂ gases in an inductively coupled reactive ion etching plasma machine.⁷ The background pressure is set to 1 Pa , the ICP power to 100 W and the rf power to 125 W by supplying an Ar flow of 40 sccm and a Cl₂ flow of 25 sccm . Using these parameters, the NbTiN is etched with a rate of $\sim 3 \text{ nm/s}$, whereas the PMMA mask is etched with $\sim 12 \text{ nm/s}$. To ensure a complete removal of the NbTiN film the etch duration is set to 150% of the actually required exposure time. The etch mask is lifted-off in acetone at 40°C during 1 h in an ultra-sonic bath. The structure is then rinsed with IPA and blow dried with N₂. Contact regions for grounding the loop and markers are patterned subsequently by depositing Ti/Au ($5 \text{ nm}/25 \text{ nm}$) after a 30 s long Ar-milling step in Balzers.

3.4. RF SQUID loop

After transferring the mesoscopic device of interest, either onto a bottom gate structure in the coupling area, or by directly placing it onto the etched SiO₂ surface, the junction needs to be formed and enclosed in a superconducting loop. For our purpose it is desirable to choose a superconducting loop material with a low kinetic inductance. Because this material property adds to the geometric inductance and hence reflects as an increased total loop inductance L_{loop} . As we have seen in Ch. 2.3.2, the screening effect becomes more and more evident with increasing product $L_{\text{loop}}J_c$ and eventually results in a hysteretic behavior, for which the point $\varphi = \pi$ can no longer be reached. Although we developed a method to correct for screening in the non-hysteretic regime

⁶In the measurements present in this thesis we do not make use of the pulse line.

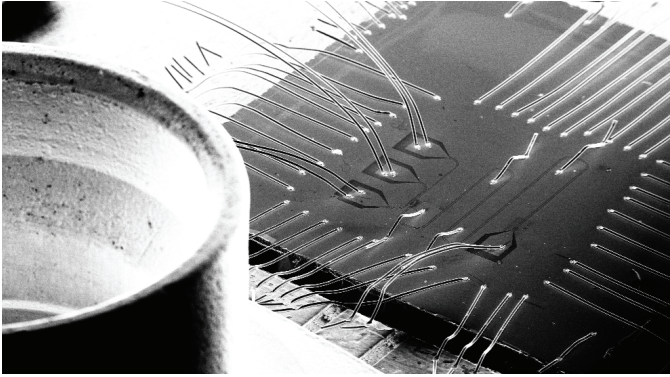
⁷Sentech[©] SI500

it's still advantageous to minimize the $L_{\text{loop}}I_c$ product. This is because close to the hysteretic regime, the oscillating external phase component stemming from the coupling to the resonator, will induce large phase biasing oscillations around $\varphi = \pi$ and hence smears out the region of interest.

The shape of the loop is always a compromise between maximizing the coupling to the resonator, reducing the amount of pick-up noise and minimizing the screening effect. We typically form SQUID loops of rectangular shape with an outer length of $\sim 100 \mu\text{m}$ and outer width of $\sim 40 \mu\text{m}$ and a lead width of $1 - 3 \mu\text{m}$, adapted from Ref. [108]. Hence, the loop surrounds an area of $\sim 4000 \mu\text{m}^2$ implying that $\sim 1 \mu\text{T}$ generates a flux quantum inside the SQUID, or in other words, provides one full phase biasing period. This small magnetic field is governed by the dc current flowing through a strip-line running in parallel along the long side of the loop with a spacing of $\sim 1 \mu\text{m}$. The loop is galvanically grounded to allow gating for hybrid semiconducting JJs. A different coupling method, in which the long axis of the SQUID is galvanically overlapping the central conductor, is expected to maximize the inductive coupling, and shall be considered for future devices.

For the graphene rf SQUID presented in Ch. 5 we chose Al, which has a low kinetic inductance and a relatively small superconducting gap $\Delta_{\text{Al}} = 180 \mu\text{eV}$, which is advantageous for keeping the critical current low. The elongated shape of the loop and the varying lead width (see Fig. 5.1 (b) in Ch. 5) is aimed for building a compromise between maximizing the coupling to the resonator and minimizing screening effects. For this specific geometry we find a self-inductance $L_{\text{loop}} = 211 \text{ pH}$ from finite-element simulations performed in Sonnet [109]. Here, we assume a kinetic sheet inductance of $0.2 \text{ pH}/\square$ for the 90 nm Al film calculated from the value presented in Ref. [110], and extract a mutual coupling inductance of $M = 30.83 \text{ pH}$. These circuit parameters are of particular relevance for the quantification of the electrical properties governed by the Josephson junction itself.

4 Measurement set-up



Josephson junctions are highly sensitive to electronic noise due to their vanishing resistance, and SQUID loops are highly sensitive to flux noise. Both aspects pose an experimental challenge to accurately measure the emission spectra of Josephson junctions or to detect the dispersive and dissipative response of a resonator coupled to a SQUID loop. In the last four years we have improved our two high-frequency equipped dry-dilution refrigerators to enable stable voltage biasing of Josephson junctions on the μV scale and to effectively reduce flux pick-up. In the following chapter we outline the most relevant set-up modifications, provide measurement protocols and report on potential further optimizations.

4.1. Preface

A prerequisite for measuring superconducting circuits is to cool down the specific device below its critical temperature. We have seen in Ch. 1 that the temperature has a substantial influence on the critical current and on the current-phase relation. Since we mainly investigate Josephson elements formed by Al, we measure our devices in dilution refrigerators with a base temperature of ~ 20 mK, which is well below the critical temperature $T_c \approx 1.2$ K of Al. It is worth mentioning that the base temperature is typically smaller than the electronic temperature, which is the relevant parameter for the performance of the devices. To reduce the thermal coupling between the measurement equipment and the device, several thermalization and filter stages are incorporated. However, not only the electronic temperature affects the quality of the measurement, additional external noise sources such as current, voltage and flux fluctuations generally limit the sensitivity of the measurement.

In our group we have two different dilution refrigerators a BlueFors[®] BF-LD400 (BF) and an Oxford[®] Triton 200 system. Both fridges are equipped with microwave components acting in the low GHz regime and with standard dc lines. The BF set-up is extended with an additional mounting stage attached below the mixing chamber plate. In this set-up several samples can be probed simultaneously with rf techniques. In the Triton set-up on the other hand, only one rf device can be measured at a time, but the transfer system installed here enables a roll-over time to a next sample from base temperature to base temperature within ~ 24 h, which is especially convenient for quick characterisation of different samples or modifications on the used PCB. Furthermore, the Triton system hosts a 1-1-6 T vector magnet, where the largest field points along the vertically installed transfer arm. Both set-ups are very similar from an rf and dc wiring point of view, and the here presented measurement schemes and optimization steps should be considered as equally relevant for both systems.

In the following, we will first discuss the set-up for measuring Josephson radiation, with which the results presented in Ch. 6 are obtained. Then we move forward to the reflectometry set-up used for probing a $\lambda/4$ -resonator coupled to an rf SQUID loop, with which the graphene Josephson junction discussed in Ch. 5 is investigated.

4.2. Josephson radiation and Shapiro step set-up

Before diving into the details of the measurement set-up, we would like to point out that measuring the emission spectrum of a Josephson junction is a delicate experiment. First, a stable voltage bias needs to be provided and second, the detection line needs to be sensitive to extremely small signals. Inspired by the

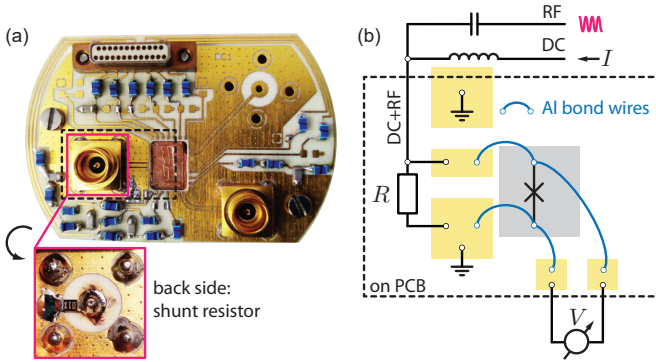


Figure 4.1. PCB for radiation measurements in Triton. (a) Optical image of the PCB with a length of 4 cm and width of 2.5 cm. (b) Schematic representation for bonding a Josephson junction device.

method presented in Ref. [57], we developed an off-chip broadband measurement scheme for detecting Josephson emission in a bandwidth 2.5 – 7.7 GHz, where the exact interval is determined by the circulators in the set-up.

We start our description on the device and PCB level. The PCB shown in Fig. 4.1(a) is patterned with co-planer transmission lines connecting to SMP launchers¹ and consists of dc lines with solder spots for 0603 SMD components connecting to a nano-D adapter. The double-sided Ni/Au plated Roger[®] 4350 PCB is mounted onto a copper plate. The opening for the device is isolated with a small glass plate to allow potential back gating. An essential element of the device – the $10\ \Omega$ metal film resistor that allows for stable voltage biasing and damps the junction – is soldered on the back side in-between the ground plane and the central conductor of the SMP connector.

On the sample side we have made a lot of progress in reducing spurious resonances by designing the feed leads to be short and continuously reducing in width towards the junction, as for instance seen in Fig. 6.10(a). We have seen no qualitative differences between using superconducting or using normal low-ohmic leads. Two bond terminals that act as source drain for the junction, should be fabricated in such a way that they can be placed as close as possible to the central rf line and the ground plane after cleaving. The sample is glued onto the glass plate with PMMA. All connections that are described in the following are made with several Al wire bonds² and are illustrated in Fig. 4.1(b). The central line connects to one side of the junction, whereas the

¹Only one SMP is needed for measuring Josephson radiation and performing Shapiro step measurements.

²Typically three per connection.

other side is connected to ground resulting in a resistively shunted junction.³ Both wire bonds are made as short as possible. Two additional bond wires connect to the differential voltage terminal.

After inserting the PCB, the device is connected to the full measurement set-up presented in Fig. 4.2. The rf measurement line connects via the bond wires to the transmission line and to ground. The dc supply lines are filtered at room temperature, on the PCB and thermalized to the mixing chamber plate via silver-epoxy filters that provide a cut-off of ~ 6 MHz [111]. The current bias is generated by a $1\text{ M}\Omega$ resistor in series with a voltage source and flows via a bias-tee that couples to the rf line through the device to ground. The voltage drop across the junction is measured differentially with a voltage amplifier in a lock-in technique operating at typically 177 Hz with an excitation current between $2 - 10\text{ nA}$. Additionally, the voltage at the output of the amplifier can be measured in dc with a voltage probe, however we report on improved readings with the lock-in technique. In the superconducting regime, most of the current flows through the junction and once the junction switches to the normal state, most of the current will flow through the shunt resistor where the exact division of current depends on the ratio between the normal state resistance and the shunt resistance. By assuming a large junction resistance, the $1\text{ M}\Omega$ source and the $10\text{ }\Omega$ shunt resistor act as a voltage divider and provide a stable voltage drop across the junction.⁴

As we have seen in Ch. 1 and Ch. 2, a constant voltage drop across a Josephson junction leads to an oscillating current. The amplification chain collects this tiny radiation signal and feeds it to a spectrum analyzer. The ac signal is coupled via the bias-tee to a cryogenic HEMT amplifier ($+40\text{ dB}$) located on the 4 K stage that is isolated from the device with two terminated circulators. The signal is further amplified with a room temperature amplifier ($+35\text{ dB}$), which is thermalized to the top plate of the cryostat to minimize temperature-induced gain drifts. The following measurement parameters are typically set at the spectrum analyzer to sense the amplified Josephson emission: detection bandwidth 20 MHz , span 24 MHz , radio bandwidth 10 MHz , video bandwidth 5 Hz and 1001 points resulting in a sweep time of 2 s . The internal attenuation is set to 7 dB and additional pre-amplification is omitted, the detection frequency is sweep between $f_{\text{det}} = 2.5 - 7.7\text{ GHz}$. In addition to the sensing line, a drive line contacts to the device via a directional coupler used for irradiating the junction with a signal generator in Shapiro step measurements.

³Note that the shunt resistor in this configuration additionally acts as ESD protection for the Josephson element.

⁴No further enhancement in the voltage stability was observed when placing the $1\text{ M}\Omega$ source resistor directly on the PCB.

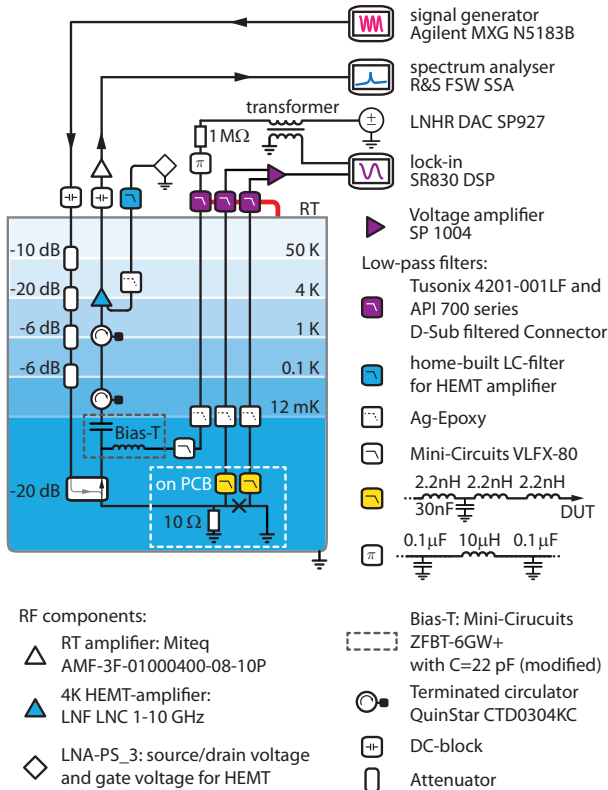


Figure 4.2. Detailed overview of the radiation measurement set-up for the Triton. The Fisher cable connecting the break-out box to the cryostat looms and the cable connecting the 4K HEMT with its power supply are surrounded with several ferrites. The break-out box shield is linked to the cryostat ground with a massive copper mesh-cable which is kept as short as possible (indicated with the red line).

4.2.1. Optimizations

To generate Josephson radiation within the bandwidth of our set-ups, a stable voltage bias $< 15 \mu\text{V}$ is required. Additional voltage fluctuations will smear out the emission peak and hence lower the detectability. Furthermore, externally coupled fluctuations increase the effective electronic temperature, resulting in a reduction of the critical Josephson current. During my PhD we drastically improved our systems in terms of noise level and resolved major electrical issues, which prohibited the detection of Josephson radiation before. In the following, we will briefly sketch our main findings based on the observations at the Triton set-up.

Grounding and shielding

The first step to ensure a proper measurement environment is determined by the grounding of the system. After sorting out several ground loops in the Triton, the cryostat is now only grounded by one cooper loom connecting to a common earth ground, at which all measurement equipment is attached. The frame is floating with respect to the cryostat and is separately grounded at the pump unit. Because connecting the temperature sensors to the resistance bridge generates a ground loop, we omit this connection whenever possible. Because the feedthrough flange for the dc looms was anodized, there was no shield connection between the break-out box and the cryostat. We solved this issue by dismounting the flange, unscrewing the connector, and removing the isolating layer in the contact regions by sanding down the surface.

At the BF set-up we identified a ground loop stemming from the heaters in the He-thermalization-rods, which can be detached after reaching the base temperature.

After sorting out these preliminary issues, we trace the non-vanishing zero bias resistance of an overdamped junction⁵ to further improve the measurement set-up. We denote that covering the ~ 1.5 m long Fisher cable that connects the break-out box to the cryostat with snap ferrites, substantially decreased the resistance value. Following Michael Steinacher's suggestion, we connected the outer cryostat to the break-out box with a massive copper mesh-cable which is made as short as possible. The observed improvement was attributed to a reduced noise-coupling between the Fischer cable shield and the inner measurement looms. Additionally, connecting the measurement equipment to the control computer with a GPIB cable negatively affected the resistance reading, and is overcome with the installation of an optical decoupler.

⁵The resistance value is an indirect measure for the electronic temperature as explained in Ch. 1.2.6.

Magnet power supply and leads

One rather subtle noise source stems from the magnet power supply cables. We observed that when the six magnet leads are attached at the cryostat and floating on the other side, the resistance readout is dependent on the location of the these leads. For instance, the value increases when the leads are close to the pump station but reduces again when moved away and therefore suspect that the electromagnetic pick-up originates from the pump motors. As a result, we relocated the power supplies, shortened the leads as much as possible and shielded the bundled leads with a flexible metal tube. Although this led to an improvement of the measured residual resistance of the test device, connecting and switching on the power supplies still triggers a rise of the zero bias resistance value. For radiation measurements with magnetic fields applied, we denote substantial improvement of the noise level by placing snap ferrites around the magnet leads. For radiation measurements without field, we recommend detaching the magnet leads directly from the feedthroughs for particular sensitive devices. To guaranty a certain clamping and unclamping the brace connectors should be modified by incorporating a second screw fitting.

HEMT wiring and filtering

Probably the most severe issue we identified in the dc biasing lines of the HEMT amplifier. Both at room and base temperatures, we were not able to adjust the source drain voltage as well as the gate voltage to the factory specified settings, and hence were not able to operate the HEMT at its optimal working point. Together with Joost Riderboos we carried out an investigation at room temperature and by sourcing the HEMT directly (not via the fridge wiring) we were able to obtain the factory settings and max out its gain to +40 dB. We identified that high-ohmic looms inside the cryostat are responsible for the discrepancy and replaced this loom section with low-ohmic Cu looms. Furthermore, we installed a filter and thermalization stage on the 4 K plate just in front of the HEMT amplifier. We use low-ohmic silver-epoxy filters with a cut-off frequency of 100 kHz, which are generously provided by Christian Scheller. After these modifications, the HEMT can be accurately tuned to the nominal values at room temperature as well as at base temperatures.

During the development of the Josephson radiation set-ups, we recognized that it is crucial to filter the supply lines for the HEMT amplifier. From various different filter designs the *CLC* π -filters with a cut-off frequency of ~ 150 kHz have shown the best performance. The final filter stage was manufactured Michael Steinacher based on the schematic shown in Fig. 4.3.

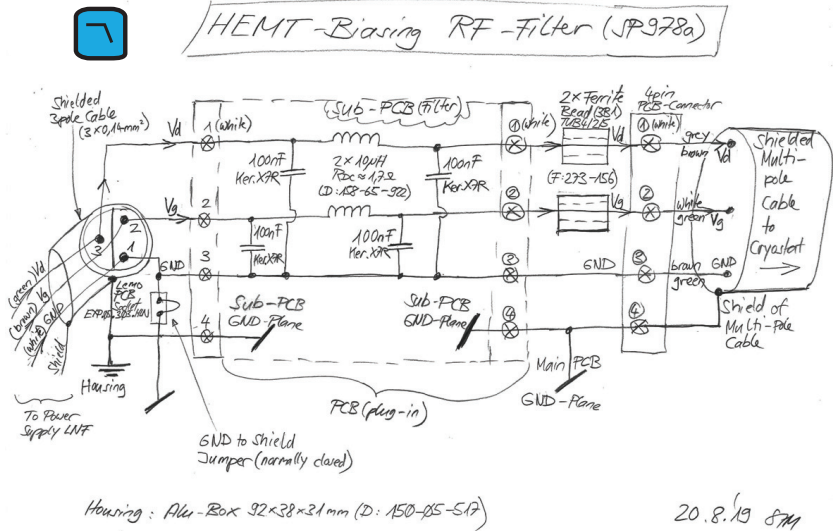


Figure 4.3. Detailed schematic of the home-built LC-filter for the HEMT amplifier drawn by Michael Steinacher. The filter is located at room temperature close to the feed-though into the cryostat.

4.2.2. Possible future improvements

Although we have progressed significantly in making our fridges more suitable for radiation measurements, the following additional improvements could be implemented in the near future.

Bandwidth: When measuring radiation, the voltage difference between emission peaks of different orders linearly increases with frequency. The resolvability of these peaks therefore directly scales with the accessible maximum accessible frequency in our measurement set-ups. In this respect, the Triton set-up should be especially considered for an upgrade, since the system possesses the ability to generate a large vector field. This makes the system especially interesting for probing the nature of potential topological Josephson junctions. Until now the bandwidth is confined to 2.5 – 4 GHz determined by the circulators, which could be replaced to reach frequencies up to 10 GHz, corresponding to the limiting operation frequency of the HEMT amplifier.

Soft ground: We suspect that the stability of the voltage drop across the Josephson elements is limited due to fluctuations on the ground potential. In contrast to the hard ground scheme described above, a soft ground should be considered in which a capacitor between ground and the device is closes the

rf circuit. By carefully choosing the capacitance value, efficient decoupling from the ground fluctuations could be obtained. In addition, by using a soft-ground, the observed increased noise level when using magnetic fields - when originating from cross-coupling to ground - should also be effectively reduced. This modification is compatible with the current PCB design and easily implemented. Note that the return current path would need to be re-routed by incorporating a second dc loom, which in the hard ground situation is provided by the cryostat ground.

One could even think of more elaborated device structure, in which two on-chip fabricated capacitors, bonded to the central rf line and the ground, provide the coupling to the read-out scheme. This arrangement could be accompanied with thin meandered NbTiN dc supply lines, thus forming an on-chip bias-tee, which might reduce the microwave leakage to the current biasing and voltage probe lines.

Tunable shunt resistor: In the currently used measurement scheme, the device is always shunted by the $10\ \Omega$ resistor, making the normal state behavior of the junction is barely detectable. By using a tuneable shunt resistor, for instance a high mobility transistor capable to operate at base temperature or a relay switch, one could access this regime. Furthermore, we suspect that with an adjustable resistor an optimised balance between voltage stability and coupling to the rf lines could be achieved.

Voltage calibration: So far we take the current bias for granted to infer from the differential voltage readings, the resistance and the actually voltage drop across the junction.⁶ However, a voltage biased I/V -converter could be used to measure the sourced current at room temperature for a hard ground device. In the case of soft ground arrangement, the current could be measured via the virtual ground of the unbiased I/V -converter. Another approach employs an SMD resistor on the PCB, in series with the source to extract the current from the voltage drop over the resistance, however this technique suffers from the fact that the resistance value needs to be known accurately.

Parametric amplification: Since Josephson parametric amplifiers provide high gain and potentially have quantum-limited noise, the performance of the amplification chain could be boosted significantly [112]. Especially interesting would be the implementation of a travelling wave parametric amplifier, which still provides nearly quantum limited noise levels, while providing an increased bandwidth and an enlarged dynamical range [113].

SQUID array resonator: Coupling a Josephson junction via a resonator to the amplification chain allows for highly efficient photon absorption and hence increases the signal to noise ratio [59]. By making use of a high quality SQUID array resonator, in which the resonance frequency can be adjusted via

⁶We suspect that the voltage discrepancy observed on the WTe₂ sample shown in Ch. ?? originates from an inaccurate voltage evaluation.

the flux tunable Josephson inductance [19], the Josephson emission spectrum can be probed with increased accuracy. The resonator in-between the junction and the detector acts as a bandpass filter. Whenever the resonance of the SQUID loop cavity equals Josephson radiation frequency, a spike in the measured emission intensity is expected. In particular, the visibility of the weak higher-order emission peaks will be enhanced.

4.3. Reflectometry set-up

The measurements on the graphene rf SQUID presented in Ch. 5 are carried out in the BF set-up after the optimizations listed above. A detailed overview of the high frequency and dc set-up in the BF system is provided in Fig. 4.4. The reflectometry set-up is similar to the radiation set-up presented in Sec. 4.2, but the previously mentioned signal generator and spectrum analyzer are exchanged with a vector network analyser (VNA). In addition, the device is surrounded by a permalloy shield to screen external magnetic field fluctuations. We probe the resonant structure with the VNA in a standard reflectometry configuration. The probe signal reaches the sample via an attenuated input line and a directional coupler. The reflected signal travels back to the VNA through the amplification chain consisting of a room temperature amplifier and 4K-HEMT amplifier, which are isolated towards the device by two circulators located at the mixing chamber plate. The supply lines for the gate and bias voltages of the 4K-HEMT amplifier are filtered with the home-built LC -lowpass filters mentioned in Sec. 4.2.1. The dc lines for tuning the gate voltage on the graphene junction and the flux inside the rf SQUID, are heavily filtered at room and base temperature. In addition to the silver-epoxy filters located on the mixing chamber plate, there is a filter stage in the BF set-up consisting of a cascade of LC SMD π -filters at the 100 mK stage. The gate voltage is supplied via a $1\text{ M}\Omega$ resistor⁷ in series with a voltage source, whereas the current for flux biasing the SQUID loop is directly provided by a current source. Ecosorb[®] lowpass-filters fabricated by Jann Ungerear, are placed in the reflection line which provide a cut-off frequency around 13 GHz. The filter consists of a copper box with a cylindrical hole, in which the central conductor of the rf line is thermalized to the copper wall with Ecosorb[®] enriched epoxy.

⁷This resistor is placed to protect the device and would limit the current in the event of a gate leakage.

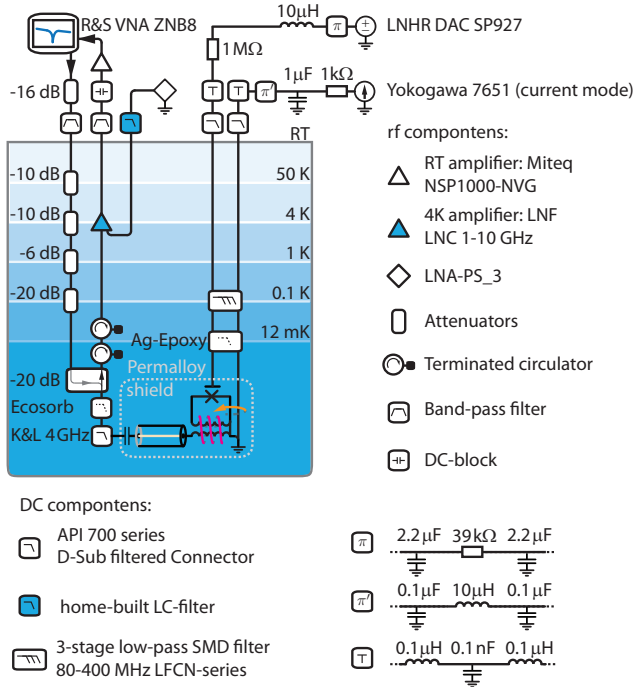


Figure 4.4. Detailed overview of the reflectometry measurement set-up in the BlueFors cryostat.

4.3.1. Bonding

After gluing the sample with silver paste onto the copper backplane of the PCB holder, we connect the rf and DC lines from the PCB with Al bond wires to the ones of the device. We ensure a homogeneous ground plane by adding many grounding bonds around the resonant structure. Additionally, we place bond bridges across the co-planar transmission line and between the areas surrounding the rf SQUID. Fig. 4.5 presents the bond arrangement used for the graphene rf SQUID devices presented later.

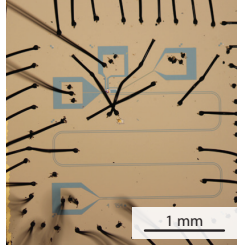


Figure 4.5. Optical picture for illustrating the bonding of the $\lambda/4$ -resonator coupled to an rf SQUID. Note that this picture is taken after removing the sample from the PCB holder after measurement during which some bond wires snapped.

4.3.2. Read-out

The read-out power has a substantial influence on the response of the coupled resonator rf SQUID circuit. In Fig. 4.6 we present the reflectance coefficient Γ as a function of probe frequency f and probe power VNA_{out} . Here, the graphene junction is gated with $V_{\text{bg}} = 4.5 \text{ V}$ (electron doped) and tuned to $\varphi = \pi$ (spectral gap is smallest). We observe that for increasing the probe power the resonance frequency shifts to higher values and the resonance line-shape alters. We attribute this to non-linear effects caused by over driving the resonator or saturating the ABS spectrum. It could also be that the stray field of the resonator induces large phase biasing oscillations, which smears out the phase-dependent features of the JJ. Additionally, irradiating Josephson junctions affects their current-phase relation [114] and the IV -characteristic develops Shapiro steps [50]. Both of these effects will also influence the reflective response. If the read-out power is below -25 dBm , there is no observable changes in the resonance frequency nor in the resonance lineshape for this particular device. All subsequent measurements presented in Ch. 5 are carried out with a probe power $VNA_{\text{out}} = -30 \text{ dBm}$ in a bandwidth $VNA_{\text{BW}} = 500 \text{ Hz}$, which builds a compromise between the collected data quality and read-out time. We would like to stress that such a pre-characterization is crucial for measuring the system in linear response.

Conversion to photon number

By knowing the output power of the VNA, the total attenuation of the input line and characteristic parameters of the resonant structure can be found by fitting the resonance line shape as described in Ch. B.1. Together with the formulas provided in Ch. A, we can evaluate the averaged photon number in

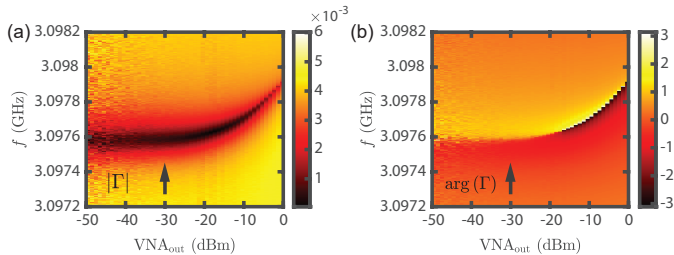


Figure 4.6. Reflection coefficient Γ at $V_{\text{bg}} = 4.5$ V and $\varphi = \pi$ as a function of probe frequency f and probe power VNA_{out} obtained with a bandwidth $VNA_{\text{BW}} = 50$ Hz. (a) Amplitude and in (b) argument of Γ . All subsequent measurements are carried out with $VNA_{\text{out}} = -30$ dBm.

the resonator, which is given by [115]

$$\langle n \rangle = \frac{2}{\hbar\omega_0^2} \frac{Z_0}{Z_r} \frac{Q^2}{Q_c} P_{\text{app}}, \quad (4.1)$$

where \hbar is the reduced Planck constant, Z_0 is the environmental impedance, Z_r is the characteristic impedance of the co-planar transmission line, Q is the total quality factor of the resonant structure, Q_c is the coupling quality factor and P_{app} is the applied microwave power. With $\omega_0 = 2\pi \cdot 3.1$ GHz, $Z_0 = 50 \Omega$, $Z_r = 69.5 \Omega$, $Q = 24000$, $Q_c = 24000$ and $P_{\text{app}} = -130$ dBm ($= 10^{-16}$ W) we obtain an intra cavity photon occupation $\langle n \rangle \approx 90$. This value should be considered a rough estimation since, since P_{app} is determined by using the total attenuation measured at room temperature and does not consider input loss on the PCB and/or the feedline of the device.

Probe flux $\delta\Phi$

Beside the fact that the probe power influences the current-phase relation, it also induces an oscillating phase bias, which we refer to as the probe flux $\delta\Phi$. In order to accurately resolve and sense the phase evolution of the Andreev bound states in the junction under investigation, $\delta\Phi$ needs to be much smaller compared to one full phase period. To estimate the probe flux $\delta\Phi$, we first evaluate the current at the end of the transmission line and then translate the current to the magnetic field strength. From transmission line theory we can derive a function, as shown in Ch. A.4, which expresses the current at the shorted end of a lossless $\lambda/4$ -resonator that is capacitively coupled to a generator (VNA)

$$I_{\text{TL}}(f) = \frac{V_{\text{gen}}}{\sin(\beta l)} \frac{\tan(\beta l)}{jZ_r \tan(\beta l) + Z_0 + (j2\pi f C_c)^{-1}}. \quad (4.2)$$

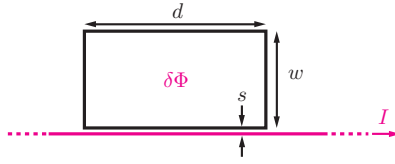


Figure 4.7. Rectangular loop next to a straight current-carrying wire.

Here, $V_{\text{gen}} = 10^{\frac{P_{\text{app}}[\text{dBm}] - 10}{10}}$ [V] is the generator voltage, Z_r is the characteristic impedance of the TL, Z_0 is the input impedance of the generator, $\beta = 2\pi f \frac{\sqrt{\epsilon_{\text{eff}}}}{c}$ is the wavenumber of the transmission line, $\sqrt{\epsilon_{\text{eff}}}$ is the effective refractive index, l is the length of the resonator and C_c is the coupling capacitance. By maximizing the absolute value of this expression for the frequency, one obtains the maximal current in the resonator provided at resonance. With $P_{\text{app}} = -130$ dBm, $\epsilon_{\text{eff}} = 10.24$, $Z_0 = 50 \Omega$, $Z_r = 69.5 \Omega$, $l = 7.54$ mm and $C_c = 4.7$ fF, which are the characteristic parameters deduced from the experiment shown in Ch. 5, we obtain $|I_{\text{TL}}|_{\text{max}} = 310$ nA at 3.094 GHz. The Biot-Savart law expresses the magnetic field magnitude B at distance r apart from a long, thin wire, carrying a steady current in free space

$$B = \frac{\mu_0 I}{2\pi r}, \quad (4.3)$$

where $\mu_0 = 4\pi \cdot 10^{-7}$ N/A⁻² is the vacuum permeability. By substituting values $I = 310$ nA and $r = 1 \mu\text{m}$ one obtains $B = 62$ nT. Furthermore, we are interested in the flux created by this current within a rectangular loop, which can be expressed by

$$\delta\Phi = \frac{\mu_0 I}{2\pi} \cdot d \cdot \ln\left(\frac{s+w}{s}\right), \quad (4.4)$$

where d is the length of the loop, w is the width of the loop and s describes the spacing from the wire to the closer loop edge as shown in Fig. 4.7. With $I = 310$ nA, $d = 80 \mu\text{m}$, $w = 40 \mu\text{m}$ and $s = 1 \mu\text{m}$, which roughly mimics the dimensions of the rf SQUID investigated in Ch. 5, we obtain $\delta\Phi \approx 0.01 \Phi_0$, where $\Phi_0 \approx 2 \times 10^{-15}$ Wb is the magnetic flux quantum, and hence the probe requirement is fulfilled.

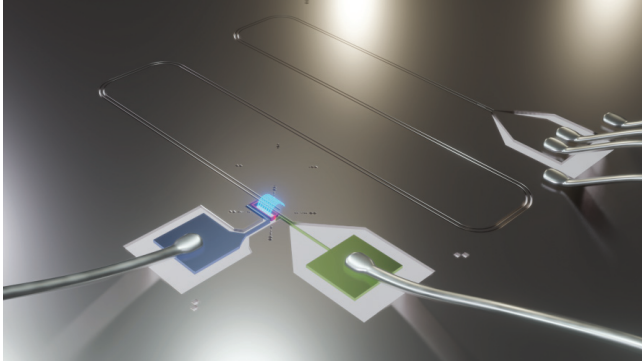
4.3.3. Magnetic field pick-up

During our characterisation of rather large-scale rf SQUID loops sensed by an inductively coupled $\lambda/4$ -resonator, we noted that these devices were highly sensitive to magnetic fields from external sources, as will be illustrated in the following examples.

First, the BF set-up is at a ~ 3 m distance to another cryostat, which hosts a magnet that can provide in- and out-of-plane magnetic fields. In the beginning, the plane of the rf SQUID was facing vertically to the neighboring cryostat. We traced the resonance frequency as a function of time, while sweeping the in-plane magnet in the other cryostat. We observed a direct correlation between resonance frequency shifts and sweep intervals of the magnetic field, i.e., the SQUID loop was flux biased by the neighboring cryostat. After this observation, we re-positioned the cold finger such that the SQUID plane is aligned in parallel to the stray field lines of the other cryostat. However, we would like to mention that this solution is not optimal and the use of magnets in neighbouring cryostates should still be coordinated.

Second, in the Triton set-up the plane of the SQUID was facing perpendicular to the elongation of the transfer arm, which is aligned with the orientation of the cylindrical hole in the vector magnet. The main power supply cable for the whole building runs underneath the nearby corridor at ~ 6 m distance from the sample. Together with David Indolese we investigated the time dependence of the resonance frequency that senses the rf SQUID during 24 h of operation. We denoted an irregular pattern and unpredictable phase jumps during the daytime. However, during the time window from two o'clock in the morning to five o'clock in the morning the resonance frequency was perfectly stable. We cannot say with certainty, but we suspect that the flux jumps are originating from the feedback between the public transport power grid to the in-house network, and its magnetic stray field couples to the SQUID loop. An additional indication is that the time interval where the noise appears, exactly correlates to the hours of operation of BVB – the Basler Verkehrs-Betriebe – the local transport company. After modifying the sample holder such that the SQUID plane runs parallel to the elongation of the transfer arm, these daytime fluctuations were not present. Furthermore, it would be desirable to obtain a permalloy shield for the Triton set-up to protect the sample from external magnetic field fluctuations.

5 Phase-dependent microwave response of a graphene Josephson junction¹



Gate tunability of semiconducting materials provides the basis for classical computers, while analogously, non-linear Josephson elements in microwave circuits are the fundamental building blocks of superconducting quantum computers. The combination of these technologies therefore offers a highly promising platform to in-situ engineer and optimize novel quantum processors. The interplay between the electromagnetic environment and the Andreev bound states (ABS) governing the Josephson effect in superconductor-semiconductor-superconductor junctions is of particular relevance for the performance of these circuits. Here, we inductively couple a graphene-based Josephson junction (JJ) to a superconducting resonator operating at 3 GHz, which enables to probe the structure and dynamics in the ABSs under weak microwave irradiation. By combining a concise circuit model with a rigorous analysis of the reflectometry signal that senses the resonant behavior of the coupled system, we determine the gate-tuneable current-phase relation (CPR) and the phase-dependent loss of the graphene JJ. Thus, we fully characterize the electrical microwave properties of the junction. The experimentally deduced inductive and dissipative microwave response is theoretically reproduced by a short, diffusive JJ model, from which we infer an ABS lifetime of ~ 17 ps implying fast equilibration.

¹This Chapter together with sections from the appendix, the fabrication and the set-up chapters will be submitted to PRX in similar form.

The title image was generate by Gergő Fülöp with blender.

5.1. Introduction

Josephson junctions (JJs) are one of the most amazing devices in mesoscopic physics: they couple superconducting properties through non-superconducting regions. For JJs, in which the superconducting electrodes are linked with a short normal-conducting region, the coherent superconducting interaction is promoted by so-called Andreev bound states (ABSs) [29]. These quasiparticle states are formed in the non-superconducting region and arise from counter propagating electron-hole pairs undergoing consecutive Andreev reflections at the superconducting interfaces [26]. The material and geometrical properties of the weak link together with the superconducting phase difference φ across the JJ define the energy of the quasiparticle states, which due to the electron-hole symmetry appear always in pairs of opposite energies [116]. The structure and the occupation dynamics within the ABSs dictate the inductive and dissipative microwave response, i.e. the admittance of the JJ [41, 117], which is the key quantity to engineer impedance-matched Josephson circuits.

The strong demand for highly tunable junctions in microwave applications has raised the attention to JJs consisting of semiconducting materials, for which the interaction between the superconducting electrodes can be controlled by an electric gate-field [118]. Embedding such a JJ in a superconducting loop forms an rf SQUID, which allows to additionally control the phase across the junction [119]. This rf SQUID coupled to a resonator acts as an effective tunable complex impedance in the circuit that shifts and broadens the resonance behavior, from which one can infer the gate [120] and phase-dependent inductive and dissipative response [32, 121–125], and thereby probe the ABS characteristics [25, 35, 68, 101]. In particular, the inductive response is a measure of the time-averaged dispersion of the populated ABS spectrum, which defines the phase-dependent supercurrent $I_s(\varphi)$ across the junction known as the current-phase relation (CPR) [47, 126]. On the other hand, the dissipative response relates to the fluctuations in the ABS population, which lead to temporal changes in the supercurrent [127, 128]. The short-lived ABS excitations can be activated thermally or induced by microwave photons [32].

In our work we make use of a superconducting microwave resonator coupled to a JJ consisting of a weak-link made of graphene, which is a prototype two-dimensional (2D) material with high mobility and excellent gating properties. Graphene JJs have already demonstrated their compatibility in different superconducting circuits, such as bolometers [22, 23], transmon qubits [129, 130] and tunable microwave cavities [131]. In order to optimize the performance of graphene-based superconducting microwave circuits, knowledge about the Josephson admittance is required. Here, we present a classical circuit model to infer the complex admittance of a graphene JJ from the reflective response of the coupled microwave circuit operating at ~ 3 GHz. We further translate this to the CPR and the phase-dependent dissipation at different charge car-

rier densities and describe our observations within the framework of ABSs. The experimental results are in remarkable agreement with the theoretically predicted microwave response of a short, diffusive JJ.

5.2. Device structure

The device investigated here is presented in Fig. 5.1 and consists of a graphene JJ embedded in a superconducting loop, which inductively couples to a coplanar transmission line (CTL) resonator. The resonant structure and supply lines are etched into NbTiN (80 nm) sputtered on an intrinsic Si/SiO_x (500 μm/170 nm) substrate. The meandered CTL shown in Fig. 5.1(a) is shorted to ground on one side, and interrupted by a coupling capacitor on the other. Both of these terminations act as microwave mirrors of the opposite type, and thereby form a superconducting λ/4-resonator with a fundamental bare resonance frequency $f_{\text{bare}} = 3.098$ GHz.

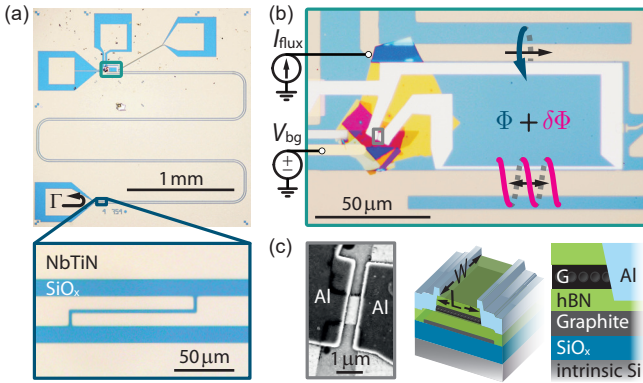


Figure 5.1. Graphene rf SQUID inductively coupled to a superconducting transmission line resonator. (a) Optical image of the NbTiN λ/4-resonator consisting of a meandered co-planar transmission line with the shorted end (current anti-node) on top, seen also at the bottom of image (b), and the open end (current node) at the bottom, shown in the zoom-in. (b) Optical image of the monolayer graphene (G) Josephson junction (JJ) embedded in an Al loop forming the rf SQUID. The DC current I_{flux} creates a flux Φ inside the loop (blue line), which allows to phase bias the JJ. The inductive coupling to the resonator induces a small oscillating probe flux $\delta\Phi$ (red lines). The gate voltage V_{bg} applied on the bottom graphite sheet tunes the charge carrier density in G. (c) SEM image and cross-sectional schematics of the hBN-encapsulated G-JJ with Al side-contacts of width $W = 1 \mu\text{m}$ and length $L = 400 \text{ nm}$.

The graphene JJ, shown in Fig. 5.1(c), is made of a van der Waals heterostructure consisting of a monolayer graphene encapsulated in hexagonal boron nitride (hBN). The lower hBN layer (47.5 nm) separates the graphene flake from the bottom graphite gate. A thermally evaporated Ti/Al (5 nm/90 nm) lead contacts the graphene from both sides [106] and encloses the junction in a loop, thus forming a graphene rf SQUID, which is inductively coupled to the current anti-node of the resonator as illustrated in Fig. 5.1(b). The galvanic grounding of the loop defines the reference potential for the gate voltage V_{bg} applied on the bottom graphite structure. The DC current I_{flux} controls the magnetic flux Φ inside the loop and therefore tunes the external phase difference $\varphi_{\text{ext}} = 2\pi\Phi/\Phi_0$ across the rf SQUID, where $\Phi_0 = h/2e$ is the superconducting flux quantum. Details about the device fabrication can be found in Ch. 3.

In the subsequent experiment we perform reflectance measurements on the port denoted by Γ in Fig. 5.1(a) and investigate the resonant circuit as a function of V_{bg} and I_{flux} , from which we later infer the current-phase relation and the phase-dependent loss of the graphene JJ.

5.3. Reflectometry

The coupled microwave circuit is probed by reflectometry in a dry dilution refrigerator, in which the device is surrounded by a permalloy shield. With a vector network analyzer we measure the complex reflection coefficient Γ as a function of probe frequency f and I_{flux} . We ensure a quasi-equilibrium sensing by setting the probe power to an averaged intra-cavity occupation of ~ 100 photons, which corresponds to an oscillating probe flux $\delta\Phi \approx \Phi_0/100$ inside the SQUID loop. Details about the measurement set-up and the calibration of the probe power can be found in Ch. 4. Additionally, we tune the charge carrier density in the graphene layer by applying a gate voltage in the range $V_{\text{bg}} = [-9, 9]$ V. For the conversion from V_{bg} to charge carrier density consider Ch. D.

The reflective response at $V_{\text{bg}} = 6$ V presented in Fig. 5.2 is exemplary for the whole measurement set. Clear periodic shifts of the resonance frequency f_0 as a function of I_{flux} can be observed in Fig. 5.2(a) and Fig. 5.2(b). We encounter no phase jumps and relate the external phase $\varphi_{\text{ext}} = n_{\text{odd}}\pi$ ($= n_{\text{even}}\pi$) to points of minimal (maximal) resonance frequencies.[122, 125] Besides f_0 , the resonance lineshape also changes as seen in Fig. 5.2(c) and Fig. 5.2(d) when comparing line cuts at $\varphi_{\text{ext}} = -\pi$ and $\varphi_{\text{ext}} = 0$. As we will show, both the modulation in f_0 and the altered lineshape are the consequence of a phase-dependent electrical impedance of the graphene JJ.

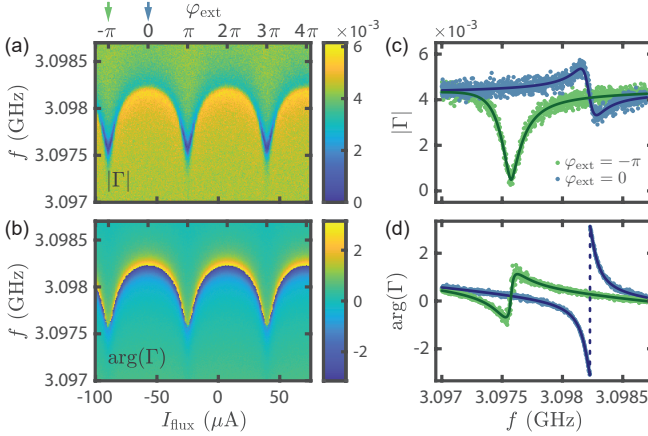


Figure 5.2. Flux dependence of the reflection coefficient Γ at $V_{\text{bg}} = 6$ V. (a)-(b) Colormaps of $|\Gamma|$ and $\arg(\Gamma)$ as a function of probe frequency f and DC flux current I_{flux} . The horizontal top axis represents the conversion to the external phase φ_{ext} across the rf SQUID. (c)-(d) $|\Gamma|$ and $\arg(\Gamma)$ at $\varphi_{\text{ext}} = [-\pi, 0]$ overlaid with fits to Eq. 5.1 (solid lines).

In order to characterize the JJ from the reflective response, we fit $|\Gamma|$ and $\arg(\Gamma)$ simultaneously for each combination of V_{bg} and I_{flux} with the complex resonance curve of a loaded $\lambda/4$ -resonator expressed according to Ref. [132] as:

$$\Gamma = \left[\frac{\Gamma_{\text{min}} + 2jQ \frac{f-f_0}{f_0}}{1 + 2jQ \frac{f-f_0}{f_0}} - 1 \right] e^{j\phi} + 1 \quad (5.1)$$

Thus, we can deduce f_0 and assess the broadening of the resonance curve. The latter is determined by the total quality factor $Q = 1/(Q_{\text{load}}^{-1} + Q_i^{-1} + Q_c^{-1})$, which in turn, consists of three different dissipation sources: i) The inverse load quality factor Q_{load}^{-1} describes loss generated by the rf SQUID, ii) the inverse internal quality factor Q_i^{-1} describes loss inherent to the properties of the CTL and iii) the inverse coupling quality factor Q_c^{-1} describes loss to the measurement environment. Here, Q_{load}^{-1} and Q_i^{-1} are merged to an effective quality factor $Q_e = 1/(Q_{\text{load}}^{-1} + Q_i^{-1})$. Furthermore, we define $\Gamma_{\text{min}} = (Q_c - Q_e)/(Q_c + Q_e)$ and introduce the angle ϕ , which accounts for an asymmetric line shape.

The fits to Eq. 5.1 at $\varphi_{\text{ext}} = -\pi$ and $\varphi_{\text{ext}} = 0$, shown in Fig. 5.2(c) and Fig. 5.2(d) as solid lines, reveal an overall shift of 660 kHz in f_0 and a drastic change in Q_e , while Q_c and ϕ remain similar (see Tab. 5.1). At $\varphi_{\text{ext}} = -\pi$, we

obtain $Q_e = 19\,400$ and $Q_c = 23\,400$; whereas at $\varphi_{\text{ext}} = 0$, we find $Q_e > 200\,000$ and $Q_c = 23\,700$. Consequently, the resonator is undercoupled ($Q_e < Q_c$) at $\varphi_{\text{ext}} = -\pi$, but overcoupled ($Q_e > Q_c$) at $\varphi_{\text{ext}} = 0$, which explains the distinct resonance lineshapes [133]. Since Q_i can be treated as a constant with Q_e being a lower bound, we conclude that $Q_i > 200\,000$. This large value allows us to treat the CTL as lossless ($Q_i^{-1} = 0$) such that $Q_e \approx Q_{\text{load}}$. In Ch. B.1 further insights about the resonance curve fitting is provided.

φ_{ext}	f_0	ϕ	Q_c	Q_e
$-\pi$	3.09755 GHz	0.224	23 400	19 400
0	3.09821 GHz	0.235	23 700	> 200 000

Table 5.1. Fit results for the resonance frequency f_0 , asymmetry angle ϕ , coupling quality factor Q_c and effective quality factor Q_e at different phase conditions at $V_{\text{bg}} = 6$ V.

The observed flux tunable microwave response in terms of f_0 and Q_{load} is the direct manifestation of phase-dependent microscopic processes in the graphene JJ [122], which will be discussed in detail in Sec. 5.7 and Sec. 5.8 within the framework of ABSs. In the following section we model the electrical properties of the graphene JJ with lumped elements and explain their effect on the resonant behavior with the circuit of a loaded $\lambda/4$ -resonator.

5.4. Circuit model

The inductively coupled rf SQUID acts as a variable load impedance Z_{load} attached to the resonator, which tunes the reflective response. We express Z_{load} according to the circuit schematic depicted in Fig. 5.3. The rf SQUID is modeled as a loop with self-inductance L_{loop} in series with the JJ. The mutual inductance M quantifies the coupling strength to the resonator, which is built from a CTL with characteristic impedance Z_r . The JJ itself is represented by a variable Josephson inductance L_J in parallel with a variable shunt resistance R_s . For this arrangement the load impedance terminating the resonator reads [134]:

$$Z_{\text{load}} = \frac{\omega^2 M^2}{j\omega L_{\text{loop}} + (G_s + jB_J)^{-1}}, \quad (5.2)$$

where $\omega = 2\pi f$ is the angular frequency, $G_s = 1/R_s$ is the shunt conductance and $B_J = -1/(\omega L_J)$ is the susceptance. Note that $Y = G_s + jB_J$ is the complex admittance of the JJ.

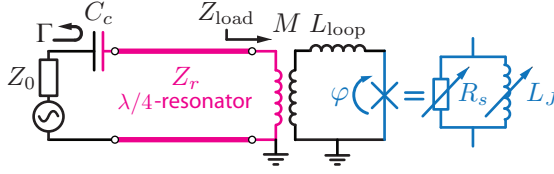


Figure 5.3. Circuit schematic of a rf SQUID coupled to a $\lambda/4$ resonator. The resonator couples inductively to the rf SQUID with strength M and connects to the reflectometry setup via capacitance C_c . The rf SQUID is modeled as a loop with self-inductance L_{loop} in series with the JJ, which in turn, is modeled as a variable Josephson inductance L_J in parallel with a variable shunt resistance R_s . This forms a variable load impedance Z_{load} , which tunes the reflective response Γ .

The influence of Z_{load} on the $\lambda/4$ -resonator is twofold and is derived in Ch. A: First, the imaginary part of Z_{load} causes a shift of the resonance frequency

$$\delta f_0 = f_0 - f_{\text{bare}} = -\frac{2}{\pi Z_r} \text{Im}(Z_{\text{load}}) f_{\text{bare}}, \quad (5.3)$$

with respect to the unloaded resonance frequency f_{bare} . Second, the real part of Z_{load} gives rise to dissipation in the resonant circuit, which is described by

$$Q_{\text{load}} = \frac{\pi Z_r}{4 \text{Re}(Z_{\text{load}})}. \quad (5.4)$$

From Eq. 5.2 one recognizes, that the junction variables, G_s and B_J affect both $\text{Re}(Z_{\text{load}})$ and $\text{Im}(Z_{\text{load}})$. Consequently, δf_0 and Q_{load} would need to be considered simultaneously to evaluate them. However, it turns out that, due to the obtained relatively large Q_{load} values, one is allowed to set $G_s \rightarrow 0$ to infer the inductive part from δf_0 . With this approximation Eq. 5.3 simplifies to

$$\delta f_0 \approx \frac{8}{\pi^2} \frac{M^2}{L_p (L_J + L_{\text{loop}})} f_{\text{bare}}, \quad (5.5)$$

where L_p is the parallel LC -equivalent inductance of the $\lambda/4$ -resonator. This means that the shift of the resonance frequency mainly originates from the Josephson inductance L_J , whereas the broadening of the resonance originates from the dissipation in the JJ specified by the shunt conductance G_s . These two circuit parameters, L_J and G_s are of high interest, since they describe the full complex microwave admittance of the JJ.

Since the inverse Josephson inductance is a measure of the change in the supercurrent $I_s(\varphi)$ with respect to the phase φ across the junction [47]

$$L_J(\varphi)^{-1} = \frac{2\pi}{\Phi_0} \frac{\partial I_s(\varphi)}{\partial \varphi}, \quad (5.6)$$

we can express the resonance frequency shift and the behavior of $L_J(\varphi)$ with the current-phase relation (CPR).

In order to quantify the CPR and G_s from the resonator response, we perform finite-element simulations [109] based on the device geometry, to acquire $L_{\text{loop}} = 211$ pH and $M = 30.83$ pH. Moreover, we find $Z_r = 69.5 \Omega$ from conformal mapping techniques [135] in combination with properties of the resonator, and deduce $L_p = 4.55$ nH. Details about the evaluation of Z_r and L_p can be found in Ch. A.3.

5.5. Current-Phase relation

In this section we extract the CPR by fitting the periodic shift of the resonance frequency under consideration of self-screening effects. The coupling strength between the superconducting leads is determined by the Cooper pair transmission probability and defines the shape of the CPR. For small coupling or low transmission probability the CPR is sinusoidal, whereas the CPR becomes forward-skewed for increased coupling. Due to the semiconducting properties in graphene JJs, the coupling strength and therefore the CPR skewness can be tuned with the gate voltage [104, 131, 136–138]. To capture the non-sinusoidal behavior, we express the CPR as Fourier series [54]

$$I_s(\varphi) = \sum_k (-1)^{k-1} A_k \sin(k\varphi), \quad (5.7)$$

with k being the harmonic order and A_k the corresponding amplitude.

In order to extract the CPR from the measured resonance frequency modulations we need to relate the external phase φ_{ext} to the phase difference φ across the JJ. This is not straightforward, since if a supercurrent flows within the rf SQUID, there is a phase drop over the loop in addition to the phase drop over the JJ, which leads to a non-linear relation between the internal phase φ and the external phase φ_{ext} – known as the screening effect [3]:

$$\varphi = \varphi_{\text{ext}} - \frac{2\pi}{\Phi_0} L_{\text{loop}} I_s(\varphi). \quad (5.8)$$

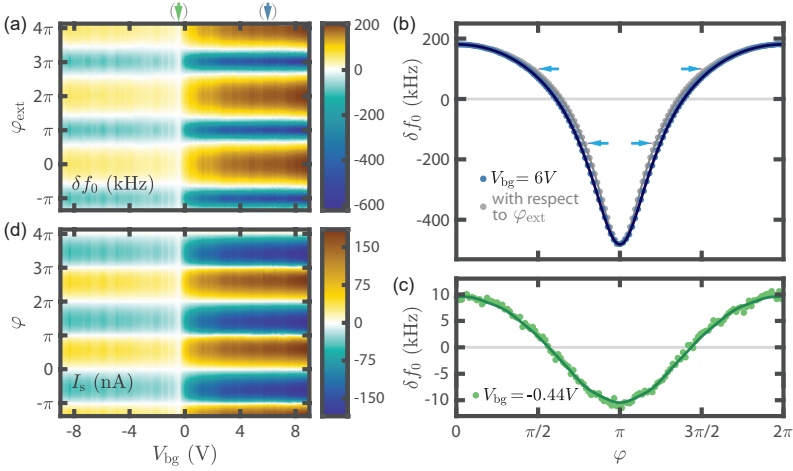


Figure 5.4. Evaluation of the CPR. (a) Colormap of the resonance frequency shift $\delta f_0 = f_0 - f_{bare}$ with $f_{bare} = 3.098$ GHz as a function of gate voltage V_{bg} and external phase φ_{ext} . (b) δf_0 at $V_{bg} = 6$ V as a function of φ and φ_{ext} , respectively overlain with the curve fittings (solid lines), from which the CPR is deduced. Arrows illustrate the screening effect, which is eliminated by an iterative fitting routine, and from which the internal phase φ is obtained. (c) δf_0 at the charge neutrality point ($V_{bg} = -0.44$ V) as a function of φ overlain with the fit (d) CPR inferred from (a) as a function of V_{bg} .

Here, we obtain the CPR for each gate voltage by solving the set of equations Eqs. 5.5-5.8 in a self-consistent way by using an iterative fitting method. The basis for this method is the resonance frequency shift as a function of φ_{ext} , which is presented for the entire gate range in Fig. 5.4(a). At each fitting iteration we include Fourier amplitudes A_k upto to the 10th-harmonic and allow for small changes in f_{bare} to account for parasitic effects. This method is detailed in Ch.B.2.

In Fig. 5.4(b) we illustrate the effect of screening by comparing δf_0 as a function of φ and φ_{ext} , respectively – for the example at $V_{bg} = 6$ V. The corresponding CPRs, deduced from fitting the modulations in δf_0 with respect to phase, shown as solid lines in Fig. 5.4(b), are presented in Fig. 5.5(a). The screening consideration causes a distortion of the phase around π as indicated by arrows. Omitting this effect results in an apparent enhancement of the skewness [139]. Even after correcting for screening, we find a substantially forward-skewed CPR, visualized by the comparison with a sinusoidal behavior. Although screening effects are small in this case, we want to emphasize that

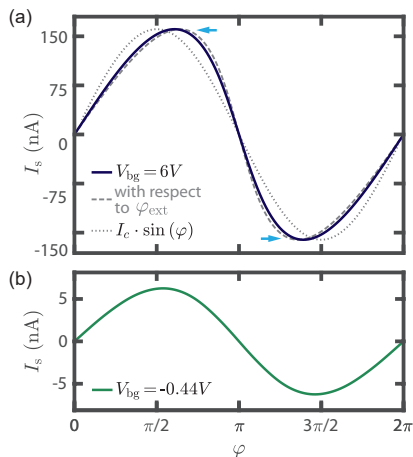


Figure 5.5. (a) Presents the corrected (blue) and uncorrected (dashed) CPR at $V_{bg} = 6V$ deduced from the fit shown in Fig. 5.4 in comparison with a sinusoidal behaviour (dotted). (b) CPR at the charge neutrality point $V_{bg} = -0.44V$.

they can have a significant impact on the evaluated skewness, especially for larger I_s and L_{loop} .

In Fig. 5.4(d) we map the extracted CPR as a function of V_{bg} . The smallest CPR amplitude is found at $V_{bg} = -0.44V$, which we attribute to the charge neutrality point (CNP) of graphene. Here, resonance frequency modulations of only ± 10 kHz can still be clearly resolved as seen in Fig. 5.4(c), which demonstrates the sensitivity of the microwave circuit. The CPR at the CNP, shown in Fig. 5.5(b), is slightly skewed and has a maximal supercurrent of $I_c = 6.3$ nA.

In the following, we quantify the CPR and its skewness by two commonly used ways: i) by the skewness parameter $S = (2\varphi_{max}/\pi) - 1$, where $\varphi_{max} = [0, \pi]$ is the phase maximizing the CPR to the critical current I_c [137], and ii) by directly providing the set of Fourier amplitudes A_k [54]. The latter description is more precise, since it captures the entire CPR lineshape, whereas the S -parameter together with I_c is not uniquely characterizing the CPR, but might be more intuitive.

In Fig. 5.6 we employ both of these characterizations to illustrate the gate dependence of the CPR. We observe a rapid enhancement of I_c up to ~ 200 nA for gating towards positive voltages (n -doped), whereas towards negative voltages (p -doped) the increase is weaker and reaches only ~ 50 nA as seen in Fig. 5.6(a). Because A_1 closely follows I_c , the CPR is mainly determined by

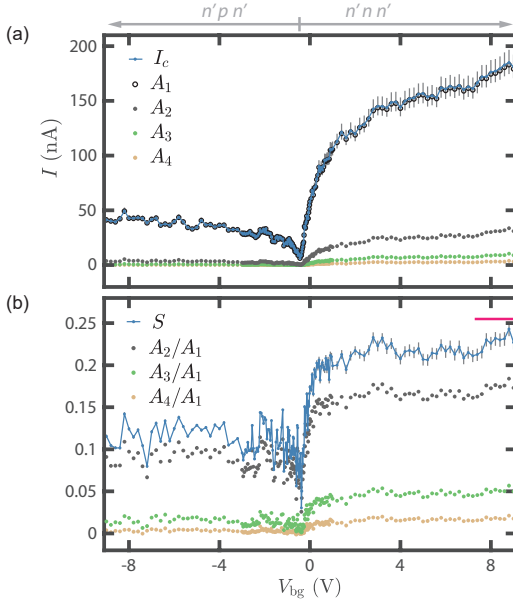


Figure 5.6. Characteristics of the CPR as function of gate voltage V_{bg} . The step size in V_{bg} is reduced close to the CNP ($V_{bg} = -0.44$ V). (a) Critical current I_c and Fourier amplitudes A_k . (b) Skewness parameter S and ratios A_k/A_1 . The theoretical skewness value for a short, diffusive system under ideal conditions $S = 0.255$ is illustrated with the pink mark. (a)-(b) Systematic error bars in I_c and S are generated by modifying M by $\pm 3\%$ and L_{loop} by $\pm 5\%$ in the CPR evaluation.

the 2π -periodic sinusoidal contribution for all V_{bg} . However, the small additions from higher harmonics lead to a forward-skewed CPR. The amplitudes A_k for $k \geq 5$ are negligibly small and omitted in the figures. From Fig. 5.6(b) it appears that the skewness saturates in both doping regimes with a slight reduction around the CNP. For the n -doped side, the skewness saturates around $S \approx 0.22$, whereas on the p -doped side the skewness is less pronounced, saturating around $S \approx 0.12$. The ratios A_k/A_1 follow the same trend.

The asymmetric behavior in I_c and S with respect to V_{bg} are attributed to the presence of n' -doped contact regions inducing additional scattering potentials. The JJ is therefore more transparent in the $n'nn'$ -situation compared to the $n'pn'$ -case [137, 140]. We speculate that the minimal skewness of $S \approx 0.05$ close to the CNP originates from the formation of electron-hole puddles [141] in the graphene flake, which further enhance the scattering probability.

5.6. Phase-dependent loss

Having the CPR extracted, we now deduce the phase-dependent dissipative part of the graphene JJ; namely, the shunt conductance G_s . We can infer G_s from Eq. 5.4, in which we express the susceptance B_J with the CPR according to Eq. 5.6 and make use of Q_{load} obtained from the reflectance curve analysis.

From Fig. 5.7(a), we observe that around the 0-points ($\varphi = n_{\text{even}}\pi$) the dissipation in the microwave circuit stemming from the rf SQUID is minor

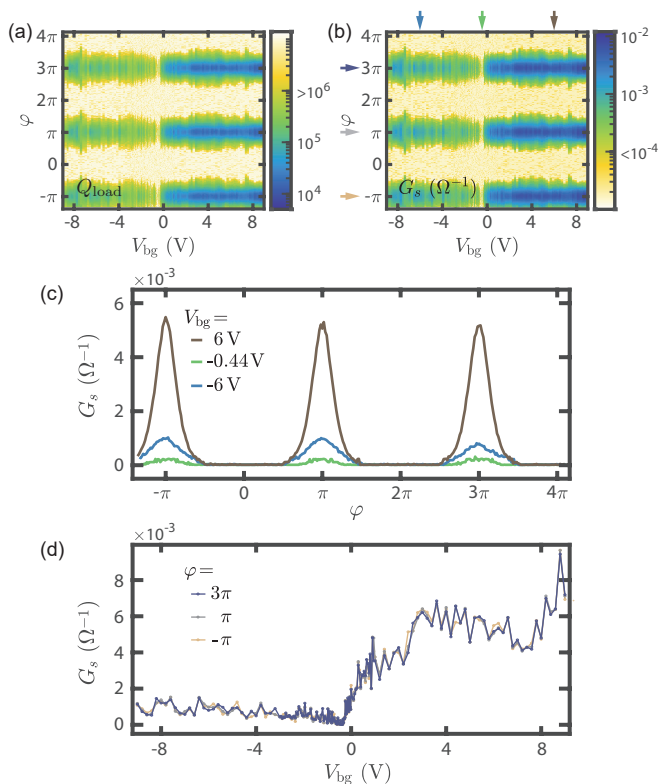


Figure 5.7. Evaluation of the shunt conductance G_s . (a) The load quality factor Q_{load} in logarithmic scale as a function of V_{bg} and φ , deduced from resonance curve fittings. (b) G_s in logarithmic scale obtained by using Eq. 5.4 with Q_{load} and the CPR results. (c) Phase dependence of G_s for different gate voltages. (d) Gate dependence of G_s for phase biasing conditions $\varphi = n_{\text{odd}}\pi$.

($Q_{\text{load}} > 200\,000$) for all V_{bg} . However, at the π -points ($\varphi = n_{\text{odd}}\pi$), the dissipation becomes significantly larger and gate dependent with a minimal quality factor of $Q_{\text{load}} \approx 9800$.

This behavior is reflected in G_s , which is mapped in Fig. 5.7(b) as a function of V_{bg} and φ . Around the 0-points, we deduce low conductance values $G_s \leq 0.1 \text{ m}\Omega^{-1}$, which refers, according to the parallel circuit model presented in Sec. 5.4, to weak dissipation. In contrast, at the π -points, a pronounced Lorentzian-shaped dissipation peak develops, as seen in Fig. 5.7(c). The dissipation onsets locate symmetrically around the π -points and are weakly gate dependent. On the other hand, the peak heights are strongly influenced by V_{bg} and reach a maximal value of $G_s \approx 10 \text{ m}\Omega^{-1}$ at large n -doping. Although the amplitude of the peak appears to fluctuate as a function of V_{bg} , the height replicates for the three π -points, as illustrated in Fig. 5.7(d). This demonstrates the stability of the gate-tunable potential landscape in graphene.

5.7. Theory of Andreev Bound States

In the following we relate the CPR and the phase-dependent dissipation to the concept of Andreev bound states (ABSs) formed within the JJ. Coherent Andreev reflections of quasiparticles at the graphene-superconductor interfaces lead to the formation of ABSs. These quasiparticle states transfer Cooper pairs across the junction in form of counter propagating electron-hole pairs [142]. Due to the electron-hole symmetry, the ABSs come in pairs; one state has negative energy $E_n^- \leq 0$ and the other has positive energy $E_n^+ = -E_n^-$, where n stands for a specific transport channel. The spectral gap δE quantifies the minimal transition energy between states with negative and states with positive energies.

Inherent to wide junctions – like the graphene JJ investigated here – is that there are various possible transport channels leading to many ABSs and hence to a dense ABS spectrum [143]. The phase dependence of the ABS spectrum is determined by the geometry of the JJ and its material properties, i.e. the superconducting gap Δ in the leads and the inverse transport time in the normal region that relates to the Thouless energy E_T . In the ballistic transport limit $E_T = \hbar v_F/L$, where v_F is the Fermi velocity in the normal region and L is the junction length. In the diffusive limit $E_T = \hbar D/L^2$, where $D = v_F l_{\text{mfp}}/2$ is the diffusion coefficient determined by the elastic scattering mean-free path l_{mfp} . An important characteristics of JJs is whether they are in the ‘short’ or ‘long’ junction limit. The former case is realized when $E_T \gg \Delta$, while the latter holds in the opposite limit. The condition for the short junction limit can also be expressed with the coherence length ξ , which needs to be longer than L . In the ballistic case the coherence length reads $\xi = \hbar v_F/\Delta$ and in the diffusive case $\xi = \sqrt{\hbar D/\Delta}$.

As already seen in Ch. 1, for a short multi-channel JJ the ABS energies are given by $E_n^\pm(\varphi) = \pm\Delta\sqrt{1 - \tau_n \sin^2(\varphi/2)}$, where τ_n is the transmission probability of a specific channel. Since diffusive transport associates to continuously distributed transmission coefficients following Dorokhov's bimodal distribution [42], describing that there are many channels with low transmission, but also many with high transmission probabilities, a dense ABS spectrum with a spectral gap $\delta E = 2\Delta|\cos(\varphi/2)|$ emerges for short diffusive JJ as illustrated in Fig. 5.8(a). Characteristic for this type of JJ is that the spectral gap closes ($\delta E \rightarrow 0$) towards the π -points while it is maximally open ($\delta E = 2\Delta$) at the 0-points. Long, diffusive junctions behave similarly, but the spectral gap evolves as $\delta E \approx 3E_T|\cos(\varphi/2)|$ [32].

The structure of the ABS spectrum is relevant because each occupied state carries supercurrent proportional to the derivative of its energy with respect to phase. The sum over the set of all channels defines the total supercurrent [37], which can be expressed as

$$I_s(\varphi) = \frac{2\pi}{\Phi_0} \sum_n f(E_n^\pm) \frac{\partial E_n^\pm}{\partial \varphi}, \quad (5.9)$$

where $f(E_n^\pm)$ is a functional describing the occupation probability of the n^{th} ABS. In equilibrium the functional is given by the Fermi-Dirac distribution.

At zero temperature and in the absence of photons, all ABSs with negative energies are occupied ($f(E_n^-) = 1$), whereas all ABSs with positive energies are empty ($f(E_n^+) = 0$). In this situation the system is in the ground state and the occupation of the ABS spectrum is constant. Therefore the supercurrent I_s is free of any fluctuations. By virtue of the fluctuation-dissipation theorem, [144] there is no dissipation and the effective junction shunt conductance assumes $G_s \rightarrow 0$.

When finite electronic temperatures T and/or the absorption of photons from the electromagnetic environment are considered, the situation becomes different; thermal activation and/or microwave-induced transitions will drive the system out of the ground state. The excitation-relaxation dynamics gives rise to fluctuations in the ABS population ($f(E_n^\pm) \neq \text{const.}$), and correspondingly, in the supercurrent as well. Consequently, there is dissipation and a finite shunt conductance G_s appears [128]. When the spectral gap closes ($\delta E \rightarrow 0$), which is the case at the π -points in transparent ballistic and coherent diffusive junctions, already small temperatures T and small photon energies hf will trigger fluctuations. We note that the fluctuations are determined by the temperature, the photon absorption and emission rates and as well by the relaxation time τ_{rel} of a non-thermal distribution towards a thermal one, which we express in the following as the energy $\gamma = \hbar/(2\tau_{\text{rel}})$. In conclusion, this means that in general, both the inductive and dissipative part of a JJ depend on the ABS spectrum and the population dynamics within this spectrum.

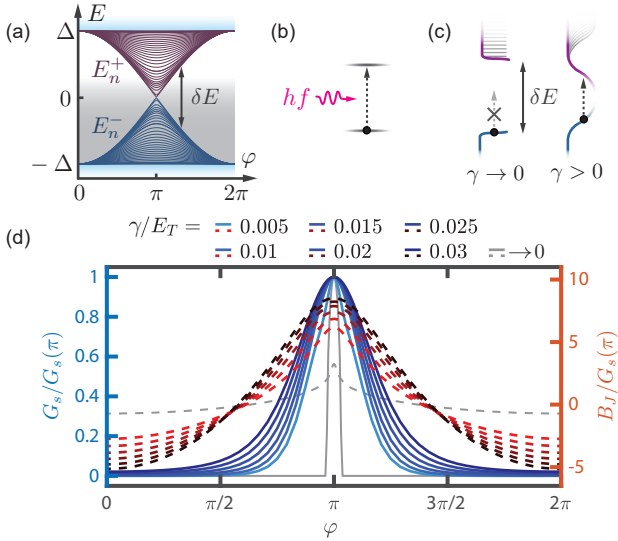


Figure 5.8. ABS spectrum and theoretical microwave response for a short, diffusive JJ. (a) Spectrum of a short JJ with multiple channels of different transparencies. (b) Microwave-induced transitions between states triggered by the absorption of a photon with energy hf . (c) The finite lifetime of states described by the relaxation rate γ causes a spectral broadening of the ABS energies and hence blurs the transition condition. (d) Theoretically predicted G_s (blue, left axis) and B_J (red, right axis) normalized by the conductance value at $\varphi = \pi$ as function φ for different γ/E_T ratios. The normalization values read for increasing γ/E_T , $G_s(\pi)/G_N = 45, 11, 8.6, 7, 5.9, 5, 4.4$, where G_N is the normal state conductance. Here: $\Delta/E_T = 0.1$, $hf/E_T = 0.01$ and $kT/E_T = 0.008$.

In order to explain this in more detail and later compare this to our experiment, we make use of theoretical works [41, 117]² that predict the linear microwave response of JJs in terms of the susceptance B_J and the shunt conductance G_s . For the theoretical analysis we consider a diffusive multi-channel JJ in the short junction limit at finite temperature coupled to a photonic environment of energy hf . Note that in the experiment the photonic environment is provided by the driven microwave resonator.

Once the spectral gap becomes smaller than the excitation energy $\delta E \leq hf$, transitions across the gap are accessible leading to a sharp onset in G_s as

²Pauli Virtanen for the University of Jyväskylä performed numerical simulations to solve the time-dependent Usadel equations.

depicted by the solid gray line in Fig. 5.8(d). The width and the height of the dissipation peak depends on characteristic energy scales denoted in the figure caption. It is worth mentioning that not only transitions across the gap lead to dissipation; all possible absorption processes, including intra-band excitations $E_n^+ \rightarrow E_m^+$, contribute to it, whereas the transition probability scales according to Fermi's Golden rule with the available density of states [120]. Fig. 5.8(b) depicts a microwave-induced transition of a quasiparticle from an arbitrary initial state to an available final state.

The fact that the ABSs have a finite lifetime specified by γ causes a spectral broadening of the energies. This results in a blurring of the transition condition ($\delta E \leq hf$) as sketched in Fig. 5.8(c). Therefore, increasing γ , i.e., shortening the lifetime, broadens the dissipation peak as seen by the blue lines in Fig. 5.8(d). Importantly, the lifetime broadening also affects the susceptance, in particular the phase conditions for $B_J = 0$ shift away from the π -point, which is equivalent to a reduction of the CPR skewness. Note that B_J for $\gamma \rightarrow 0$ shown in dashed gray appears different, because it is rescaled with a large conductance value $G_s(\pi)$. Besides this, also the electronic temperature T influences the dissipative and inductive response, because the temperature balances the population between E_n^+ and E_n^- -states as described by the Fermi-Dirac distribution.

The theoretically predicted response as function of T together with experimental results as well as a representation of Fig. 5.8(d) without normalization are presented in Ch. C.

In short, environmental perturbations, namely, temperature and electromagnetic irradiation, cause dynamical variations in the population of ABS spectra on the timescale of the non-equilibrium occupation lifetime, which influence the susceptance B_J likewise the CPR and give rise to dissipation captured by the shunt conductance G_s .

5.8. Comparison with Theory

Finally, we compare the experimental results of the graphene junction with theoretical predictions based on the assumption of a short, diffusive multi-channel JJ.

The CPR of a short, diffusive junction in equilibrium can be expressed analytically, from which one obtains a skewness $S = 0.255$ at $T = 0$ [41, 43] as indicated in Fig. 5.6. The assumption of predominantly diffusive transport in the graphene JJ investigated here is supported by multiple observations: i) the small discrepancy to the experimentally determined skewness at large n -doping ($S \approx 0.22$), ii) the lack of Fabry-Pérot oscillations [137] in the gate dependence of the CPR presented in Fig. 5.6, and iii) the randomly evolving shunt conductance G_s seen in Fig. 5.7. The reduced skewness in the p -doped

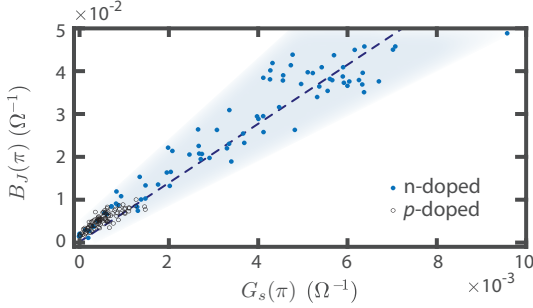


Figure 5.9. Susceptance B_J versus shunt conductance G_s obtained at $\varphi = \pi$ follows a linear trend as predicted for a short, diffusive junction.

regime ($S \approx 0.12$) we assign to an overall suppression of the transmission probability due to the formation of pn' -junctions at the graphene-superconductor interfaces. Since the superconducting coherence length of similar devices is reported to be $\xi \approx 500$ nm [143, 145] and the junction under investigation has a length $L = 400$ nm, the condition for the short junction limit $\xi \geq L$ seems reasonably valid.

One theoretical prediction, which was not explicitly pointed out above, is that the inductive and dissipative response (B_J, G_s) scale linearly with the normal state conductance G_N [41, 117], which is here tunable with the gate voltage. From Fig. 5.9 one can retrace this statement, since the relation between the experimentally deduced values of the susceptance B_J and conductance G_s obtained at $\varphi = \pi$ for all different V_{bg} – clearly follows a linear trend. Furthermore, the ratio B_J/G_s is the inverse loss tangent describing the quality of the Josephson inductance [125]. A larger ratio implies a more ideal behavior of the inductance. Counter-intuitively the ratio at the π -points decreases for lowering the temperature or reducing the relaxation rate, whereby the latter effect can be inferred from Fig. 5.8(d). This behavior might originate from the bimodally weighted ABS spectrum. We attribute the cone-shaped spread around the mean ratio ($\langle B_J(\pi)/G_s(\pi) \rangle \approx 7$) seen in Fig. 5.9 to altered ABS spectra and modified relaxation dynamics at different gate voltages.

In the next step, we search for the best match between the theoretically predicted and the experimentally deduced phase-dependent microwave response by considering both the inductive and the dissipative properties of the JJ. To this end, we numerically generate sets of B_J and G_s with different characteristic parameters. In particular, we vary the ratios kT/E_T and γ/E_T to account for a finite electronic temperature and capture the effect of lifetime broadening. We have fixed the Thouless energy to $E_T = 10\Delta$ and the pho-

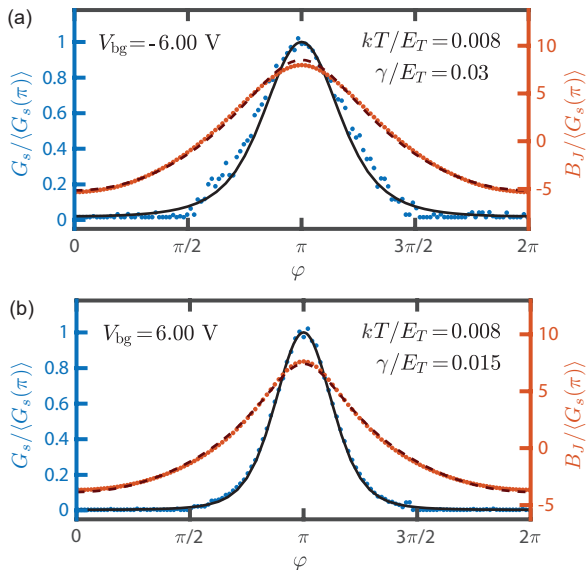


Figure 5.10. Experimental observations in comparison with theoretical predictions for a short, diffusive JJ. (a)-(b) Normalized measured G_s (dotted blue, left axis) and B_J (dotted red, right axis) overlaid with the normalized theoretical predictions for G_s (solid blue) and B_J (dashed red), for which $\Delta/E_T = 0.1$ and $hf/E_T = 0.01$ are fixed, but kT/E_T and γ/E_T are variable. The best fitting parameter ratios are indicated in the figure. For $V_{bg} = -6\text{ V}$ (6 V) the normalizations read $\langle G_s(\pi) \rangle = 0.98\text{ m}\Omega^{-1}$ ($5.23\text{ m}\Omega^{-1}$) for the experimental traces and for the theoretical traces $G_s(\pi) = 4.4 G_N$ ($7 G_N$), where G_N is the normal state conductance.

ton energy to $hf = \Delta/10$: the first condition ensures the short junction limit, whereas the second one compares favourably well to the expected experimental relation between the photon energy of the resonator and the superconducting gap of Al.

In Fig. 5.10(b) we compare the normalized theoretical and experimental values for $V_{bg} = -6\text{ V}$, whereas in Fig. 5.10(c) we perform the comparison for $V_{bg} = 6\text{ V}$. The experimental values G_s (blue dots) and B_J (red dots) are normalized with the shunt conductance at $\varphi = \pi$, denoted by $\langle G_s(\pi) \rangle$ ³. Close overlap between theory and experiment can be found for both gate voltages

³We average the three shunt conductance values closest to $\varphi = \pi$ to accommodate for scattering of the data.

with the same temperature ($kT/E_T = 0.008$), but distinct relaxation rates γ .

At $V_{bg} = -6$ V we observe differences between the model and the experimental data even with the best match ($\gamma/E_T = 0.03$). This is especially evident at the flanks of the dissipation peak and the susceptance at the π -point. We attribute this mismatch to an inappropriate choice of transport regime for this gate voltage, because here the additional pn' -junctions at the interfaces effectively elongate the quasiparticle trajectories and l_{mfp} becomes shorter. As a consequence, the JJ tends to be in the long-junction limit.

On the other hand, we stress that we observe striking agreements between the theoretical predictions with $\gamma/E_T = 0.015$ and the experimental data at $V_{bg} = 6$ V. Apparently, the model of a short, diffusive junction reproduces simultaneously the inductive and dissipative response of the graphene JJ for this doping configuration. By evaluating the best fitting ratios $kT/hf = 0.8$ and $\gamma/hf = 1.5$ with the resonance frequency $f = 3.098$ GHz, we deduce an electronic temperature $T = 120$ mK and obtain an relaxation time $\tau_{rel} = 17$ ps. A similar equilibration time ($\tau_{rel} = 7$ ps) is reported for an equivalent short diffusive Al-graphene JJ probed at mK temperatures and large n -dopings [146]. We would like to mention that the ABS spectrum of a short, diffusive junction might not be the only spectrum which in a similar theoretical model could reproduce the experimentally observed response. In particular, in a wide JJ the ABS spectrum can be built from quasiparticles with long and short trajectories leading to more complex ABS structure than discussed above [143].

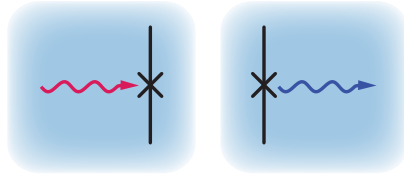
5.9. Conclusion

We have measured the reflective response of a microwave resonator inductively coupled to graphene-based rf SQUID as a function of flux-bias and charge carrier density. We made use of a concise circuit model to infer from the modulations in the resonance frequency and the broadening of the resonances the current-phase relation and the phase-dependent dissipation of the graphene JJ. We hereby obtain the full complex admittance of the junction, which is the key parameter to achieve impedance-matched Josephson microwave circuits.

Our comprehensive investigation demonstrates the impact of the environment on the performance of JJs in terms of finite temperature and microwave photons. If the environment provides energies larger than the spectral gap, short-living excitations appear in the ABS spectrum, which induce fluctuations in the supercurrent and lead to dissipation. The comparison between the experimentally deduced microwave response at high electron density and the one predicted by theory for a short, diffusive junction model yields striking agreement, from which we deduce a relaxation time of 17 ps. This quick thermal relaxation makes graphene-based devices, which additionally stand out due to their low electron-phonon coupling, unique candidates for highly

sensitive and fast bolo- and calorimeters [22, 23, 147]. Furthermore, the device architecture and measurement protocols presented in this work are well-suited to explore the fundamental properties of other JJs, such as junctions made of 2D/3D topological insulators or Dirac and Weyl semimetals [92]. Particularly, the topological nature of these JJs can be probed, because it is predicted that they host ABS states, which cross at the π -points, but do have opposite parities, meaning that microwave-induced transitions across the gap are prohibited [74]. As a consequence, it is expected that the dissipative character of topological JJs is distinctly different from trivial ones [90, 91], which could be probed with the technique presented here.

6 Josephson Radiation and Shapiro Steps¹



Measuring the frequency dependent emission of voltage biased Josephson junctions is a powerful way to probe the charge correlations of the supercurrent and provides direct access to the Fourier components of the current-phase relation. We investigate the Josephson radiation from many different kinds of Josephson junctions which we can classify in three categories: (1) Al-based SIS tunnel junctions, (2) 1-dimensional SNS junctions, one made of an InAs nanowire and one made of Cd₃As₂ nanowire, and (3) higher dimensional junctions made of HgTe and WTe₂. We report on various phenomena that modify the emission spectrum beyond the trivial $2e$ -radiation. In particular, we observe the down-conversion of a trivial emission peak due to the interaction with the electromagnetic environment, which causes the emergence of an emission peak mimicking a topological $1e$ -radiation signal. Furthermore, we detect higher order tunneling events appearing as $4e$ - and $6e$ -radiation peaks, which are signatures of non-sinusoidal supercurrent oscillations in highly transparent Josephson junctions.

¹Parts of this chapter were published in a similar form in the Master Thesis of Dario Sufra "AC Josephson effect in InAs nanowire Josephson junction" (2018) and in the Master Thesis of Melissa Osterwalder "Probing Cd₃As₂ Nanowire Josephson Junctions with RF Techniques" (<https://nanoscience.ch>) both supervised by R. Haller *et al.*

6.1. Introduction

The measurement of Josephson radiation may have a profound and essential application for determining the existence of Majorana quasiparticle states in topological Josephson junctions (JJ). The search for perturbation protected quantum computation based on the non-Abelian exchange statistics of Majoranas initiated the search for these non-trivial JJs [70, 148, 149]. Since the opposing parities of Majorana doublet-states ensure a level crossing at superconducting phase differences $\varphi = \pm\pi, \pm 3\pi, \dots$ across the junction and consequently, the current-phase relation (CPR) in topological JJs is expected to be 4π -periodic [85, 150]. However, as previously explained in Ch. 2, fast equilibration triggered by quasiparticle poisoning or coupling to the surrounding trivial Andreev bound state spectrum, can result in a restoring of the trivial 2π -periodic Josephson effect. Therefore, potential topological JJs need to be measured on time scales shorter than the relaxation time, which is supposedly provided by directly probing the microwave emission spectrum of the junction [151]. The universal relation between the frequency f_J of the oscillating supercurrent and an applied dc voltage bias V is given by

$$\frac{f_J}{V} = \frac{q^*}{h}, \quad (6.1)$$

where q^* is the effective charge transferred across the junction and h is the Planck constant. We have seen in Ch. 2, that for trivial JJs the effective charge is a multiple of the Cooper pair charge, $q^* = n \cdot 2e$; whereas for topological JJs the effective charge is given by $q^* = e$. Although the relation given in Eq. 6.1 together with the expected charge granularity provides a clear distinction between the two JJ-flavors, many experimental aspects – such as weak emission strength, lifetime broadening, voltage noise, finite detection bandwidth, self-irradiation and down-conversion of the emission – pose a challenge to unambiguously prove the emergence of Majorana states in topological JJs [57, 58, 87].

In this chapter, we provide a broad overview of Josephson emission spectra for a rich diversity of JJs. Similar measurements are performed on a wide range of devices and we will now summarize the important quantities that define these experiments. In general, the emitted radiation signal is enhanced in an amplification chain and probed with a spectrum analyzer at room temperature as described in detail in Ch. 4. The power spectral density (PSD) of the radiation signal is collected in a specific bandwidth² around a center frequency f_{det} . In order to isolate the junction contribution from the background noise and to exaggerate the contrast, we typically normalize the PSD by shifting the minimal PSD value to zero and scaling the maximum value to 1 at each

²The bandwidth is set to either 20 MHz or 50 MHz, which qualitatively gives the same results.

detection frequency. The voltage bias V is controlled by the dc current bias I that flows through the resistively shunted junction to ground. The shunt resistor ensures a stable voltage drop across the junction after exceeding the critical current. The differential voltage is measured with standard lock-in techniques in a quasi-four-probe configuration and serves the differential resistance dV/dI via the current excitation. By numerically integrating dV/dI over the current we obtain the voltage drop V across the junction.

In Sec. 6.2 we investigate the dc characteristics and the emission spectrum of a dc SQUID formed by two Al/AlO₂/Al-tunnel junctions embedded in a superconducting loop. In Sec. 6.3, we turn our attention to gate tunable nanowire (NW) JJs where we first probe the ac Josephson effect in a Cd₃As₂ NW with superconducting Al leads by collecting the radiation signal and by detecting the response of the junction under irradiation with a microwave tone. Second, we trace the radiative behavior of an InAs NW JJ formed by locally removing its epitaxial Al half shell. In Sec. 6.4, we focus on JJs consisting of multi-dimensional materials. One of the junctions consists of a HgTe layer contacted with Nb leads, while the other one incorporates a WTe₂ flake in proximity to Pd stripes and MoRe contacts.

6.2. SIS junction

The device presented in Fig. 6.1 consists of two Al/AIO₂/Al JJs embedded in a superconducting loop, forming a dc SQUID. The SIS tunnel junctions are fabricated by a double-angle shadow evaporation technique with an intermediate oxidation step as described in Ch. 3. The launcher and the surrounding ground plane seen in Fig. 6.1 (a) are patterned simultaneously with the junctions and are expected to reduce microwave losses. The size of the SQUID loop is designed such that the current I_{flux} in the flux line running in parallel, is able to supply multiple flux quanta through the SQUID area, before the stripe switches to the normal state. By adjusting the overlapping area between the two Al layers shown in the zoom-in of Fig. 6.1(b), we ensure an overdamped junction behavior.

If the two junctions have the same critical current \tilde{I}_c , the maximum supercurrent across the SQUID is given by $I_c(\Phi) = 2\tilde{I}_c |\cos(\pi\Phi/\Phi_0)|$ [4], where Φ_0 is the flux quantum, $\Phi = B \cdot A$ is the magnetic flux through the loop area A for a given external magnetic field B , which is here produced by I_{flux} . The dark region in Fig. 6.2(a) indicates the superconducting state, where the periodic oscillation is dictated by the flux dependence of I_c . We attribute the non-vanishing supercurrent amplitude to slight asymmetries between the junctions.

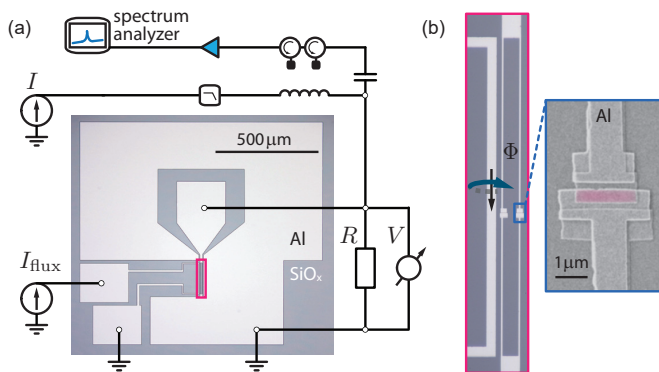


Figure 6.1. dc SQUID formed by Al/AIO₂/Al-tunnel junctions embedded in a radiation set-up. (a) Optical overview picture of the device. The flux current I_{flux} running parallel to the SQUID loop provides a the magnetic field for phase bias the junctions. The SQUID is shunted by a resistor ($R = 10 \Omega$). (b) Optical image (left) of the loop with an area $40 \times 200 \mu\text{m}^2$ and a SEM image (right) of one of the junctions. The overlapping tunnelling region is shaded in pink.

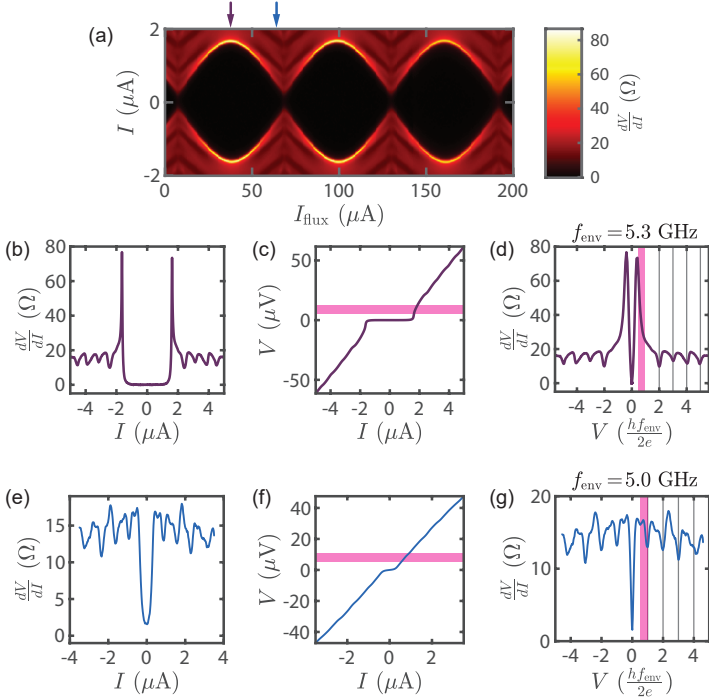


Figure 6.2. Flux dependence of the Al/AlO₂/Al-tunnel junction dc SQUID. (a) Differential resistance dV/dI as a function of current I and flux bias I_{flux} . (b)-(d) Switching behavior and IV -characteristics for $I_c = 1.6$ μA obtained at $I_{\text{flux}} = 38$ μA. (b) dV/dI as a function of I , (c) V as a function of I . (d) dV/dI as a function of V . (e)-(g) Switching behaviour and IV -characteristics for $I_c = 400$ nA obtained at $I_{\text{flux}} = 64$ μA. The pink shaded region in (c), (d), (f), (g) denotes the voltage range for the radiation measurements.

In the normal state in Fig. 6.2(a), we observe depression patterns in the differential resistance dV/dI that follow the shape of the oscillation of I_c , which are also clearly seen in the linecuts in Fig. 6.2(b) and 6.2(e). We plot these linecuts in Fig. 6.2(d) and 6.2(g) with respect to the voltage V across the junction and find that the dips occur at regular voltages $V = n h f_{\text{env}} / (2e)$ where, n is an integer number and f_{env} corresponds to the frequency of an environmental cavity. We therefore interpret these regular dips as self-induced Shapiro steps where their periodicity for $I_c = 1.6$ μA is given by $f_{\text{env}} = 5.3$ GHz, whereas for $I_c = 400$ nA an environmental cavity frequency of $f_{\text{env}} = 5$ GHz is found.

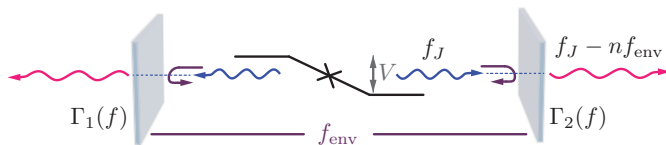


Figure 6.3. Illustration of self-induced Shapiro steps and the down-conversion of the Josephson radiation.

The emergence of self-induced Shapiro steps is the manifestation of fundamental properties of JJs: they are simultaneously radiation sources and sensors. The electromagnetic environment with which the JJ interacts is crucial for the radiative interplay. The environment can be modelled as a cascade of semi-transparent interfaces that lead to the formation of a cavity operating around the frequency f_{env} . When applying a finite voltage drop across the junction, microwave photons are generated that are then partially reflected back to the junction, as sketched in Fig. 6.3 by violet arrows, which leads to self irradiation. The effect becomes most pronounced close to the eigenfrequencies of the environmental cavity. In general, the surrounding microwave environment is hard to control, since stray capacitance, impedance mismatches, and the microwave response beyond the sample border need to be considered. Therefore the precise reason for the appearance of the environmental cavity is unknown. However, we suspect that the large ground plane surrounding the SQUID is part of the cavity mode. In the in-house built devices presented below we minimized the appearance of self-induced Shapiro steps by designing the electrodes to be short and progressively narrowing towards the junction.

From Fig. 6.2(c) and 6.2(f) we observe a smooth increase of the voltage versus I within the frequency window of 2.5–5 GHz. This bandwidth corresponds to the operation bandwidth of the amplification chain, as highlighted by the pink shaded regions for $2e$ -radiation. The possibility to apply a stable voltage bias in this range is required to accurately probe the frequency dependent emission spectrum.

The measured, normalized emission spectrum of the tunnel SQUID tuned to $I_c = 400$ nA is shown in Fig. 6.4(a) and overlaid with the expected peak position for the trivial $2e$ -radiation with a gray line. In addition to the clear emergence of $2e$ -radiation, we observe two emission peaks that move in parallel. We explain these features by the down-conversion of Josephson emission produced at higher voltages. The observed frequency shift, i.e., the spacing in V between the gray lines, matches with the environmental frequency $f_{\text{env}} = 5$ GHz inferred from the self-induced Shapiro step pattern. This is further illustrated in Fig. 6.4(b), by the highly accurate alignment between the measured emission

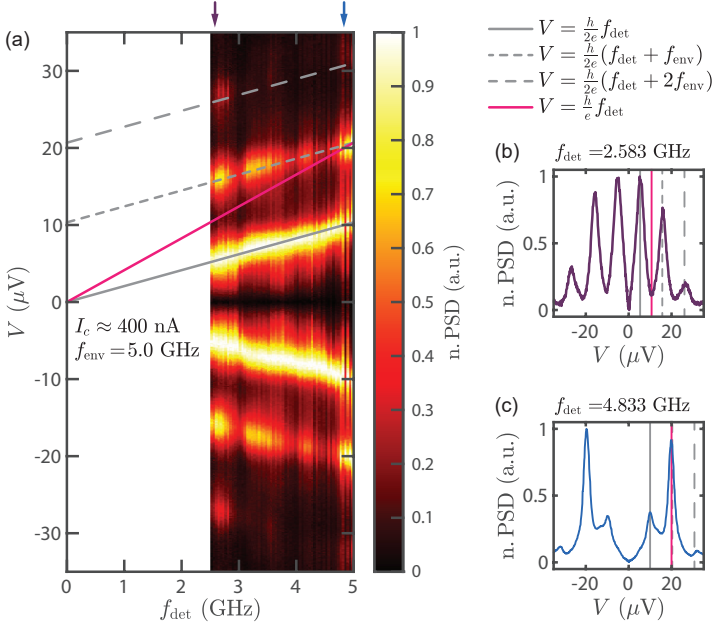


Figure 6.4. Emission spectrum of the tunnel SQUID at $I_c \approx 400$ nA. (a) Normalized power spectral density as a function of detection frequency f_{det} and voltage V across the junction. (b)-(c) Line cuts in the radiation map at fixed f_{det} as indicated by the purple and blue arrows in (a) respectively.

peaks and the dashed lines that represent the down-converted signals. The down-conversion can be described with a multi-photon process exciting an environmental mode as depicted in Fig. 6.3. The Josephson photon at frequency f_J (blue) is split in two lower frequency photons, one which stays in the cavity nf_{env} , and another that reaches the detector $f_J - nf_{\text{env}}$ (pink), causing an effective down-conversion of the Josephson emission.

At frequencies satisfying $f_{\text{det}} = f_{\text{env}}$ the down-converted $2e$ -radiation peak coincides with the position of the $1e$ -peak and hence can mimic the feature of a topological JJ. For example, in a line cut at $f_{\text{det}} = 4.833$ GHz presented in Fig. 6.4(c), the down-converted features appearing at the $1e$ -position dominate the trivial $2e$ -emission and can be misinterpreted as the signature of a topological junction.

Consequently, radiation measurements need to be performed over a wide range of frequencies to ensure one can accurately determine the slopes of the respective emission peaks as a function of voltage.

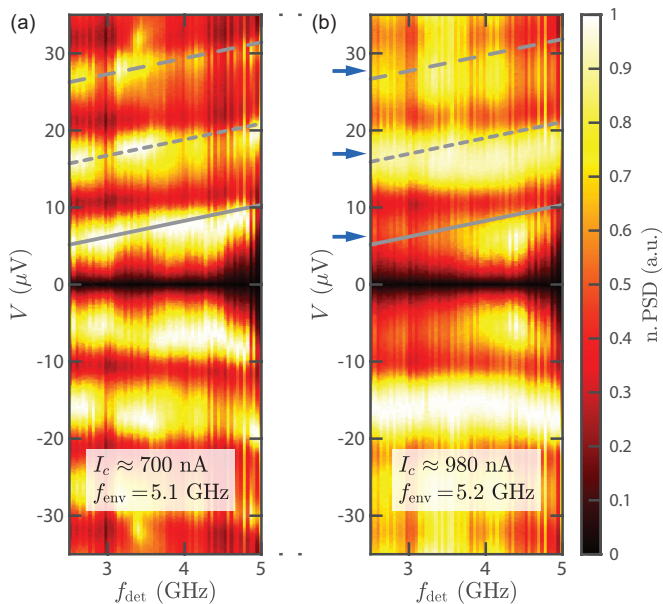


Figure 6.5. Emission spectrum of the tunnel SQUID with the expected resonance conditions overlaid for $2e$ -emission (gray) and its down-conversion (dashed) in (a) for $I_c \approx 700$ nA and in (b) for $I_c \approx 980$ nA. The blue arrows indicated non-dispersing emission peaks.

For increasing the critical currents we observe a progressive broadening of the radiation peaks, and a reduced voltage dependence in the emission spectrum, as can be recognized in Fig. 6.5. We attribute this weaker dispersion to enhanced voltage noise across the junction. As indicated by the pink bar in Fig. 6.2 (d), the IV -characteristics steepens in the measured frequency interval for larger critical currents and as a consequence the voltage becomes ill-defined, which results in broadband emission. Furthermore, the back-action from the microwave environment increases, as seen by the enhancement of the down-converted signal over the full frequency range.

We have successfully shown that we are able to measure Josephson radiation from a tunnel SQUID with critical currents ranging from 400–1000 nA and observe, in addition to the expected $2e$ -radiation peak, multiple down-converted radiation signals due to environmental back-action. In the next section we will investigate 1D nanowire SNS junctions with, in general, lower critical currents, resulting in a weaker absolute radiation signal. This makes measure-

ments more challenging from an experimental point of view. In contrast to the tunnel SQUID discussed here, in nanowire SNS JJs higher order $n2e$ -peaks (integer n denotes the order) may become visible based on the transparency of the channels in the junction.

6.3. 1D nanowire SNS junctions

In this section we present and discuss the experimental results obtained on gate tunable NW JJs. We will first focus on a weak link formed by Cd_3As_2 , which is a Dirac semimetal with ultrahigh carrier mobility, unique bulk Dirac cones and nontrivial surface states [152]. On this platform, the emergence of topological superconductivity has been claimed from Shapiro step measurements [153]. The second device consists of an InAs NW with an epitaxial Al half shell [100], where the JJ is formed by locally removing the Al clad. These types of junctions are one of the work horses in the search for the elusive Majorana fermions. It is predicted that topological superconductivity emerges in this material system upon applying a magnetic field along the wire axis [88, 154].

6.3.1. Cd_3As_2 nanowire Josephson junction

Cd_3As_2 NWs are placed by a random deposition technique on top of a highly p-doped Si/SiO₂ (500 μm /305 nm) wafer with pre-patterned Au markers and bonding pads. After removing the native oxide with Ar-milling, the NW is in-situ contacted by Ti/Al (3 nm/200 nm) electrodes in a quasi-four-probe

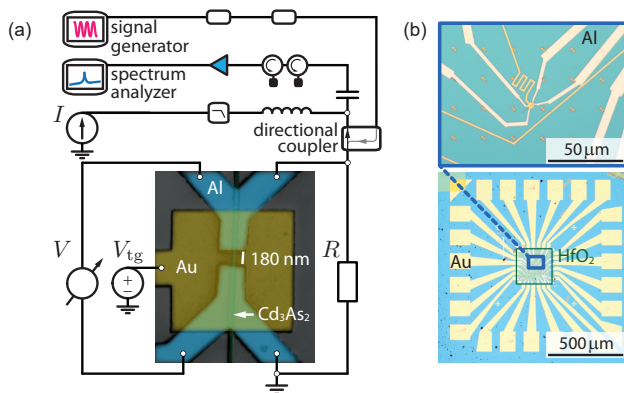


Figure 6.6. Cd_3As_2 nanowire Josephson junction formed by Al leads embedded in a radiation/irradiation set-up. (a) Colored SEM image of the device. The top gate electrode (yellow) is isolated from the junction by a 20 nm thick HfO_2 layer. The voltage V_{tg} applied on the Au gate structure allows to tune the charge carrier density. The junction is shunted by a resistor ($R = 10 \Omega$). (b) Optical image showing the direct (top) and indirect (bottom) surroundings of the device.

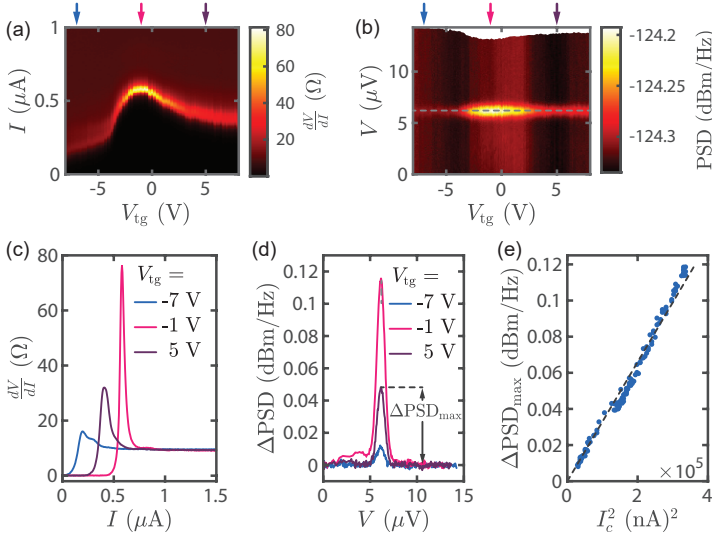


Figure 6.7. Gate dependence of the Cd_3As_2 nanowire. (a) Differential resistance dV/dI as a function of current bias I and top gate voltage V_{tg} . (b) Power spectral density (PSD) as a function of the voltage drop V across the junction and V_{tg} . The signal is collected at a fixed detection frequency $f_{\text{det}} = 3$ GHz. The gray dashed line indicates the expected $2e$ -peak position. (c) Line cuts in dV/dI at different voltages. (d) Line cuts in the PSD with subtracted background (Δ PSD) for different voltages. (e) Δ PSD_{max} (see (d)) versus the corresponding critical current squared (I_c^2).

configuration as seen in Fig. 6.6(a). The wire has a diameter of 50 nm and the junction length is 180 nm. The Al leads extend from the NW up to the inner border of the base structures. We cover this inner region, indicated by the green box in Fig. 6.6(b), with a 20 nm thick locally deposited HfO_2 gate-dielectric. A subsequently deposited Au top gate allows tuning of the charge carrier density. In addition to the radiation detection set-up, a signal generator is connected to the device via a directional coupler to irradiate the junction with microwaves.

In Fig. 6.7, we probe the response of the junction as a function of the top gate voltage V_{tg} , by sweeping the current bias while simultaneously measuring the differential resistance and the emission spectrum at a fixed detection frequency. The differential resistance as a function of current bias and gate voltage presented Fig. 6.7(a), reveals a clear continuous switching behavior. In contrast to the observations in Sec. 6.2, we find a stable resistance value

without features of self-induced Shapiro steps as can be infer from the linecuts presented in Fig. 6.7(c), which we attribute to the restructured lead architecture with omitted ground plane and short electrodes, continuously narrowing towards the junction.

We estimate the critical current I_c by identifying the position of the dV/dI peak at each gate voltage. An anomalous evolution of I_c is observed when sweeping the gate from negative to positive voltages; I_c first increases and then asymmetrically decreases again. This behavior contrasts with ordinary semiconductor JJs, which generally exhibit a steady increase of the critical current as a function of larger electric-field induced doping. The unusual gate response has been previously reported in long Cd_3As_2 NW JJs and has been proposed to originate from scattering mechanisms between surface and bulk states that give rise to dephasing [155]. In this case, increasing the electron density enhances the scattering which results in a suppression of the coherent Cooper pair transport, and hence leads to a reduction of the critical current. We inferred the normal state resistance R_N from measurements carried out in magnetic field with a large probe excitation in combination with a parallel resistor model. We denote $I_c R_N$ -products of $\sim 50 \mu\text{V}$ in the far negatively doped regime up to $\sim 100 \mu\text{V}$ at the maximal I_c position, which indeed points to the direction of gate dependent scattering mechanisms on the surface.

Fig. 6.7(b) maps the raw data of the collected radiation signal with respect to the top-gate voltage V_{tg} and voltage V across the junction. We observe that the emission peak remains visible throughout the whole gate range and aligns to a high degree with the expected $2e$ -peak position at $V = hf_{\text{det}}/(2e)$ (see the gray dashed line) with $f_{\text{det}} = 3 \text{ GHz}$. Besides the trivial $2e$ -emission, no additional spurious radiation peaks or signatures of high-order tunneling events appear. In Fig. 6.7(d), we present the background-subtracted linecuts in the emission spectrum at fixed voltages. Note that even for a relatively low critical current $I_c \approx 200 \text{ nA}$ at $V_{\text{tg}} = -7 \text{ V}$, the radiation power overcomes the noise floor.

In Fig. 6.7(e) we plot the effective emission peak height versus the corresponding extracted critical current squared. We recognize a clear quadratic dependence between the emission strength and I_c . If we naively think of the junction acting as sinusoidal ac current source with amplitude I_c that is in parallel with a resistor \tilde{R} , a power $P = \tilde{R}I_c^2/2$ will be dissipated in the circuit. In the full experimental circuitry, a fraction of the power will be dissipated within the amplification chain and the shunt resistor. The other fraction is dissipated across the 50Ω -termination in the spectrum analyzer, which is directly proportion to the measured PSD. Consequently, the PSD height is proportional to the current squared. In order to quantitatively relate the measured PSD to I_c , the full transfer function between the junction and the detector needs to be considered. In of case a non-sinusoidal ac source, reflecting a skewed current-phase relation (CPR), the trivial and higher-order emission peak heights would

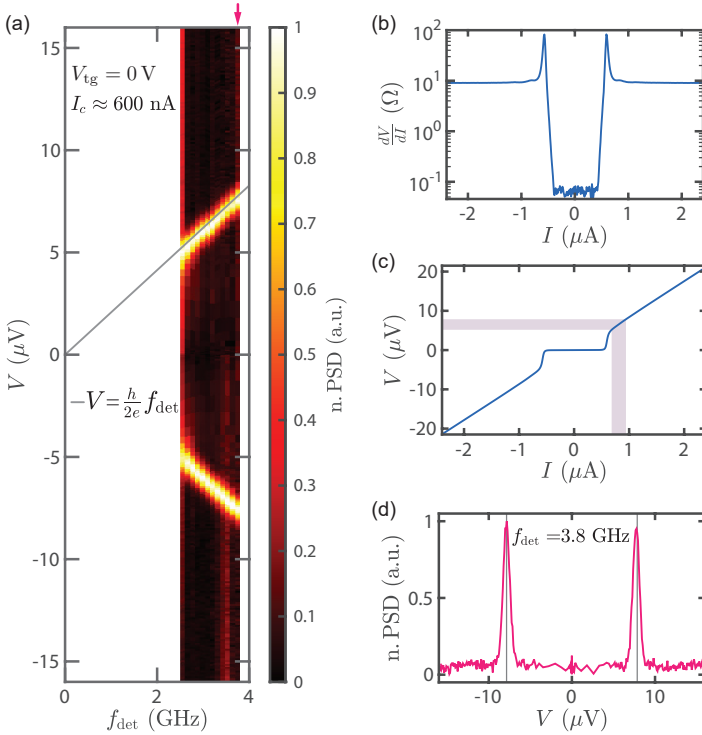


Figure 6.8. Emission spectrum of the Cd_3As_2 device for $I_c \approx 600$ nA obtained at $V_{\text{tg}} = 0$ V. (a) Normalized radiation spectrum overlaid with the expected position of the $2e$ -emission peak. (b) Differential resistance dI/dV in log-scale as a function of current bias I . (c) IV -curve with the current and voltage range that produces $2e$ -radiation in a frequency window from 2.5–3.8 GHz as indicated by the violet shading. (d) Line cut in the normalized radiation map at a fixed detection frequency.

correspond to the Fourier amplitudes of the CPR. In Sec. 6.3.2 and 6.4.2, we make use of the heuristically found proportionality between the peak height and the current amplitude to obtain the relative ratios between the Fourier amplitudes.

In a next step, we investigate the Josephson radiation spectrum at a constant top gate voltage $V_{\text{tg}} = 0$ V, which corresponds to a critical current $I_c \approx 600$ nA. In Fig. 6.8(a), the normalized power spectral density is plotted as a function of the voltage bias V and the detection frequency f_{det} in the

range 2.5 – 3.8 GHz, that is limited by the measurement set-up. The detected radiation features are symmetric in voltage and solely determined by trivial single Cooper pair transport. No signatures of topological $1e$ -transfer events or higher-order processes appear. In agreement with the lack of self-induced Shapiro steps in the dV/dI , no features of down-conversion emerge. The observed emission peaks appear sharp with a base width of $\sim 2 \mu\text{V}$, as can be inferred from the line cut presented in Fig. 6.8(d). We attribute this to a stable voltage drop across the junction, which by virtue of a noise picture is reflected in the rapid switching behavior (see Fig. 6.8(b) and (c)) and the nearly vanishing residual resistance in the superconducting state as presented in log-scale in Fig. 6.8(b). The fact that the IV -curve becomes steep just below the detection bandwidth for trivial emission, as indicated in 6.8(c), makes the voltage drop ill-defined for the voltage range that could produce features of higher-order tunnelling events. These higher-order process could have been expected for the short semimetal section investigated here.

We now direct our focus to the investigation of the ac Josephson effect by measuring the Shapiro step pattern. The junction is irradiated by a microwave tone of fixed frequency $f = 2$ GHz at variable output power P of the signal generator. The driving signal is applied to the rf line connecting the device to the amplification chain, as seen in Fig. 6.6. We probe the differential resistance dV/dI as a function of current bias and P for a constant gate voltage $V_{\text{tg}} = 0$ V. The resulting map shown in Fig. 6.9(a), reveals the characteristic plateaus of constant current and zero dV/dI (and constant V) represented by the elongated dark regions. It can be observed that with increasing the drive power, the plateau of the 0-voltage state becomes narrower and eventually disappears, while higher-order Shapiro steps progressively emerge. The Shapiro steps can be identified as dips in the dV/dI , as seen in the line cut for $P = -18$ dBm presented in Fig. 6.9(b). Here, the first and the second steps are indicated with black arrows. In Fig. 6.9(d) we present the IV -curve obtained by integrating dV/dI for different drive powers. The voltage axis presented in units of the Shapiro step voltage with $f = 2$ GHz nicely matches the measured voltage steps. The development of the various voltage plateaus depends on the drive power. By numerically differentiating the interpolated IV -curves we can extract the differential conductance dI/dV , which is presented in Fig. 6.9(c) as function of V and P . With this visualisation technique developed by Joost Ridderbos [51] no binning is required and the resolution is maintained. The voltage plateaus appear as lines in the color map, whereas their intensity reflects the width of the Shapiro step.

In parallel with the Shapiro steps, we measure the emission spectrum of the junction for a fixed detection frequency. In Fig. 6.9(e), which presents the normalized emission spectrum as a function of V and P , we observe replicas of the $2e$ -peak at large drive power, which are shifted up in voltage by multiples of the drive tone. Since these features are not present at low drive powers we refer

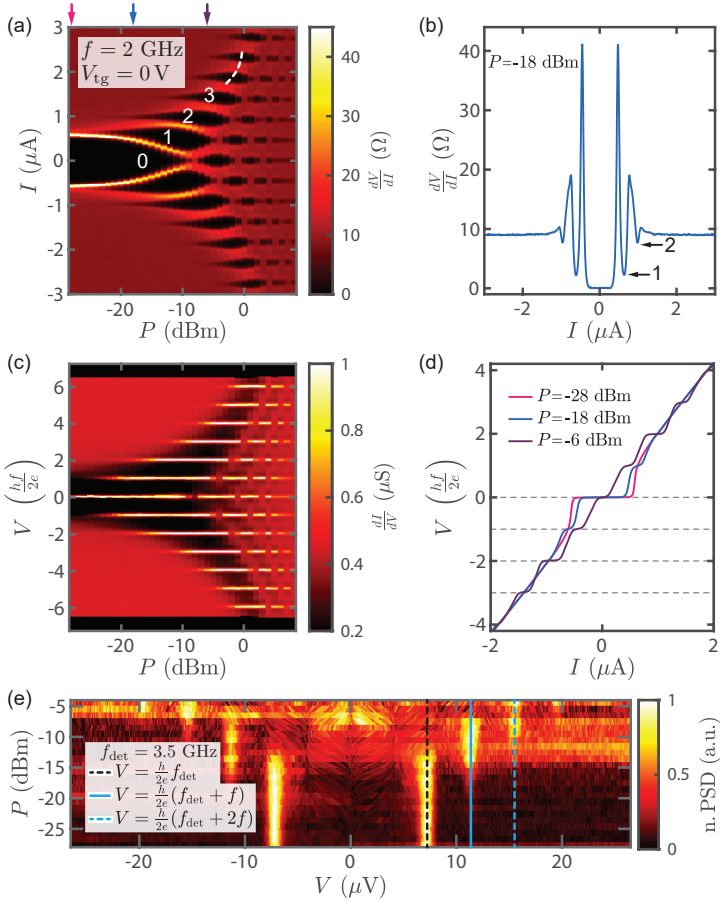


Figure 6.9. Shapiro step measurement performed on the Cd₃As₂ device by irradiating the junction with a microwave tone of frequency $f = 2$ GHz. (a) Differential resistance dV/dI as a function of drive power P and current bias I . (b) Line cut in dV/dI for a fixed power value. (c) Numerically deduced differential conductance dI/dV as a function of P and the voltage V in units of the Shapiro step voltage with $f = 2$ GHz. (d) IV -curves obtained by integrating dV/dI over I for different irradiation powers. (e) Normalized power spectral density (n. PSD) as a function of V and P . The signal is collected at a fixed detection frequency $f_{det} = 3.5$ GHz. The black dashed line indicates the expected $2e$ -peak position, whereas the blue lines indicate its ‘forced’ down-conversion.

to them as ‘forced’ down-conversions of the Josephson emission. The fact that, in contrast to measuring radiation, Shapiro step measurements heavily drive the system out-of-equilibrium and frequency mixing between the Josephson emission and the drive tone arises [114], makes the extraction of 4π -periodic CPR contributions from plateau size analysis a poor identifier of topological superconductivity and will be omitted here.

For the first the emission spectrum of a Cd_3As_2 nanowire has been measured. Although a topological emission peak is predicted for this material, we have only measured trivial $2e$ radiation. The $1e$ emission intensity might be limited by scattering potentials on the surface, which could strongly reduce the transparency of the topological modes living on it. This explanation is consistent with the observation of the anomalous gate effect. In addition, we have obtained a very clean radiation signal and Shapiro step pattern where environmental modes were not observed, in contrast to the $\text{Al}/\text{AlO}_2/\text{Al}$ tunnel SQUID. We partly explain this cleaner electromagnetic environment to an omitted ground plane and an optimized design of the on-chip electrodes. Importantly, we denote a quadratic proportionality between the supercurrent amplitude and the emission intensity.

6.3.2. InAs nanowire Josephson junction

We now move to a device where a single InAs NW with an epitaxial Al half shell is deterministically deposited on top of a pre-patterned bottom gate structure made of Ti/Au (5 nm/20 nm), in turn, covered with a 20 nm thick HfO_2 dielectric. The gate structure consists of a thin middle gate flanked by two large area side gates, extending beyond the length of the NW as seen in Fig. 6.10(b). The Josephson weak link is formed by removing the 7 nm thick Al half shell just above the middle gate using a wet etching procedure. The resulting bare InAs section, which is seen in Fig. 6.10(c), has a length of 55 nm. Here, the bare InAs section is enclosed between the Al covered nanowire and the bottom-gate structure, which ensures a strong capacitive gate coupling. The NW tails are contacted by sputtering NbTiN , after removing the native oxide by in-situ Ar-milling. The electrodes are designed to be short and homogeneously increasing in width to reduce losses and suppress spurious resonances. An overview of the final device is shown in Fig. 6.10(a).

Here, we aim to investigate Josephson transport in a highly transparent regime, which is obtained by applying positive voltages on the three bottom gates to accumulate charge carriers and open-up a transport channel. In the following, we limit our discussion to the gate configuration in which the two outer gates are set to $V_{\text{og}1} = V_{\text{og}2} = 4$ V and the middle gate to $V_{\text{mg}} = 6$ V. This gating potential was optimized for obtaining the highest critical current. The corresponding differential resistance measured as a function of current bias I , presented in Fig. 6.11(b), reveals a critical current $I_c \approx 120$ nA. We

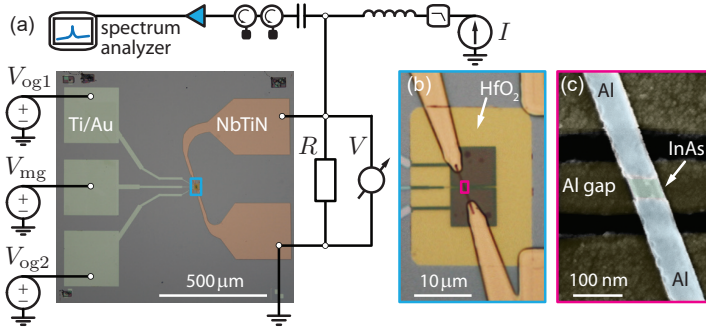


Figure 6.10. InAs nanowire Josephson junction embedded in a radiation set-up. (a) Three bottom gates allow tuning of the junction. The nanowire is contacted by NbTiN leads and shunted by a resistor ($R = 10 \Omega$). (b) The locally deposited 20 nm thick HfO_2 -layer isolates the gate structure consisting of a thin middle gate and two large-area side-gates. (c) SEM image of the nanowire junction, formed by locally etching the epitaxial Al half-shell. The etched region is centered over the middle gate.

observe a non-vanishing resistance value for $I = 0$, which we attribute to finite temperature effects and current/voltage noise in the system. The device was measured in the BlueFors set-up with an amplification chain providing a bandwidth of 3 – 7.7 GHz. This allows to probe the emission spectrum in a wide voltage range, as indicated on the IV -curve in Fig. 6.11(c) with the violet shading for $2e$ -radiation.

Fig. 6.11(a) presents the high resolution emission spectrum³, which was collected in a time window of 80 h with 1 s per data point averaging time. We detect trivial $2e$ -emission that appears as broad white lines due to the saturated color-scale. In addition, we observe two faint emission traces at lower voltages with clearly different slopes compared to the $2e$ -emission. We find a remarkable agreement between this feature and the expected peak positions that corresponds to $4e$ -radiation, and we therefore attribute these features to a higher-order inelastic Cooper-pair tunnelling event that incorporates four electrons.

The appearance of higher-order tunnelling events in this device is the direct manifestation of a highly transparent junction. Assuming that the emission peak height scales with the contribution to the total supercurrent, we can

³The background and the color-scale are adjusted such that features are optimally visible.

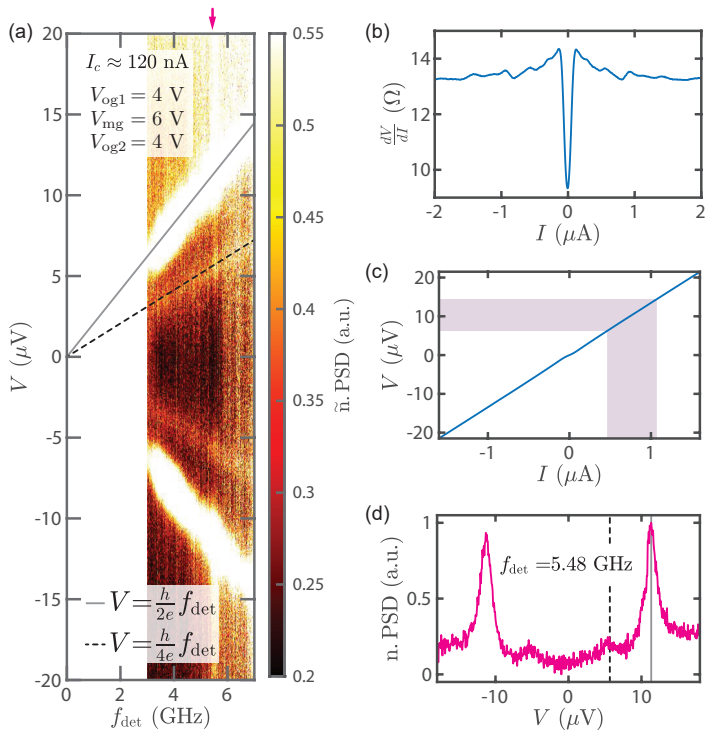


Figure 6.11. Emission spectrum for the InAs nanowire Josephson junction $I_c \approx 120$ nA. (a) Normalized radiation spectrum with the gray line indicating the expected position of the $2e$ -emission peak and the black dashed line tracing the emission of a $4e$ -peak. (b) Differential resistance dI/dV as a function of current bias I . (c) IV -curve with the current and voltage range that produces $2e$ -radiation in a frequency window from 3 – 7.7 GHz is indicated with the violet shading. (d) Normalized radiation signal obtained at a fixed detection frequency.

estimate the ratio of the Fourier amplitudes of the higher order processes as

$$\frac{A_2}{A_1} \propto \sqrt{\frac{\Delta\text{PSD}_{\text{max}2}}{\Delta\text{PSD}_{\text{max}1}}}. \quad (6.2)$$

In the linecut shown in Fig. 6.11(d), the signatures of $4e$ -radiation can be recognized as minor peaks between the two main $2e$ -emission peaks. From this we estimate a relative peak height ratio $\Delta\text{PSD}_{\text{max}2}/\Delta\text{PSD}_{\text{max}1} \approx 0.05$ between

the $4e$ and $2e$ signal, from which we obtain $A_2/A_1 \approx 0.22$. On the same nanowire platform, very similar A_2/A_1 -ratios have been reported in Ref. [54] and are attributed to an averaged transparency of $\tau \approx 0.8$. This implies that the InAs NW JJ investigate here might have a transparency of the same order. However, we want to stress that the modest analysis used here is only a rule of thumb. Further developments where we take into account the frequency dependence of the relative ratios A_2/A_1 and the voltage dependent background noise, would offer a more accurate estimation.

Besides trivial emission we collect $4e$ -radiation signals from the InAs NW junction, which implies coherence between subsequent Cooper pair transfer events. By virtue of a heuristic model, we can estimate the relative ratio of the Fourier components and hence obtain direct access to the CPR. In contrast to conventional rf/dc SQUID methods to probe the CPR, radiation measurements can be even performed in large magnetic fields and are therefore highly interesting for probing surface supercurrents. The observed higher-order emission stemming from a supercurrent amplitude of $A_2 \approx 30$ nA, further demonstrates the sensitivity of our radiation set-up.

6.4. 2D/3D SNS junctions

In this section we focus on the experimental results obtained from JJs made of 2D/3D materials. The first sample discussed here originated from a collaboration with the group of Prof. Dieter Weiss: a HgTe junction with Nb leads, which was fabricated and pre-characterized by Ralf Fischer at the University of Regensburg. HgTe is a 3D topological insulator [156], in which the emergence of Majorana fermions is theoretically predicted when the surface states interact with an ordinary superconductor [71]. Therefore, this material system is a highly promising platform to observe the non-trivial 4π -periodic Josephson effect [57, 81, 82]. The second, in-house built device, was measured together with A. Kononov, who fabricated the device together with M. Endres. The Josephson element investigated here incorporates a WTe₂ flake with Pd induced superconductivity [157]. Since WTe₂ is predicted to be a higher-order topological insulator with 1D-hinge states [157–159], it is as well a particularly promising candidate for hosting topological superconductivity.

6.4.1. HgTe Josephson junction

The following brief description of the HgTe JJ device is adapted from the fabrication recipe provided by Ralf Fischer. Fig. 6.12(c) illustrates a cross-section of the heterostructure, in which the 80 nm thick HgTe layer is capped by CdHgTe/CdTe buffer layers on a GaAs/CdTe growth-substrate [160]. A stripe-shaped MESA structure with a width of 2.7 μm , as seen in Fig. 6.12(b), is formed by chemical wet etching. After locally removing the capping layer in a subsequent wet etching step, these contact regions are cleaned by Ar-milling before in-situ depositing Ti/Nb (3 nm/100 nm) leads, which are protected by a 3 nm thick Pt layer. The length of the JJ is defined by a 200 nm contact separation and a top-gate allows tuning of the charge carrier density. An overview of the device together with the microwave set-up can be seen in Fig. 6.12(a). Because wire bonding on the CdTe substrate is difficult, large bond terminals are patterned for potential indium press contacts, which are far away from the junction. Furthermore, the Nb supply lines from the bond region to the junction are narrow all the way.

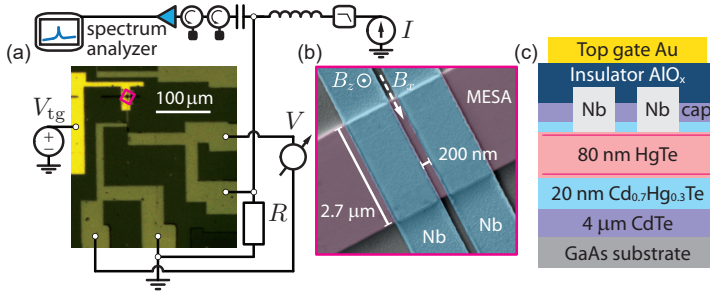


Figure 6.12. HgTe Josephson junction embedded in a radiation set-up. (a) The voltage V_{tg} applied on the Au top gate structure (yellow) allows to tune the charge carrier density. The MESA is contacted by Nb leads and shunted by a resistor ($R = 10 \Omega$). (b) SEM image of the junction. (c) Cross-sectional schematic of the junction. Ralf Fischer from the University of Regensburg took the pictures and fabricated the device.

The differential resistance dV/dI is presented in Fig. 6.13(a) and is measured as a function of current bias I and top gate voltage V_{tg} . We infer a weak gate dependence of the critical current, with a range $I_c \approx 280 - 420$ nA. The line cut taken at $V_{tg} = 0$ V shown in Fig. 6.13(b), reveals a smooth switch behavior and the emergence of a potential self-induced Shapiro step, indicated with the pink arrow. The corresponding IV -curve is shown in Fig. 6.13(c).

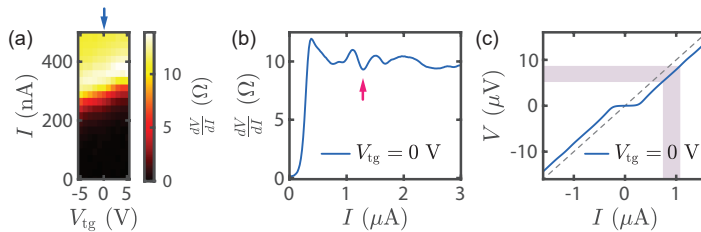


Figure 6.13. Gate dependence of the HgTe junction. (a) Differential resistance dV/dI as a function of current bias I and top gate voltage V_{tg} . (b) dV/dI in response to I at $V_{tg} = 0$ V. The pink arrow indicates a potential self-induced Shapiro step. (c) Voltage V across the junction obtained by integrated dV/dI as a function of I . The gray dashed line indicates the linear behavior of a 10Ω resistor and the violet shading corresponds to the current and voltage range that produces $2e$ -radiation in a frequency window from $2.5 - 4$ GHz.

We again investigate the emission spectrum of the junction, for which the experimentally available frequency range for $2e$ -radiation is highlighted on the IV -curve in the violet color in Fig. 6.13(c). We would like to note that the emission spectrum stays qualitatively unchanged for different gate voltages and we therefore limit our subsequent discussion to the $V_{\text{tg}} = 0$ V configuration. The normalized radiation map, shown in Fig. 6.14(a) is taken at $V_{\text{tg}} = 0$ V and includes a plethora of features. First of all, we observe the appearance of a clear $2e$ -emission peak indicated by the black solid line. Second, we notice bright blobs at higher voltages which one might mistake for a peak corresponding to $1e$ radiation. However, upon careful inspection over the measured frequency range, these features do not match with the slope of the the expected $1e$ -radiation (shown in green), and this allows us to rule out the observed feature as signatures of a 4π -periodic supercurrent contribution. Instead, we attribute the high-voltage emission features to down-converted $2e$ -radiation with two environmental frequencies, $f_{\text{env}1} = 3.2$ GHz and $f_{\text{env}2} = 5.3$ GHz. The latter frequency is also observed as a self-induced Shapiro step marked in Fig. 6.13(b). Furthermore, a broadband emission peak emerges at the voltages indicated by the gray arrows in Fig. 6.14(a). The lowest peak (solid gray arrow) largely coincides with the expected peak position for a $4e$ -radiation signal, however the slope of the peak seems not to match (gray line). The second peak at higher voltage (dashed gray arrow) has a similarly horizontal shape. Due to the limited frequency range and the relatively large peak widths, we cannot draw any further conclusions from these additional radiation peaks. The diversity in this emission spectrum might originate from suboptimal design of the on-chip contact electrodes.

By measuring the voltage dependent emission at elevated temperatures and at a fixed detection frequency, we observe that the down-converted peaks weaken and a more conventional spectrum is obtained, as seen in Fig. 6.14(b). A similar evolution can be seen in Fig. 6.14(c), where we apply an in-plane magnetic field that points perpendicular to the direction of the current, as illustrated in Fig. 6.12(b) by the B_x -arrow. In both cases we observe a decrease of the main $2e$ -peak heights, corresponding to a reduction in critical current. In addition, we also observe diminishing environmental radiation peaks with increased temperature and magnetic field, which can either be the result of the reduced strength of self-irradiation (because of the smaller critical current), or from temperature and magnetic field dependent changes in the electromagnetic environment. Although not shown in this work, we also investigated the emission spectrum as a function of an in-plane magnetic field that points along the current direction. Here, the goal was to thread a flux quanta through the cross-sectional junction area, which could give rise to the Little-Parks effect [161] due to the potential presence of superconducting surface states. However, the evidence of the effect is still illusive since our experimental observation were suffering from induced noise, while measuring in magnetic field.

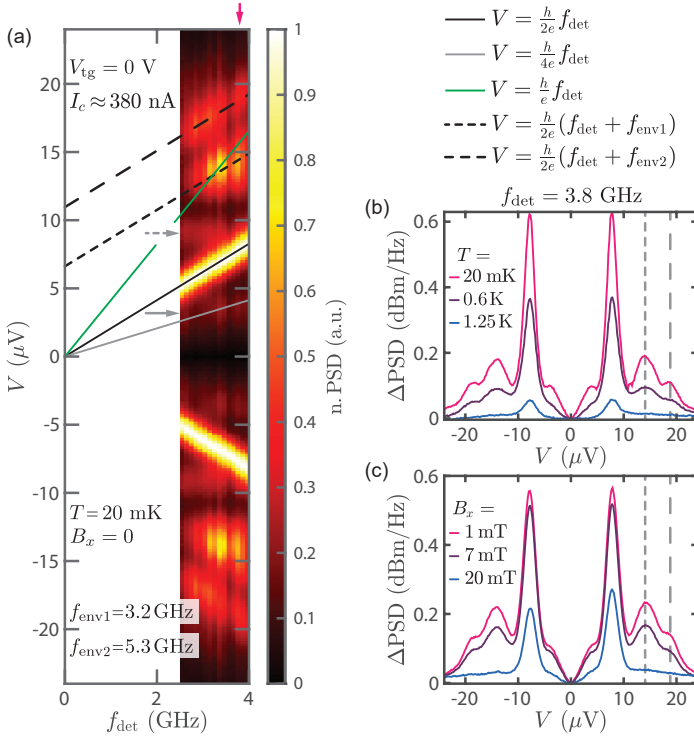


Figure 6.14. Emission spectrum of the HgTe junction at $I_c \approx 380$ nA. (a) Normalized radiation spectrum overlaid with the expected position of the $2e$ -emission peak (black) and the gray line traces the one of the $4e$ -peak. The two dashed black lines running parallel to the $2e$ -emission peak indicate the down-conversion of the signal produced at higher voltages for different environmental frequencies $f_{\text{env}1}$ and $f_{\text{env}2}$. (b) Temperature dependence of the emission spectrum obtained at a fix detection frequency with subtracted background. (c) In-plane magnetic field dependence of the emission spectrum obtained at a fix detection frequency with subtracted background. The field B_x is aligned parallel to the contacts as indicated in Fig. 6.12.

In Fig. 6.15(a) we look at dV/dI versus I and the out-of-plane magnetic field B_z . A clear Fraunhofer-like pattern emerges, however a strong increase in the noise level is observed compared to measurements without an applied magnetic field. This noise reduces the maximum value of I_c and ‘smears out’ the switching behaviour: for the maximal critical current, the maximum in dV/dI

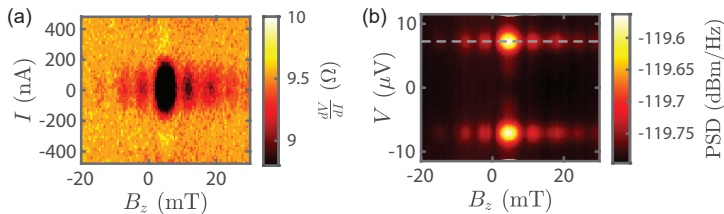


Figure 6.15. Dependence on the out-of-plane magnetic field B_z at $V_{tg} = 0$ V. (a) Differential resistance dV/dI as function of current bias I and B_z . (b) B_z -dependent emission spectrum is obtained at a fix detection frequency $f_{det} = 3.5$ GHz and plotted with respect to the voltage V across the junction. The dashed line indicates the expected $2e$ -peak position. The offset in B_z likely originates from flux trapping.

barely reaches the 10Ω shunt resistor value, contrasting the stronger previously observed peak in Fig. 6.13(b). Although our past efforts have already greatly improved the set-up, we attribute this noise to the power supplies of the magnet and pick-up on the magnet leads. In strong contrast to the more noisy lock-in measurement, a much cleaner Fraunhofer-like pattern is observed in the simultaneously measured radiation signal shown Fig. 6.15(b), which implies that the voltage drop across the junction is not that much affected. The discrepancy between the rf and dc readings might be explained by fluctuations on the ground potential together with a finite RC -time on the dc side. Further investigations have to be performed to eliminate the cross-talk between the magnet system and the measurement equipment.

6.4.2. WTe_2 Josephson junction

We now arrive at the last device that is investigated in this chapter, namely a top-down fabricated WTe_2 JJ. The following brief description of the WTe_2 JJ is adapted from the fabrication recipe developed by Artem Kononov and others. The 2D WTe_2 consists of a single crystal with a thickness of ~ 22 nm, which corresponds to ~ 31 single layers. To form Josephson junctions with WTe_2 , we used Pd-induced superconductivity that emerges at the interface between the WTe_2 crystal and the metal [157, 162]. First, Ti/Pd ($3 \text{ nm}/40 \text{ nm}$)⁴ stripes are patterned on top of a p-doped Si/SiO₂ ($500 \mu\text{m}/295 \text{ nm}$) substrate. The stripes have a width of $3 \mu\text{m}$ and a spacing of $1 \mu\text{m}$, defining the length of the studied junction. In the next step, the WTe_2 crystal covered with a hBN protection flake, is stacked on top of the Pd stripes using a standard polymer

⁴Ti acts as a sticking layer.

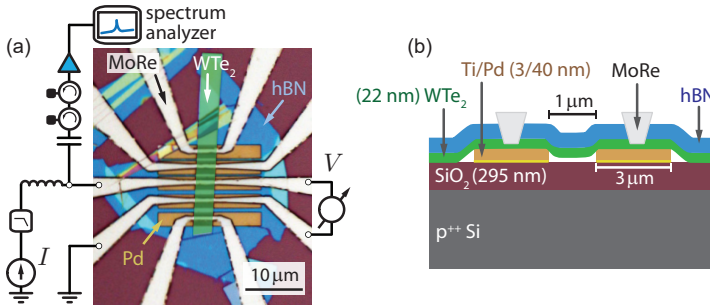


Figure 6.16. WTe_2 Josephson junction embedded in a radiation set-up. (a) The hBN covered WTe_2 flake is placed on top of Pd strips and side-contacted by MoRe leads. (b) Cross-sectional schematic of the junction. Device fabrication and imaging was performed by Artem Kononov.

pick-up technique [103]. Both the exfoliation and the stacking have been performed under nitrogen atmosphere in an oxygen free glovebox to avoid WTe_2 flake oxidation. In the last step, the superconducting contacts to the WTe_2 are formed by sputtering MoRe following a local plasma etching of hBN. This approach employs the standard recipe for making edge superconducting contacts to graphene [104]. The main idea of this design is to combine the advantage of the highly transparent Pd-mediated WTe_2 Josephson junctions, with fully superconducting contacts that minimize loss for the radiation measurements. An optical image of final device with a schematic measurement set-up, and an illustration of the cross-section of the junction are provided in Fig. 6.16(a) and (b) respectively. Due to the expected low normal state resistance on the order of $\sim 2 \Omega$ for these devices, the previously used shunt resistor is omitted in the microwave set-up.

In Fig. 6.17(b), we plot the measured differential resistance dV/dI as a function of current bias I for three different temperatures, which shows characteristic Josephson junction behavior. At base temperature $T = 20 \text{ mK}$ the dV/dI shows hysteretic behavior: When the current bias is swept from $I = 0$ to higher values, the junction maintains in the superconducting state up to the critical current $I_c \approx 9 \mu\text{A}$. Decreasing the current bias again leaves the junction in the normal state until the re-trapping current $I_r \approx 4 \mu\text{A}$ is reached. While this behaviour is typical for underdamped Josephson junctions, it could also originate from overheating in the normal state due to high critical current [163].

The corresponding IV -curve in Fig. 6.17(c) reveals that the voltage range relevant for $2e$ -emission in a detection bandwidth $3.2 - 4.2 \text{ GHz}$ falls into the hysteretic regime of the junction where the junction cannot be operated as a

radiation source. We overcome this problem by increasing the temperature. At $T = 350$ mK the critical current has shrunk to $I_c \approx 1.8 \mu\text{A}$ and the switching appears symmetric around $I = 0$ as seen by the blue trace in Fig. 6.17(b). The corresponding IV -curve shown in blue in Fig. 6.17(c) exhibits a smooth voltage increase, which corresponds to an overdamped junction desirable for properly measuring the Josephson emission spectrum.

In Fig. 6.17(a) the emission spectrum of the WTe₂ junction is presented. The color scale is confined to the lower 10% of the spectrum to enhance the visibility of the faintest measured features. We overlay the map with the expected peak position for inelastic Cooper pair tunnelling events, incorporating the following effective charges: in black $q^* = 2e$, in gray $q^* = 4e$ and in pink $q^* = 6e$. We note a good agreement between the measured peaks evolution and the expected behavior, with a tendency for the experimental peaks to lay slightly below the expected voltages. We speculate that this slight discrepancy in the voltage peak positions originates from imperfect measurements of the differential resistance.

We can estimate the individual contributions of the different orders of Cooper pair tunneling to the total supercurrent, by looking at amplitudes of the corresponding emission peaks following the approach described in Sec. 6.3.2. Fig. 6.17(d) shows the emission spectrum at a fixed frequency in the full n. PSD range. The spectrum is dominated by the $2e$ -peaks at $V \sim \pm 8 \mu\text{V}$, which flank the ~ 6 times smaller $4e$ -peaks at $V \sim \pm 4 \mu\text{V}$. The $6e$ -peaks, highlighted with pink arrows in the insert, have an amplitude that is ~ 20 times smaller than the $2e$ -peaks. Employing the heuristic Eq. 6.2 we find a Fourier amplitude ratio $A_2/A_1 \approx 0.4$ for the first two harmonics, and similarly a ratio $A_3/A_1 \approx 0.22$.

In the following, we compare these Fourier amplitudes ratios with theoretical predictions for different transport regimes: a ballistic weak link with a perfect transmission $\tau = 1$ has a saw-tooth CPR, yielding decaying Fourier amplitudes for increasing order k as $A_k \propto 1/k$ [43]. Hence, the expected ratios are $A_2/A_1 = 0.5$, $A_3/A_1 = 0.33, \dots$. On the other hand, for a diffusive weak link in the short junction limit, the amplitudes decay as $A_k \propto 1/k^2$ [43] and a forward skewed CPR emerges. Here, the averaged junction transparency is given by $\tau \approx 0.8$ and the ratios progress as $A_2/A_1 = 0.25$, $A_3/A_1 = 0.11, \dots$

Previously, a similar highly non-sinusoidal CPR in junctions of similar length has been linked to topological modes [164, 165]. Furthermore, the topological states are expected in our sample for several reasons. First, WTe₂ is believed to be a higher-order topological insulator hosting 1D edge states with a demonstrated contribution to Josephson transport [157–159]. Second, the sample has sufficient thickness to host topological Fermi arc surface states [166], which were previously connected with the appearance of fractional Shapiro steps [167]. We also want to emphasize that the previous analysis and conclusions are not invalidated by the elevated temperature at which measurements were performed. On the contrary, for an ordinary Josephson junction higher-

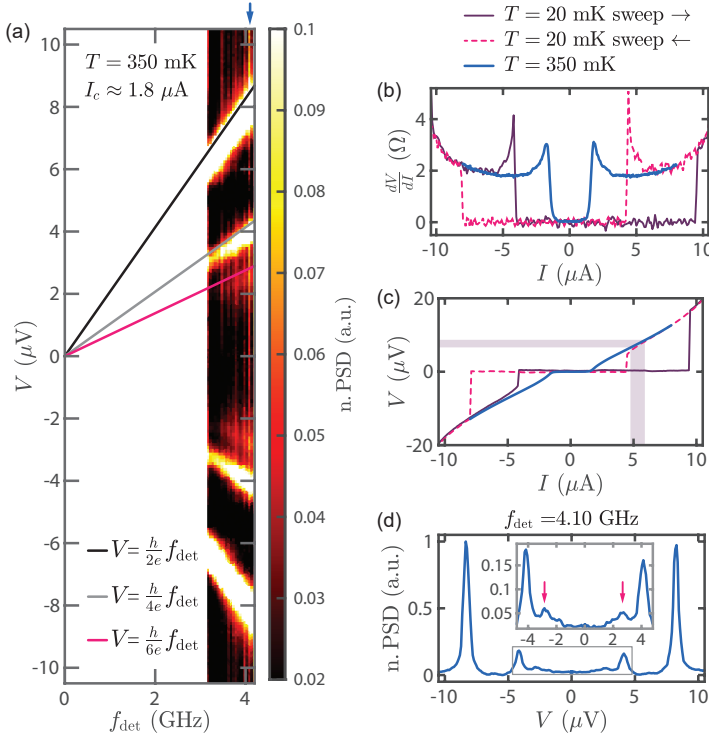


Figure 6.17. Emission spectrum of the WTe₂ Josephson junction obtained at elevated temperature ($T = 350$ mK). (a) Normalized radiation spectrum (n. PSD) for $I_c \approx 1.8$ μA overlaid with the expected positions of the $2e$ -emission peak (black), $4e$ -emission peak (gray) and $6e$ -emission peak (pink). Values above 0.1 are saturated in the color plot. (b) Differential resistance dV/dI as a function of current bias I at different temperatures and sweep directions. The blue curve corresponds to the dc characteristics of the map shown in (a). (c) IV -curves measured at the different temperatures and sweep directions. The violet shading indicates the current and voltage range that produces $2e$ -radiation in a frequency window from 3.2 – 4.2 GHz. (d) Line cut in n. PSD for a fixed detection frequency.

order Fourier components are decaying faster with the temperature [43, 54], suggesting an even stronger representation of the higher order processes if the sample could have been measured at base temperature. Nonetheless, we cannot exclude that a part of the much higher supercurrent at the base tem-

perature ($I_c(20 \text{ mK}) \approx 9 \mu\text{A}$ vs $I_c(350 \text{ mK}) \approx 1.8 \mu\text{A}$) is hosted by diffusive bulk modes.

To sum up, we studied Josephson radiation from WTe_2 with highly transparent superconducting contacts, provided by Pd induced superconductivity in WTe_2 . In the emission spectrum we observe radiation peaks up to the 3-rd order, with amplitudes ratios that suggest the junction is close to the ballistic limit. We connect this observation with the potential contribution from topological states in WTe_2 .

6.5. Conclusion

We have developed a measurement set-up for sensing the microwave emission spectrum of Josephson junctions in a broad frequency range. A superiority of the presented technique compared to the more conventional characterization of Josephson elements is evident since we gain direct access to the Fourier amplitudes that appear as higher-order emission bands. Another strength of this read-out scheme lays in the simplicity from a device point of view. No loop or additional junction needs to be integrated to the circuitry, which makes the method particularly powerful for measurements in large magnetic fields. Since these large fields are essential with respect to the investigation of topological surface states, this is a strong motivator for continued efforts improvements to both set-up and sample in our lab.

By directly measuring the emission spectrum of μV -regime biased Josephson elements, we gained substantial insight in their radiative behavior and interaction with the environment. Our initial investigation shows parasitic effects, such as self-induced Shapiro steps and down-converted emission features, which disappeared after changing the device designs and junction material. The observation of higher-order emission bands in junctions with modest critical currents implies a great sensitivity of our method. Various different material systems with potential for topological surface states haven been measured, for which $1e$ radiation is predicted. However, no such feature has been observed so far. About the reason we can only speculate. In the case of the Cd_3As_2 junction a possible explanation is the presence of a high concentration of surface states that drastically suppress the transmission probability and one could raise the same argument for the HgTe and WTe_2 . However, there can be other explanations. There can be some unaccounted factors in the measurements that prevent the observation of $1e$ emission or maybe the problem has a more involved cause. Since the topological states can be elusive and are easily mimicked by other phenomena, a combination of techniques should be used on a single sample to be able to obtain a solid proof of topological states. It is therefore possible that real topological materials are even less common than we believe they are from other experimental methods. The answers to these

questions are beyond the scope of this thesis but gives a strong motivation to perform additional experiments.

7 Conclusion and Outlook

This work was inspired by two fascinating, although very distinct physical phenomena: the rather exotic Josephson physics that appear when two superconductors are weakly linked, and the versatility and probing power of microwaves that are omnipresent in our everyday life. Their combination sent us on a scientific journey, in which we use microwaves of varying frequency and power to explore the fundamental properties of a wide arrange of different Josephson elements.

Our research can be categorized into two main experimental approaches: The first approach makes use of a highly sensitive superconducting resonator operating at microwave frequencies to both probe and interact with a Josephson junction. Here, a gate-tunable graphene Josephson junction is embedded in a superconducting loop and forms a rf SQUID. The junction is placed in close proximity to the resonant structure – a NbTiN $\lambda/4$ -resonator – to obtain a finite inductive coupling. By applying magnetic flux through the rf SQUID loop, the elementary phase across the junction can be adjusted over its full range, allowing us to characterise its changing electrical properties. Due to the inductive interaction, the Josephson element has become part of the resonant circuit, which allows us to trace its changing properties by ‘simply looking’ at the resonator characteristics. Interaction implies a two-way exchange of information and indeed, the oscillating stray field of the resonator creates a back-action on the Josephson junction. In our case, this stray microwave photon-field acts mainly on phase-dependent quasiparticle states living in the junction, the famous Andreev bound states (ABS).

By virtue of a concise circuit model in combination with an iterative fitting procedure, we translate the resonator response to the CPR, corrected for screening and the phase-dependent dissipation. Theoretical predictions, which take into account this microwave interaction between the resonator and the ABS spectrum, reveal a striking agreement for a short, diffusive junction model from which an ABS lifetime of ~ 17 ps was deduced.

The second experiment requires a less complicated device design. It mainly contains a voltage biased Josephson element and directly makes use of the conversion from a dc voltage to an oscillating supercurrent, as dictated by the ac Josephson relation. These oscillations are small but can be probed when the Josephson element is sufficiently coupled via a low-noise high-gain amplifica-

tion chain to a spectrum analyzer, essentially ‘listening’ to the junction. The operational bandwidth of our set-up lays in the microwave regime and hence requires a stable μV -voltage bias, ensured by shunting the junction with a resistor. In general, voltage biased Josephson elements simultaneously emit at different well-defined frequencies, where the respective amplitudes can be directly related to the Fourier amplitudes of the current-phase relation.

By directly measuring the emission spectrum of different types of Josephson junctions we have obtained a zoo of observations: (i) clear signatures of trivial $2e$ emission have been detected on all different flavors of junctions (SIS, SNS, 1D and 2/3D), (ii) we have found features attributed to a down-conversion of the emission on junctions with non-ideal lead designs, which also result in self-induced Shapiro steps, and more impressively (iii) we detected the emission traces of higher-order tunneling events, attributed to $4e$ and even $6e$ radiation which indicates, beside large junction transparencies, also a high measurement sensitivity.

The fact that both of these measurement techniques are now well established and there exist plentiful ideas for device and set-up optimisations, a unique and highly versatile platform for future experiments is provided. The obvious next step for the rf SQUID technique would be to incorporate a potentially topological material, investigate whether the topological nature can be observed in the dissipation feature, and most importantly, whether it poses a clear distinction from the trivial case. We should stress that the graphene junction investigated here could serve as benchmark for the trivial case. Because of the extremely small gap at the π -point the spectrum has a very similar shape as the one expected for Majoranas, but without the essential parity protection.

On the side of the radiation measurements, the first steps that should be taken in the near future should rather focus on further improving the set-up. An essential part is to solve the problem with excessive noise when performing measurements in magnetic fields. Furthermore, the incorporation of a tunable resonator would be applicable without large modifications to the devices or setup. An experiment on the further horizon could even combine these two techniques. For instance, the radiative signal from a Al SIS tunnel junction can have energies up to the gap edge (~ 44 GHz), which can be utilized to perform two-tone spectroscopy over very large frequency ranges on the ABS or MBS spectrum of a second more exotic junction. An even more elaborate measurement scheme could exploit the emitter/detector dualism of a JJ and so that it could be used as an on-chip VNA. Not only would both the source and detection take place at milliKelvin temperatures which greatly reduces thermal fluctuations, there would also be an obvious and huge improvement in terms of scaling up. One would no longer require rf-components and advanced expensive electronics, and a full microwave characterisation could be performed using only dc infrastructure.

Bibliography

- [1] H. Kamerlingh Onnes, Leiden Communication **120b**, **122b** (1911).
- [2] J. Bardeen, L. N. Cooper, and J. R. Schrieffer, Theory of Superconductivity **105**, 1175 (1957).
- [3] M. Tinkham, *Introduction to superconductivity* (Courier Corporation, 2004).
- [4] T. T. Heikkilä, *The physics of nanoelectronics: transport and fluctuation phenomena at low temperatures*, Vol. 21 (Oxford University Press, 2013).
- [5] N. A. Court, A. J. Ferguson, and R. G. Clark, Superconductor Science and Technology **21**, 015013 (2008).
- [6] J. P. Turneaure and I. Weissman, Journal of Applied Physics **39**, 4417 (1968).
- [7] W. Meissner and R. Ochsenfeld, Die Naturwissenschaften **21**, 787 (1933).
- [8] R. Merservey, B. Schwartz, and R. Parks, Superconductivity **1**, 117 (1969).
- [9] V. Ginzburg, L. Landau, M. Leontovich, and V. Fok, JETP **20**, 1064 (1950).
- [10] A. Abrikosov, J. Exptl. Theoret. Phys.(USSR) **32**, 1442 (1957).
- [11] B. D. Josephson, Advances in Physics **14**, 419 (1965).
- [12] M. A. Castellanos-Beltran and K. W. Lehnert, Applied Physics Letters **91**, 83509 (2007).
- [13] C. Macklin, K. O'Brien, D. Hover, M. E. Schwartz, V. Bolkhovskiy, X. Zhang, W. D. Oliver, and I. Siddiqi, Science **350**, 307 (2015).
- [14] A. Grimm, F. Blanchet, R. Albert, J. Leppäkangas, S. Jebari, D. Hazra, F. Gustavo, J. L. Thomassin, E. Dupont-Ferrier, F. Portier, and M. Hofheinz, Physical Review X **9**, 021016 (2019).
- [15] M. C. Cassidy, A. Bruno, S. Rubbert, M. Irfan, J. Kammhuber, R. N. Schouten, A. R. Akhmerov, and L. P. Kouwenhoven, Science **355**, 939 (2017).
- [16] A. Wallraff, D. Schuster, A. Blais, L. Frunzio, R. Huang, J. Majer, S. Kumar, S. Girvin, and R. Schoelkopf, Nature **431**, 162 (2004).
- [17] J. Clarke and F. K. Wilhelm, Nature **453**, 1031 (2008).

- [18] F. Arute, K. Arya, R. Babbush, D. Bacon, J. C. Bardin, R. Barends, R. Biswas, S. Boixo, F. G. S. L. Brandao, D. A. Buell, B. Burkett, Y. Chen, Z. Chen, B. Chiaro, R. Collins, W. Courtney, A. Dunsworth, E. Farhi, B. Foxen, A. Fowler, C. Gidney, M. Giustina, R. Graff, K. Guerin, S. Habegger, M. P. Harrigan, M. J. Hartmann, A. Ho, M. Hoffmann, T. Huang, T. S. Humble, S. V. Isakov, E. Jeffrey, Z. Jiang, D. Kafri, K. Kechedzhi, J. Kelly, P. V. Klimov, S. Knysh, A. Korotkov, F. Kostritsa, D. Landhuis, M. Lindmark, E. Lucero, D. Lyakh, S. Mandrà, J. R. McClean, M. McEwen, A. Megrant, X. Mi, K. Michielsen, M. Mohseni, J. Mutus, O. Naaman, M. Neeley, C. Neill, M. Y. Niu, E. Ostby, A. Petukhov, J. C. Platt, C. Quintana, E. G. Rieffel, P. Roushan, N. C. Rubin, D. Sank, K. J. Satzinger, V. Smelyanskiy, K. J. Sung, M. D. Trevithick, A. Vainsencher, B. Villalonga, T. White, Z. J. Yao, P. Yeh, A. Zalcman, H. Neven, and J. M. Martinis, *Nature* **574**, 505 (2019).
- [19] A. Stockklauser, P. Scarlino, J. V. Koski, S. Gasparinetti, C. K. Andersen, C. Reichl, W. Wegscheider, T. Ihn, K. Ensslin, and A. Wallraff, *Physical Review X* **7**, 11030 (2017).
- [20] J. Kohlmann, R. Behr, and T. Funck, *Measurement Science and Technology* **14**, 1216 (2003).
- [21] D. Vasyukov, Y. Anahory, L. Embon, D. Halbertal, J. Cuppens, L. Neeman, A. Finkler, Y. Segev, Y. Myasoedov, M. L. Rappaport, M. E. Huber, and E. Zeldov, *Nature Nanotechnology* **8**, 639 (2013).
- [22] G.-H. Lee, D. K. Efetov, W. Jung, L. Ranzani, E. D. Walsh, T. A. Ohki, T. Taniguchi, K. Watanabe, P. Kim, D. Englund, and K. C. Fong, *Nature* **586**, 42 (2020).
- [23] R. Kokkonen, J.-P. Girard, D. Hazra, A. Laitinen, J. Govenius, R. E. Lake, I. Sallinen, V. Vesterinen, M. Partanen, J. Y. Tan, K. W. Chan, K. Y. Tan, P. Hakonen, and M. Möttönen, *Nature* **586**, 47 (2020).
- [24] Y.-J. Doh, J. A. Van Dam, A. L. Roest, E. P. A. M. Bakkers, L. P. Kouwenhoven, and S. De Franceschi, *Science* **309** (2005).
- [25] C. Janvier, L. Tosi, L. Bretheau, C. O. Girit, M. Stern, P. Bertet, P. Joyez, D. Vion, D. Esteve, M. F. Goffman, H. Pothier, and C. Urbina, *Science* **349**, 1199 (2015).
- [26] A. F. Andreev, *Soviet Physics JETP* **19**, 1228 (1964).
- [27] G. E. Blonder, M. Tinkham, and T. M. Klapwijk, *Physical Review B* **25**, 4515 (1982).
- [28] M. Kjaergaard, F. Nichele, H. J. Suominen, M. P. Nowak, M. Wimmer, A. R. Akhmerov, J. A. Folk, K. Flensberg, J. Shabani, C. J. Palmstrøm, and C. M. Marcus, *Nature Communications* **7**, 12841 (2016).
- [29] I. Kulik, *Soviet Journal of Experimental and Theoretical Physics* **30**, 944 (1969).
- [30] B. Pannetier and H. Courtois, *Journal of Low Temperature Physics* **118**, 599 (2000).

-
- [31] P. F. Bagwell, *Physical Review B* **46**, 12573 (1992).
- [32] B. Dassonneville, A. Murani, M. Ferrier, S. Guéron, and H. Bouchiat, *Physical Review B* **97**, 184505 (2018).
- [33] D. A. Ivanov, R. von Roten, and G. Blatter, *Physical Review B - Condensed Matter and Materials Physics* **66**, 1 (2002).
- [34] M. Hays, G. de Lange, K. Serniak, D. J. van Woerkom, D. Bouman, P. Krogstrup, J. Nygård, A. Geresdi, and M. H. Devoret, *Phys. Rev. Lett.* **121**, 47001 (2018).
- [35] L. Tosi, C. Metzger, M. F. Goffman, C. Urbina, H. Pothier, S. Park, A. L. Yeyati, J. Nygård, and P. Krogstrup, *Physical Review X* **9** (2019), 10.1103/PhysRevX.9.011010.
- [36] M. Hays, V. Fatemi, K. Serniak, D. Bouman, S. Diamond, G. de Lange, P. Krogstrup, J. Nygård, A. Geresdi, and M. H. Devoret, *Nature Physics* **16**, 1103 (2020).
- [37] C. Beenakker, *Physical review letters* **67**, 3836 (1991).
- [38] V. Ambegaokar and A. Baratoff, *Physical Review Letters* **10**, 486 (1963).
- [39] Y. V. Nazarov, *Physical Review Letters* **73**, 134 (1994).
- [40] C. W. J. Beenakker, *Reviews of Modern Physics* **69**, 731 (1997).
- [41] F. Kos, S. E. Nigg, and L. I. Glazman, *Physical Review B - Condensed Matter and Materials Physics* **87**, 174521 (2013).
- [42] O. N. Dorokhov, *Solid State Communications* **51**, 381 (1984).
- [43] T. T. Heikkilä and F. Giazotto, 10.1103/PhysRevB.79.094514.
- [44] I. Kulik and A. Omel'Yanchuk, *Soviet Journal of Experimental and Theoretical Physics Letters* **21**, 96 (1975).
- [45] F. Vischi, M. Carrega, A. Braggio, P. Virtanen, and F. Giazotto, *Entropy* **21**, 1005 (2019).
- [46] C. Beenakker and C. Schönberger, *Physics Today* **56**, 37 (2003).
- [47] A. Paila, D. Gunnarsson, J. Sarkar, M. A. Sillanpää, and P. J. Hakonen, *Physical Review B* **80**, 144520 (2009).
- [48] W. C. Stewart, *Applied Physics Letters* **12**, 277 (1968).
- [49] V. Ambegaokar and B. I. Halperin, *Physical Review Letters* **22**, 1364 (1969).
- [50] S. Shapiro, *Physical Review Letters* **11**, 80 (1963).
- [51] J. Ridderbos, M. Brauns, A. Li, E. P. Bakkers, A. Brinkman, W. G. Van Der Wiel, and F. A. Zwanenburg, *Physical Review Materials* **3** (2019), 10.1103/PhysRevMaterials.3.084803.

- [52] R. Gross, A. Marx, and F. Deppe, *Applied superconductivity: Josephson effect and superconducting electronics* (De Gruyter, 2016).
- [53] F. Müller, R. Pöpel, J. Kohlmann, J. Niemeyer, W. Meier, T. Weimann, L. Grimm, F. W. Dünschede, and P. Gutmann, *IEEE Transactions on Instrumentation and Measurement* **46**, 229 (1997).
- [54] E. M. Spanton, M. Deng, S. Vaitiekėnas, P. Krogstrup, J. Nygård, C. M. Marcus, and K. A. Moler, *Nature Physics* **13**, 1177 (2017).
- [55] A. H. Dayem and C. C. Grimes, *Applied Physics Letters* **9**, 47 (1966).
- [56] N. F. Pedersen, O. H. Soerensen, J. Mygind, P. E. Lindelof, M. T. Levinsen, and T. D. Clark, *Applied Physics Letters* **28**, 562 (1976).
- [57] R. S. Deacon, J. Wiedenmann, E. Bocquillon, F. Domínguez, T. M. Klapwijk, P. Leubner, C. Brüne, E. M. Hankiewicz, S. Tarucha, K. Ishibashi, H. Bühmann, and L. W. Molenkamp, *Physical Review X* **7**, 021011 (2017).
- [58] H. Kamata, R. S. Deacon, S. Matsuo, K. Li, S. Jeppesen, L. Samuelson, H. Q. Xu, K. Ishibashi, and S. Tarucha, *Physical Review B* **98** (2018), 10.1103/PhysRevB.98.041302.
- [59] M. Hofheinz, F. Portier, Q. Baudouin, P. Joyez, D. Vion, P. Bertet, P. Roche, and D. Esteve, *Physical Review Letters* **106**, 217005 (2011).
- [60] B. S. Deaver and W. M. Fairbank, *Physical Review Letters* **7**, 43 (1961).
- [61] R. Doll and M. Näbauer, *Physical Review Letters* **7**, 51 (1961).
- [62] J. B. Majer, J. R. Butcher, and J. E. Mooij, *Applied Physics Letters* **80**, 3638 (2002).
- [63] M. Tinkham, *Introduction to superconductivity* (Courier Corporation, 2004).
- [64] S. N. Erné, H. D. Hahlbohm, and H. Lübbig, *Journal of Applied Physics* **47**, 5440 (1976).
- [65] J. E. Mooij, T. P. Orlando, L. Levitov, L. Tian, C. H. Van Der Wal, and S. Lloyd, *Science* **285**, 1036 (1999).
- [66] J. Bylander, S. Gustavsson, F. Yan, F. Yoshihara, K. Harrabi, G. Fitch, D. G. Cory, Y. Nakamura, J.-S. Tsai, and W. D. Oliver, *Nature Physics* **7**, 565 (2011).
- [67] M. Stern, G. Catelani, Y. Kubo, C. Grezes, A. Bienfait, D. Vion, D. Esteve, and P. Bertet, *Physical Review Letters* **113** (2014), 10.1103/PhysRevLett.113.123601.
- [68] A. Zazunov, V. S. Shumeiko, E. N. Bratus', J. Lantz, and G. Wendin, *Physical Review Letters* **90**, 4 (2003).
- [69] C. Janvier, L. Tosi, L. Bretheau, Ç. Ö. Girit, M. Stern, P. Bertet, P. Joyez, D. Vion, D. Esteve, M. F. Goffman, H. Pothier, and C. Urbina, *Science* **349**, 1199 (2015).

- [70] A. Y. Kitaev, *Physics-Uspekhi* **44**, 131 (2001).
- [71] L. Fu and C. L. Kane, *Physical Review Letters* **100** (2008), 10.1103/PhysRevLett.100.096407.
- [72] D. Aasen, M. Hell, R. V. Mishmash, A. Higginbotham, J. Danon, M. Leijnse, T. S. Jespersen, J. A. Folk, C. M. Marcus, K. Flensberg, and J. Alicea, *Physical Review X* **6**, 1 (2016).
- [73] D. M. Badiane, L. I. Glazman, M. Houzet, and J. S. Meyer, *Comptes Rendus Physique* **14**, 840 (2013).
- [74] Y. Peng, F. Pientka, E. Berg, Y. Oreg, and F. von Oppen, *Physical Review B* **94**, 085409 (2016).
- [75] M. C. Dartiailh, J. J. Cuozzo, B. H. Elfeky, W. Mayer, J. Yuan, K. S. Wickramasinghe, E. Rossi, and J. Shabani, *Nature Communications* **12**, 78 (2021).
- [76] F. Domínguez, F. Hassler, and G. Platero, *Physical Review B - Condensed Matter and Materials Physics* **86**, 140503 (2012).
- [77] F. Domínguez, O. Kashuba, E. Bocquillon, J. Wiedenmann, R. S. Deacon, T. M. Klapwijk, G. Platero, L. W. Molenkamp, B. Trauzettel, and E. M. Hankiewicz, *Physical Review B* **95**, 195430 (2017).
- [78] L. P. Rokhinson, X. Liu, and J. K. Furdyna, *Nature Physics* **8**, 795 (2012).
- [79] A. Q. Wang, C. Z. Li, C. Li, Z. M. Liao, A. Brinkman, and D. P. Yu, *Physical Review Letters* **121**, 237701 (2018).
- [80] K. Le Calvez, L. Veyrat, F. Gay, P. Plaidoux, C. B. Winkelmann, H. Courtois, and B. Sacépé, *Communications Physics* **2**, 4 (2019).
- [81] J. Wiedenmann, E. Bocquillon, R. S. Deacon, S. Hartinger, T. Herrmann, T. M. Klapwijk, L. Maier, C. Ames, C. Brüne, K. Ishibashi, S. Tarucha, H. Buhmann, L. W. Molenkamp, O. Herrmann, T. M. Klapwijk, L. Maier, C. Ames, C. Brüne, C. Gould, A. Oiwa, K. Ishibashi, S. Tarucha, H. Buhmann, and L. W. Molenkamp, *Nature communications* **10**, 303 (2015).
- [82] E. Bocquillon, R. S. Deacon, J. Wiedenmann, P. Leubner, T. M. Klapwijk, C. Brüne, K. Ishibashi, H. Buhmann, and L. W. Molenkamp, *Nature Nanotechnology* **12**, 137 (2016).
- [83] M. Houzet, J. S. Meyer, D. M. Badiane, and L. I. Glazman, *Physical Review Letters* **111**, 046401 (2013).
- [84] Y. Jang and Y. J. Doh, *Journal of the Korean Physical Society* **78**, 58 (2021).
- [85] H.-J. Kwon, K. Sengupta, and V. M. Yakovenko, *Eur. Phys. J. B* **37**, 349 (2004).
- [86] D. I. Pikulin and Y. V. Nazarov, *Physical Review B - Condensed Matter and Materials Physics* **86**, 140504 (2012).

- [87] D. Laroche, D. Bouman, D. J. van Woerkom, A. Proutski, C. Murthy, D. I. Pikulin, C. Nayak, R. J. J. van Gulik, J. Nygård, P. Krogstrup, L. P. Kouwenhoven, and A. Geresdi, *Nature Communications* **10**, 245 (2019).
- [88] R. M. Lutchyn, J. D. Sau, and S. Das Sarma, *Physical Review Letters* **105**, 077001 (2010).
- [89] D. Averin and H. T. Imam, *Physical Review Letters* **76**, 3814 (1996).
- [90] O. Dmytruk, M. Trif, and P. Simon, *Physical Review B - Condensed Matter and Materials Physics* **94**, 115423 (2016).
- [91] M. Trif, O. Dmytruk, H. Bouchiat, R. Aguado, and P. Simon, *Physical Review B* **97** (2018), 10.1103/PhysRevB.97.041415.
- [92] A. Murani, B. Dassonneville, A. Kasumov, J. Basset, M. Ferrier, R. Deblock, S. Guéron, and H. Bouchiat, *Physical Review Letters* **122** (2019), 10.1103/PhysRevLett.122.076802.
- [93] G. J. Dolan, *Applied Physics Letters* **31**, 337 (1977).
- [94] I. M. Pop, T. Fournier, T. Crozes, F. Lecocq, I. Matei, B. Pannetier, O. Buisson, and W. Guichard, *Journal of Vacuum Science & Technology B, Nanotechnology and Microelectronics: Materials, Processing, Measurement, and Phenomena* **30**, 010607 (2012).
- [95] M. Jung, K. Yoshida, K. Park, X. X. Zhang, C. Yesilyurt, Z. B. Siu, M. B. Jalil, J. Park, J. Park, N. Nagaosa, J. Seo, and K. Hirakawa, *Nano Letters* **18**, 1863 (2018).
- [96] S. Hollosy, *Locally tunable InAs nanowire quantum dots for cooper pair splitting*, Ph.D. thesis, University of Basel (2014).
- [97] G. Fábíán, *Engineered magnetoconductance in InAs nanowire quantum dots*, Ph.D. thesis, University of Basel (2015).
- [98] J. Gramich, *Andreev and spin transport in carbon nanotube quantum dot hybrid devices*, Ph.D. thesis, University of Basel (2016).
- [99] V. Ranjan, *Admittance and noise detection in mesoscopic systems via GHz impedance matching*, Ph.D. thesis, University of Basel (2017).
- [100] P. Krogstrup, N. L. B. Ziino, W. Chang, S. M. Albrecht, M. H. Madsen, E. Johnson, J. Nygård, C. M. Marcus, and T. S. Jespersen, *Nature Materials* **14**, 400 (2015).
- [101] M. Hays, G. de Lange, K. Serniak, D. J. van Woerkom, D. Bouman, P. Krogstrup, J. Nygård, A. Geresdi, and M. H. Devoret, *Physical Review Letters* **121**, 047001 (2018).
- [102] C. H. Jünger, *Transport spectroscopy of semiconductor superconductor nanowire hybrid devices*, Ph.D. thesis, University of Basel (2019).

-
- [103] P. J. Zomer, M. H. D. Guimaraes, J. C. Brant, N. Tombros, and B. J. Van Wees, *Applied Physics Letters* **105**, 1 (2014).
- [104] D. I. Indolese, P. Karnatak, A. Kononov, R. Delagrangé, R. Haller, L. Wang, P. Makk, K. Watanabe, T. Taniguchi, and C. Schönenberger, arXiv (2020).
- [105] D. Chen, A. Kovach, X. Shen, S. Poust, and A. M. Armani, *ACS Photonics* **4**, 2376 (2017).
- [106] L. Wang, I. Meric, P. Y. Huang, Q. Gao, Y. Gao, H. Tran, T. Taniguchi, K. Watanabe, L. M. Campos, D. A. Muller, J. Guo, P. Kim, J. Hone, K. L. Shepard, and C. R. Dean, *Science* **342**, 614 (2013).
- [107] R. Kraft, J. Mohrmann, R. Du, P. B. Selvasundaram, M. Irfan, U. N. Kanilmaz, F. Wu, D. Beckmann, H. Von Löhneysen, R. Krupke, A. Akhmerov, I. Gornyi, and R. Danneau, *Nature Communications* **9**, 1 (2018).
- [108] C. Janvier, *Coherent manipulation of Andreev Bound States in an atomic contact*, Ph.D. thesis, Université Paris-Saclay (2016).
- [109] E. U. Manual, Inc., Liverpool, NY, 50 (2005).
- [110] J. Hu, M. Salatino, A. Traini, C. Chaumont, F. Boussaha, C. Goupil, and M. Piat, *Journal of Low Temperature Physics* **199**, 355 (2020).
- [111] T. Hasler, *Microwave noise detection of a quantum dot with stub impedance matching*, Ph.D. thesis, University of Basel (2016).
- [112] A. Roy and M. Devoret, “Introduction to parametric amplification of quantum signals with Josephson circuits,” (2016).
- [113] T. C. White, J. Y. Mutus, I. C. Hoi, R. Barends, B. Campbell, Y. Chen, Z. Chen, B. Chiaro, A. Dunsworth, E. Jeffrey, J. Kelly, A. Megrant, C. Neill, P. J. O’Malley, P. Roushan, D. Sank, A. Vainsencher, J. Wenner, S. Chaudhuri, J. Gao, and J. M. Martinis, *Applied Physics Letters* **106**, 242601 (2015).
- [114] J. Basset, M. Kuzmanović, P. Virtanen, T. T. Heikkilä, J. Estève, J. Gabelli, C. Strunk, and M. Aprili, “Nonadiabatic Dynamics of Strongly Driven Diffusive Josephson Junctions,” (2019).
- [115] J. Burnett, A. Bengtsson, D. Niepce, and J. Bylander, *Journal of Physics: Conference Series* **969**, 012131 (2018).
- [116] A. A. Golubov, M. Y. Kupriyanov, and E. Il’ichev, *Reviews of Modern Physics* **76**, 411 (2004).
- [117] P. Virtanen, F. S. Bergeret, J. C. Cuevas, and T. T. Heikkilä, *Physical Review B - Condensed Matter and Materials Physics* **83**, 144514 (2011).
- [118] R. Aguado, *Applied Physics Letters* **117**, 240501 (2020).
- [119] A. H. Silver and J. E. Zimmerman, *Physical Review* **157**, 317 (1967).

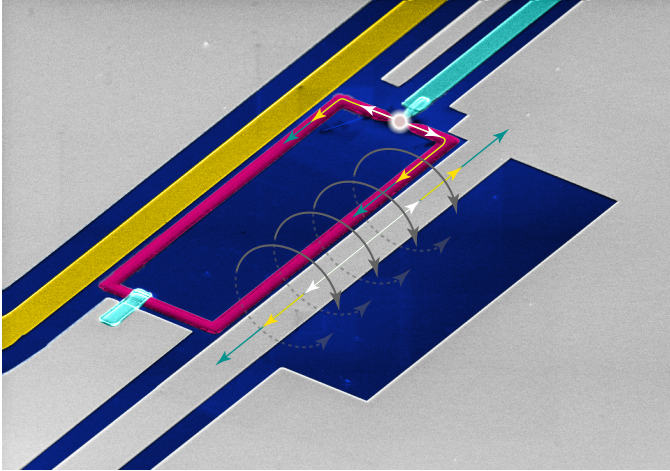
- [120] Z. Dou, T. Wakamura, P. Virtanen, N.-J. Wu, R. Deblock, S. Autier-Laurent, K. Watanabe, T. Taniguchi, S. Guéron, H. Bouchiat, *et al.*, arXiv preprint arXiv:2011.07308 (2020).
- [121] F. Zhou, P. Charlat, B. Spivak, and B. Pannetier, *Journal of Low Temperature Physics* **110**, 841 (1998).
- [122] F. Chiodi, M. Ferrier, K. Tikhonov, P. Virtanen, T. T. Heikkilä, M. Feigelman, S. Guéron, and H. Bouchiat, *Scientific Reports* **1**, 1 (2011).
- [123] M. Ferrier, B. Dassonneville, S. Guéron, and H. Bouchiat, *Physical Review B - Condensed Matter and Materials Physics* **88**, 174505 (2013).
- [124] B. Dassonneville, M. Ferrier, S. Guéron, and H. Bouchiat, *Physical Review Letters* **110**, 217001 (2013).
- [125] R. E. Lake, J. Govenius, R. Kokkonen, K. Y. Tan, M. Partanen, P. Virtanen, and M. Möttönen, *Advanced Electronic Materials* **3**, 1600227 (2017).
- [126] P. F. Bagwell, *Physical Review B* **46**, 12573 (1992).
- [127] D. Averin and H. T. Imam, *Physical Review Letters* **76**, 3814 (1996).
- [128] A. Martín-Rodero, A. L. Yeyati, and F. García-Vidal, *Physical Review B - Condensed Matter and Materials Physics* **53**, R8891 (1996).
- [129] J. G. Kroll, W. Uilhoorn, K. L. van der Enden, D. de Jong, K. Watanabe, T. Taniguchi, S. Goswami, M. C. Cassidy, and L. P. Kouwenhoven, *Nature Communications* **9**, 4615 (2018).
- [130] Z. Wang, B. J. Wieder, J. Li, B. Yan, and B. A. Bernevig, *Physical Review Letters* **123**, 1 (2019).
- [131] F. E. Schmidt, M. D. Jenkins, K. Watanabe, T. Taniguchi, and G. A. Steele, *Nature Communications* **9**, 4069 (2018).
- [132] M. S. Khalil, M. J. A. Stoutimore, F. C. Wellstood, and K. D. Osborn, *Journal of Applied Physics* **111**, 054510 (2011).
- [133] M. Göppl, A. Fragner, M. Baur, R. Bianchetti, S. Filipp, J. M. Fink, P. J. Leek, G. Puebla, L. Steffen, and A. Wallraff, *Journal of Applied Physics* **104**, 113904 (2008).
- [134] F. E. Terman, *Electronic and radio engineering* (McGraw-Hill, 1955).
- [135] S. Gevorgian, *Electronics Letters* **30**, 1236 (1994).
- [136] C. D. English, D. R. Hamilton, C. Chialvo, I. C. Moraru, N. Mason, and D. J. Van Harlingen, *Physical Review B* **94**, 1 (2016).
- [137] G. Nanda, J. L. Aguilera-Servin, P. Rakyta, A. Kormányos, R. Kleiner, D. Koelle, K. Watanabe, T. Taniguchi, L. M. Vandersypen, and S. Goswami, *Nano Letters* **17**, 3396 (2017).

- [138] D. A. Manjarrés, S. Gómez Paéz, and W. J. Herrera, *Physical Review B* **101**, 64503 (2020).
- [139] F. Nichele, E. Portolés, A. Fornieri, A. M. Whiticar, A. C. Drachmann, S. Gronin, T. Wang, G. C. Gardner, C. Thomas, A. T. Hatke, M. J. Manfra, and C. M. Marcus, *Physical Review Letters* **124** (2020), 10.1103/PhysRevLett.124.226801.
- [140] I. V. Borzenets, F. Amet, C. T. Ke, A. W. Draelos, M. T. Wei, A. Seredinski, K. Watanabe, T. Taniguchi, Y. Bomze, M. Yamamoto, S. Tarucha, and G. Finkelstein, *Physical Review Letters* **117**, 1 (2016).
- [141] J. Xue, J. Sanchez-Yamagishi, D. Bulmash, P. Jacquod, A. Deshpande, K. Watanabe, T. Taniguchi, P. Jarillo-Herrero, and B. J. LeRoy, *Nature Materials* **10**, 282 (2011).
- [142] J. D. Pillet, C. H. Quay, P. Morfin, C. Bena, A. L. Yeyati, and P. Joyez, *Nature Physics* **6**, 965 (2010).
- [143] L. Bretheau, J. I.-J. Wang, R. Pisoni, K. Watanabe, T. Taniguchi, and P. Jarillo-Herrero, *Nature Physics* **13**, 756 (2017).
- [144] J. G. Hoffman, *Physics Today* **15**, 30 (1962).
- [145] C. Li, S. Guéron, A. Chepelianskii, and H. Bouchiat, *Physical Review B* **94**, 1 (2016).
- [146] J. Voutilainen, A. Fay, P. Häkkinen, J. K. Viljas, T. T. Heikkilä, and P. J. Hakonen, *Physical Review B - Condensed Matter and Materials Physics* **84**, 45419 (2011).
- [147] D. K. Efetov, R.-J. Shiue, Y. Gao, B. Skinner, E. D. Walsh, H. Choi, J. Zheng, C. Tan, G. Grosso, C. Peng, J. Hone, K. C. Fong, and D. Englund, *Nature Nanotechnology* **13**, 797 (2018).
- [148] C. Nayak, S. H. Simon, A. Stern, M. Freedman, and S. Das Sarma, *Reviews of Modern Physics* **80**, 1083 (2008).
- [149] T. Karzig, C. Knapp, R. M. Lutchyn, P. Bonderson, M. B. Hastings, C. Nayak, J. Alicea, K. Flensberg, S. Plugge, Y. Oreg, C. M. Marcus, and M. H. Freedman, *Physical Review B* **95**, 235305 (2017).
- [150] L. Fu and C. L. Kane, *Physical Review B - Condensed Matter and Materials Physics* **79** (2009), 10.1103/PhysRevB.79.161408.
- [151] P. San-Jose, E. Prada, and R. Aguado, *Physical Review Letters* **108**, 257001 (2012).
- [152] S. Jeon, B. B. Zhou, A. Gyenis, B. E. Feldman, I. Kimchi, A. C. Potter, Q. D. Gibson, R. J. Cava, A. Vishwanath, and A. Yazdani, *Nature Materials* **13**, 851 (2014).
- [153] A. Q. Wang, C. Z. Li, C. Li, Z. M. Liao, A. Brinkman, and D. P. Yu, *Physical Review Letters* **121**, 237701 (2018).

- [154] Y. Oreg, G. Refael, and F. Von Oppen, *Physical Review Letters* **105** (2010), 10.1103/PhysRevLett.105.177002.
- [155] C. Z. Li, C. Li, L. X. Wang, S. Wang, Z. M. Liao, A. Brinkman, and D. P. Yu, *Physical Review B* **97**, 115446 (2018).
- [156] C. Brüne, C. X. Liu, E. G. Novik, E. M. Hankiewicz, H. Buhmann, Y. L. Chen, X. L. Qi, Z. X. Shen, S. C. Zhang, and L. W. Molenkamp, *Physical Review Letters* **106** (2011), 10.1103/PhysRevLett.106.126803.
- [157] A. Kononov, G. Abulizi, K. Qu, J. Yan, D. Mandrus, K. Watanabe, T. Taniguchi, and C. Schönenberger, *Nano letters* **20**, 4228 (2020).
- [158] Z. Wang, B. J. Wieder, J. Li, B. Yan, and B. A. Bernevig, *Physical Review Letters* **123**, 186401 (2019).
- [159] Y.-B. Choi, Y. Xie, C.-Z. Chen, J. Park, S.-B. Song, J. Yoon, B. J. Kim, T. Taniguchi, K. Watanabe, J. Kim, K. C. Fong, M. N. Ali, K. T. Law, and G.-H. Lee, *Nature Materials* **19**, 974 (2020).
- [160] D. A. Kozlov, D. Bauer, J. Ziegler, R. Fischer, M. L. Savchenko, Z. D. Kvon, N. N. Mikhailov, S. A. Dvoretzky, and D. Weiss, *Physical Review Letters* **116** (2016), 10.1103/PhysRevLett.116.166802.
- [161] S. Vaitiekėnas, P. Krogstrup, and C. M. Marcus, *Physical Review B* **101**, 60507 (2020).
- [162] A. Kononov, M. Endres, G. Abulizi, K. Qu, J. Yan, D. G. Mandrus, K. Watanabe, T. Taniguchi, and C. Schönenberger, arXiv preprint arXiv:2007.04752 (2020).
- [163] H. Courtois, M. Meschke, J. T. Peltonen, and J. P. Pekola, *Physical Review Letters* **101**, 067002 (2008).
- [164] I. Sochnikov, L. Maier, C. A. Watson, J. R. Kirtley, C. Gould, G. Tkachov, E. M. Hankiewicz, C. Brüne, H. Buhmann, L. W. Molenkamp, and K. A. Moler, *Physical Review Letters* **114**, 066801 (2015).
- [165] A. Murani, A. Kasumov, S. Sengupta, Y. A. Kasumov, V. T. Volkov, I. I. Khodos, F. Brisset, R. Delagrangé, A. Chepelianskii, R. Deblock, H. Bouchiat, and S. Guéron, *Nature Communications* **8**, 1 (2017).
- [166] A. A. Soluyanov, D. Gresch, Z. Wang, Q. Wu, M. Troyer, X. Dai, and B. A. Bernevig, *Nature* **527**, 495 (2015).
- [167] O. O. Shvetsov, A. Kononov, A. V. Timonina, N. N. Kolesnikov, and E. V. Deviatov, *EPL (Europhysics Letters)* **124**, 47003 (2018).
- [168] D. M. Pozar, *Microwave engineering* (John Wiley & sons, 2011).
- [169] M. A. Castellanos-Beltrán, *Development of a Josephson Parametric Amplifier for the Preparation and Detection of Nonclassical States of Microwave Fields*, Ph.D. thesis, University of Colorado (2010).

- [170] J. Zmuidzinas, *Annual Review of Condensed Matter Physics* **3**, 169 (2012).
- [171] M. Göppl, A. Fragner, M. Baur, R. Bianchetti, S. Filipp, J. M. Fink, P. J. Leek, G. Puebla, L. Steffen, and A. Wallraff, *Journal of Applied Physics* **104**, (2008).
- [172] K. D. Usadel, *Physical Review Letters* **25**, 507 (1970).
- [173] J. Xia, F. Chen, J. Li, and N. Tao, *Nature Nanotechnology* **4**, 505 (2009).
- [174] A. Laturia, M. L. Van de Put, and W. G. Vandenberghe, *npj 2D Materials and Applications* **2**, 6 (2018).
- [175] M. T. Allen, O. Shtanko, I. C. Fulga, J. I. Wang, D. Nurgaliev, K. Watanabe, T. Taniguchi, A. R. Akhmerov, P. Jarillo-Herrero, L. S. Levitov, and A. Yacoby, *Nano Letters* **17**, 7380 (2017).
- [176] V. E. Calado, S. Goswami, G. Nanda, M. Diez, A. R. Akhmerov, K. Watanabe, T. Taniguchi, T. M. Klapwijk, and L. M. K. Vandersypen, *Nature Nanotechnology* **10**, 761 (2015).
- [177] A. F. Young and P. Kim, *Nature Physics* **5**, 222 (2009).

A Formal description of a $\lambda/4$ -resonator



In this chapter we derive the basics of a $\lambda/4$ -resonator in a loaded and unloaded configuration. We provide consistency proofs for the expressions relating the resonance frequency shift and the quality factor of the resonant circuit to properties of the inductively coupled load impedance – the rf SQUID. Furthermore, we describe a method to infer the characteristic impedance of the co-planer transmission line $\lambda/4$ -resonator from geometrical means and evaluate its equivalent lumped-element parallel RCL -circuit. Finally, the current distribution along the resonator is derived, which is an important quantity for estimating the induced phase oscillations in the inductively coupled rf SQUID. For this chapter we will closely Ref. [168].

A.1. Loaded $\lambda/4$ -resonator

The performance of a resonator is depending on the load impedance Z_{load} attached to it. In order to relate the resonance frequency f_0 and the quality factor Q of the resonator to properties of Z_{load} , one can compare the input impedance of the specific circuit with the one of a known circuit. Here, we will compare a loaded $\lambda/4$ -resonator with a parallel RLC -circuit.

Input impedance of a $\lambda/4$ -resonator

In the following we consider a $\lambda/4$ -resonator, in which the normally shorted end is replaced by a load impedance Z_{load} as shown in Fig. A.1.

In general, the input impedance of a transmission line (TL) of length l and characteristic impedance Z_r shunted by Z_{load} is given by

$$Z_{\text{in,TL}} = Z_r \frac{Z_{\text{load}} + Z_r \tanh(\gamma l)}{Z_r + Z_{\text{load}} \tanh(\gamma l)}. \quad (\text{A.1})$$

Since the complex propagation constant γ can be expressed as $\gamma = \alpha + j\beta$, where the real part α is the attenuation constant in TL and, the imaginary part β the wavenumber of the TL, we can rewrite

$$\tanh(\gamma l) = \frac{1 - j \tanh(\alpha l) \cot(\beta l)}{\tanh(\alpha l) - j \cot(\beta l)}. \quad (\text{A.2})$$

With $\beta = \omega/v_p$, where v_p is the phase velocity of the TL and by introducing the relative frequency $\delta\omega = \omega - \omega_0$ with respect to the resonance frequency ω_0 , the argument of the cot-term becomes

$$\beta l = \frac{\omega_0 l}{v_p} + \frac{\delta\omega l}{v_p}. \quad (\text{A.3})$$

The phase velocity at resonance for a quarterwave resonator ($\lambda = 4l$) reads $v_p = \lambda f_0 = 2l \frac{\omega_0}{\pi}$ and therefore

$$\beta l = \frac{\pi}{2} + \frac{\pi \delta\omega}{2\omega_0}. \quad (\text{A.4})$$

Assuming $\delta\omega$ being small, we can approximate

$$\cot(\beta l) = \cot\left(\frac{\pi}{2} + \frac{\pi \delta\omega}{2\omega_0}\right) = -\tan\left(\frac{\pi \delta\omega}{2\omega_0}\right) \approx -\frac{\pi \delta\omega}{2\omega_0}. \quad (\text{A.5})$$

Assuming that the $\lambda/4$ -resonator is lossless ($\alpha = 0$) we can simplify the input impedance to

$$Z_{\text{in}}^{\lambda/4} = Z_r \frac{Z_{\text{load}} - j Z_r \frac{2\omega_0}{\pi \delta\omega}}{Z_r - j Z_{\text{load}} \frac{2\omega_0}{\pi \delta\omega}}. \quad (\text{A.6})$$

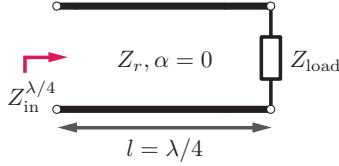


Figure A.1. Loaded quarterwave transmission line.

In the case of $Z_r \gg \frac{\pi\delta\omega}{2\omega_0} Z_{\text{load}}$, we can write

$$Z_{\text{in}}^{\lambda/4} = \frac{1}{\frac{Z_{\text{load}}}{Z_r^2} + j\frac{\pi\delta\omega}{2\omega_0 Z_r}}. \quad (\text{A.7})$$

In general the load impedance is complex valued and can be decomposed into its real and imaginary part, such that $Z_{\text{load}} = \text{Re}(Z_{\text{load}}) + j\text{Im}(Z_{\text{load}})$, which leads to

$$Z_{\text{in}}^{\lambda/4} = \frac{1}{\frac{\text{Re}(Z_{\text{load}})}{Z_r^2} + \frac{j}{Z_r} \left[\frac{\pi\delta\omega}{2\omega_0} + \frac{\text{Im}(Z_{\text{load}})}{Z_r} \right]}. \quad (\text{A.8})$$

Input impedance of parallel RLC -circuit

We compare this now to a parallel RLC resonant circuit shown in Fig. A.2. The input impedance of this circuit reads

$$Z_{\text{in}}^{RLC} = \left(\frac{1}{R_p} + \frac{1}{j\omega L_p} + j\omega C_p \right)^{-1} \quad (\text{A.9})$$

and its resonance frequency is $\omega_0 = 1/\sqrt{L_p C_p}$. Making again use of the relative frequency shift and analysing the circuit near resonance allows us to rewrite the former equation to

$$Z_{\text{in}}^{RLC} \approx \frac{1}{1/R_p + 2j\delta\omega C_p} \quad (\text{A.10})$$

or alternatively as

$$Z_{\text{in}}^{RLC} \approx \frac{1}{1/R_p + 2j\sqrt{\frac{C_p}{L_p}} \left(\frac{\delta\omega}{\omega_0} \right)} \quad (\text{A.11})$$

Additionally, the internal quality factor of the parallel resonant circuit can be expressed as

$$Q^{RLC} = \omega_0 R_p C_p. \quad (\text{A.12})$$

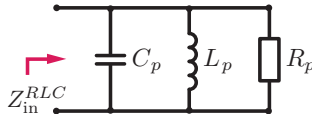


Figure A.2. Parallel RLC -circuit.

A.2. Influence of Z_{load} on f_0 and Q_{load}

The resonance condition for a loaded $\lambda/4$ -resonator is fulfilled, when $\text{Im}[Z_{\text{in}}^{\lambda/4}] = 0$, which leads to $\frac{\pi\delta\omega}{2\omega_0} + \frac{\text{Im}[Z_{\text{load}}]}{Z_r} = 0$ deduced from Eq. A.8. With the load – the new resonance frequency is called $\omega_0 (= 2\pi f_0)$, while the resonance frequency of the unloaded resonator is called $\omega_{\text{bare}} (= 2\pi f_{\text{bare}})$, hence $\delta\omega = \omega_0 - \omega_{\text{bare}}$. In the limit, $f_0 \approx f_{\text{bare}}$, we can express the resonance frequency shift influenced by the load impedance as

$$\delta f_0 = f_0 - f_{\text{bare}} = -\frac{2}{\pi Z_r} \text{Im}(Z_{\text{load}}) f_{\text{bare}}. \quad (\text{A.13})$$

In order to express the quality factor Q_{load} of a loaded quarterwave resonator, we assume that $\frac{\text{Im}[Z_{\text{load}}]}{Z_r} \ll 1$, such that we obtain from Eq. A.8

$$Z_{\text{in}}^{\lambda/4} \approx \frac{1}{\frac{\text{Re}(Z_{\text{load}})}{Z_r^2} + \frac{j}{Z_r} \left(\frac{\pi\delta\omega}{2\omega_0} \right)}. \quad (\text{A.14})$$

By comparing this expression with Eq. A.11, we can conclude that $R_p = \frac{Z_r^2}{\text{Re}(Z_{\text{load}})}$. Combining this finding with Eq. A.12 and Eq. A.25, we can express the load quality factor as

$$Q_{\text{load}} = \frac{\pi Z_r}{4 \text{Re}(Z_{\text{load}})}. \quad (\text{A.15})$$

A.2.1. Inductively coupled load

The load impedance in our circuit, as shown in Fig. A.3, can be found by applying the transformer equations and reads

$$Z_{\text{load}} = \frac{\omega^2 M^2}{j\omega L_{\text{loop}} + \left(\frac{1}{R_s} + \frac{1}{j\omega L_J} \right)^{-1}}, \quad (\text{A.16})$$

where ω describes the operating frequency. With this load impedance, we obtain for the quality factor

$$Q_{\text{load}} = \frac{\pi}{4} \cdot \frac{Z_r}{R_s M^2} \left[L_{\text{loop}}^2 + \frac{(L_J + L_{\text{loop}})^2 R_s^2}{\omega^2 L_J^2} \right]. \quad (\text{A.17})$$

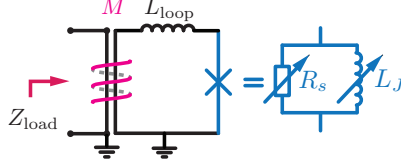


Figure A.3. Circuit schematic of the inductively coupled rf SQUID, in which the Josephson junction is modelled as variable Josephson inductance L_J in parallel with a variable shunt resistance R_s . The inductance of the superconducting loop is described by L_{loop} and the mutual inductance M quantifies the coupling strength between the end of the $\lambda/4$ -resonator and the rf SQUID.

Hence, we found a formalism to convert the load quality factor into an effective resistor shunting the JJ. In the case of $L_J \gg L_{\text{loop}}$ and $\frac{R_s}{\omega L_{\text{loop}}} \gg 1$, we can make the approximation:

$$Q_{\text{load}} \approx \frac{\pi}{4} \cdot \frac{Z_r}{\omega^2 M^2} \cdot R_s. \quad (\text{A.18})$$

Assuming $R_s \rightarrow \infty$ in Eq. A.16 and making use of Eq. A.26, we can approximate Eq. A.13 as

$$\delta f_0 \approx \frac{8}{\pi^2} \frac{M^2}{L_p(L_J + L_{\text{loop}})} f_{\text{bare}}, \quad (\text{A.19})$$

which describes the frequency shift as a function of the Josephson inductance L_J , which, in turn, is directly related to the current-phase relation (CPR).

A.2.2. Consistency proof for analytical expressions

Here, we prove the validity of the analytic formulas for δf_0 and Q_{load} (Eq. A.19 and Eq. A.17) by comparing their solutions with the numerically evaluated full model. In particular, we generate reflection curve maps and extract from those, the resonance frequency f_0^{full} and the load quality factor $Q_{\text{load}}^{\text{full}}$ by fitting as explained in Ch. B.1. In general, the reflection coefficient reads

$$\Gamma = \frac{Z_{\text{in}}^{\text{full}} - Z_0}{Z_{\text{in}}^{\text{full}} + Z_0}, \quad (\text{A.20})$$

where $Z_0 = 50 \Omega$ is the environmental impedance. The coupling capacitance C_c between the measurement set-up and the TL leads to an impedance $Z_c = 1/(j2\pi f C_c)$ in series with the input impedance of the loaded TL, $Z_{\text{in,TL}}$,

$$Z_{\text{in}}^{\text{full}} = Z_c + Z_{\text{in,TL}}. \quad (\text{A.21})$$

Hence, by combining Eq. A.1 and Eq. A.16 in Eq. A.20 with the use of Eq. A.21, we can express Γ as a function of Z_{load} with properties of the TL.

Consistency proof for δf_0

First, we provide a consistency proof for the expression of the frequency shift. In Fig. A.4, we keep the shunt resistance $R_s = 100 \text{ M}\Omega$ constant and sweep the Josephson inductance L_J .

From the artificial Γ -maps shown in Fig. A.4(a)-(b) a clear change in f_0^{full} is observed as a function of L_J , while the lineshape is not affected. Details about the parameters used here are listed in the figure caption. In Fig. A.4(c) we overlay the fit results for resonance frequency f_0^{full} of the artificial data (blue circles) with the prediction from the analytic formalism (red, Eq. A.19).

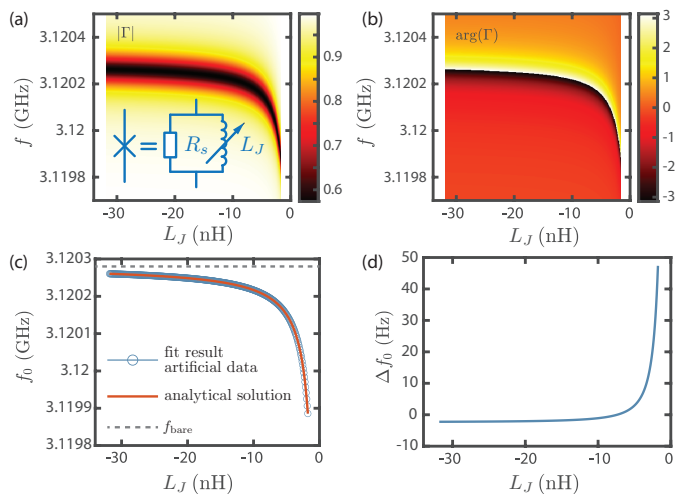


Figure A.4. Parameters for artificial data: $C_c = 4.6 \text{ fF}$, $\alpha = 0.001 \text{ m}^{-1}$, $\beta = 2\pi f \frac{\sqrt{\epsilon_{\text{eff}}}}{c}$, where $\epsilon_{\text{eff}} = 11.225$ and c is the speed of light, $l = 7.1 \text{ mm}$, $Z_r = 64.5 \text{ }\Omega$, $L_{\text{loop}} = 200 \text{ pH}$, $M = 32 \text{ pH}$, $R_s = 100 \text{ M}\Omega$, sinusoidal CPR $\rightarrow L_J = \frac{2\pi}{\Phi_0 I_c \cos(\varphi)}$, here the sweep range corresponds to the phase biasing condition $\varphi = \pi$ and the critical current is tuned $I_c = 10 \rightarrow 180 \text{ nA}$ (larger I_c produces more shift). (a)-(b) Colormaps of the artificial data $|\Gamma|$ and $\arg(\Gamma)$ as a function of Josephson inductance L_J . (c) The resonance frequency f_0^{full} (blue circles) obtained by fitting the artificial resonance curves. The analytically predicted resonance frequency (red lines) deduced from Eq. A.19 with the same parameters as listed above and $f_{\text{bare}} = 3.12028 \text{ GHz}$ obtained from minimizing $|\Gamma|$ for $L_J \rightarrow \infty$ in the full model. (d) Difference between f_0^{full} and the analytically obtained resonance frequency.

From Fig. A.4(d), which shows the difference Δf_0 between the resonance frequency of the artificial data and the one obtained from the analytic formalism, we observe only slight discrepancies on the order of Hz. Consequently, Eq. A.19 describes the resonance frequency as function of L_J to a very high accuracy.

Consistency proof for Q_{load}

Here, we provide a consistency proof for the expression of the load quality factor. In Fig. A.5, we keep the Josephson inductance $L_J = -3.2$ nH (sinusoidal CPR with $I_c = 100$ nA at $\varphi = \pi$) constant and sweep the shunt resistance R_s . For simplicity we set $\alpha = 0$, such that the effective quality factor is determined by the load.

From the artificial Γ -maps shown in Fig. A.5(a)-(b) a clear change in the lineshape of the resonance curve as a function of R_s is observed. Details about the parameters used here are listed in the figure caption.

The dark region in Fig. A.5(a), where $|\Gamma| = 0$ corresponds to full matching with $Q_c = Q_{\text{load}}$. The coupling quality factor can be expressed as [108, 169]

$$Q_c = \frac{\pi}{4\omega^2 Z_0 Z_r C_c^2}, \quad (\text{A.22})$$

for which we find $Q_c = 29950$ with the model parameters $C_c = 4.6$ fF, $Z_r = 64.5 \Omega$ and $\omega \approx 2\pi \cdot 3.12$ GHz. For small R_s values the resonator becomes overcoupled ($Q_c > Q_{\text{load}}$) and $\arg(\Gamma)$ evolves smoothly, whereas for large R_s values the resonator becomes undercoupled ($Q_c < Q_{\text{load}}$) and $\arg(\Gamma)$ undergoes a 2π -leap. In Fig. A.5(c) we overlay the fit results for Q_{load} of the artificial data (blue circles) and the prediction from the analytic formalism (red, Eq. A.17). From Fig. A.5(d), which presents the difference ΔQ_{load} between the artificial data and the predications, we observe very small discrepancies. Since, R_s is naturally present in $\text{Im}(Z_{\text{load}})$, changing the resistance causes in addition a small shift of the resonance frequency. By the comparison between the resonance frequency of the artificial data and the one obtained analytically (assumption $R_s \rightarrow \infty$, such that Eq. A.19 becomes valid) shown in Fig. A.5(e), we observe a discrepancy of ~ 6 kHz for the smallest R_s value. On a first glance this seems a lot, one should however relate this number with the overall shift of the resonance frequency coming from $L_J = -3.2$ nH, which is about 200 kHz. Hence, the error induced by neglecting R_s , is on the order of a few % as long as $R_s \geq 100 \Omega$, which is the case for our measurement.

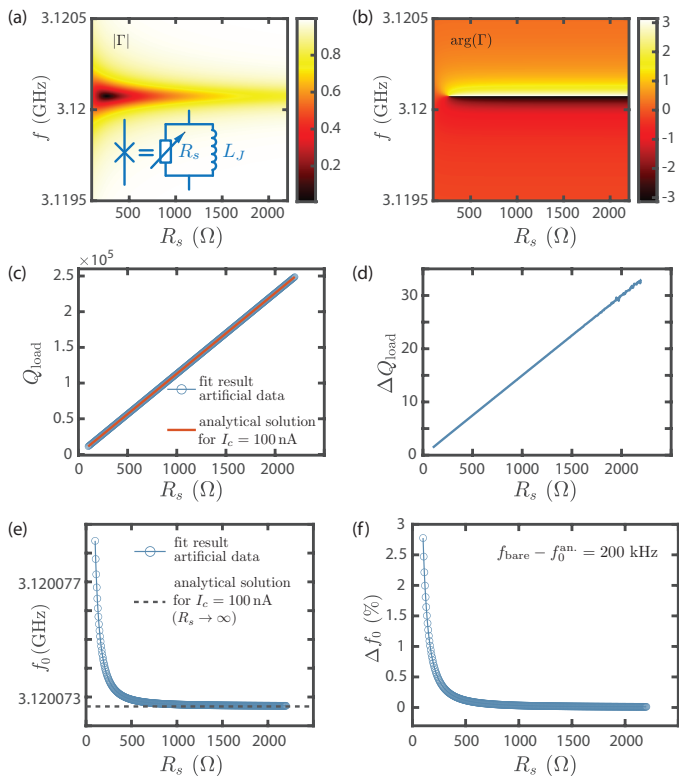


Figure A.5. Parameters for artificial data: $C_c = 4.6$ fF, $\alpha = 0$, $\beta = 2\pi f \frac{\sqrt{\epsilon_{\text{eff}}}}{c}$, where $\epsilon_{\text{eff}} = 11.225$ and c is the speed of light, $l = 7.1$ mm, $Z_r = 64.5$ Ω , $L_{\text{loop}} = 200$ pH, $M = 32$ pH, $I_c = 100$ nA, $L_J = -\Phi_0/(2\pi I_c) = -3.183$ nH. (a)-(b) Colormaps of the artificial data $|\Gamma|$ and $\arg(\Gamma)$ as a function of shunt resistance R_s . (c) The load quality factor Q_{load} (blue circles) obtained by fitting the artificial resonance curves as a function of R_s . The analytically predicted load quality factor (red lines) deduced from Eq. A.17 with the same parameters as listed above and $f_{\text{bare}} = 3.12028$ GHz obtained from minimizing $|\Gamma|$ for $L_J \rightarrow \infty$ and $R_s \rightarrow \infty$ in the full model. (d) Difference between $Q_{\text{load}}^{\text{full}}$ and the analytically obtained load quality factor. (e) The resonance frequency f_0^{full} (blue circles) obtained by fitting the artificial resonance curves and predicted resonance frequency for $L_J = -3.2$ nH. (f) Relative error between the actual resonance frequency shift and the predicted resonance frequency shift $f_0^{\text{an.}}$; $\Delta f_0(\%) = (f_0^{\text{full}} - f_0^{\text{an.}})/(f_{\text{bare}} - f_0^{\text{an.}})$.

A.3. Unloaded $\lambda/4$ -resonator

We can describe the special case of an unloaded quarterwave resonance circuit by evaluating Eq. A.7 for $Z_{\text{load}} = 0$:

$$Z_{\text{in}}^{\lambda/4} = \frac{1}{j \frac{\pi}{2Z_r} \left(\frac{\delta\omega}{\omega_0} \right)}. \quad (\text{A.23})$$

By directly comparing Eq. A.23 with Eq. A.11 for $R_p \rightarrow \infty$ one finds

$$\frac{\pi}{2Z_r} = 2\sqrt{\frac{C_p}{L_p}}. \quad (\text{A.24})$$

One can now determine the capacitance of the equivalent parallel RLC circuit with $\omega_0 = 1/\sqrt{L_p C_p}$ as

$$C_p = \frac{\pi}{4\omega_0 Z_r} \quad (\text{A.25})$$

and the inductance of the equivalent circuit as

$$L_p = \frac{4Z_r}{\pi\omega_0}. \quad (\text{A.26})$$

In a real experimental scenario the characteristic impedance Z_r is often not known precisely, since besides geometric ingredients – in particular, the capacitance per unit length C_r and the self-inductance per unit length \mathcal{L}_s – there is also a contribution from material properties, which gives rise to the kinetic inductance per unit length \mathcal{L}_k . Consequently, the characteristic impedance reads $Z_r = \sqrt{\mathcal{L}_r/C_r}$, where $\mathcal{L}_r = \mathcal{L}_s + \mathcal{L}_k$. Both C_r and \mathcal{L}_s can be computed with conformal mapping techniques to very high accuracy, whereas \mathcal{L}_k needs to be determined experimentally. \mathcal{L}_k can be measured in a temperature dependence or estimated via the low temperature normal sheet resistance [170]. In order to circumvent this inconvenience, we can make use of the wavelength λ , which in the case of a lossless transmission line is given by

$$\lambda = \frac{2\pi}{\beta} = \frac{2\pi}{\omega_0 \sqrt{\mathcal{L}_r C_r}}. \quad (\text{A.27})$$

By rearranging this expression at the quarterwave resonance condition and multiplying both sides with C_r , we find

$$\omega_0 C_r = \frac{2\pi}{4l \sqrt{\mathcal{L}_r C_r} \frac{1}{C_r}}. \quad (\text{A.28})$$

Substituting $Z_r = \sqrt{\mathcal{L}_r/C_r}$ into the previous equation and solve for Z_r leads to

$$Z_r = \frac{2\pi}{4l\omega_0 C_r}. \quad (\text{A.29})$$

This is now a description for Z_r by just geometrical means (l and C_r) in combination with the resonance frequency ω_0 . Here, we do assume an ideal resonator without any coupling to the environment – however those corrections will be small for large coupling quality factors Q_c . Now inserting Eq. A.29 into the expressions for the equivalent circuit (Eq. A.25 and A.26), we find in agreement with Ref. [171]

$$C_p = \frac{C_r l}{2}, \quad (\text{A.30})$$

$$L_p = \frac{2}{l\omega_0^2 C_r}. \quad (\text{A.31})$$

Evaluating Z_r and L_p

In order to evaluate characteristic properties of the resonant circuit, we make use of conformal mapping techniques derived in Ref. [135] to express the capacitance per unit length. The effective dielectric constant of a two-layered substrate is found to be

$$\widetilde{\epsilon}_{\text{eff}} = 1 + \frac{\epsilon_{r1} - \epsilon_{r2}}{2} \cdot \frac{K(k_1)K(k'_0)}{K(k'_1)K(k_0)} + \frac{\epsilon_{r2} - 1}{2} \cdot \frac{K(k_2)K(k'_0)}{K(k'_2)K(k_0)} \quad (\text{A.32})$$

and the corresponding capacitance per unit length reads

$$C_r = 4\epsilon_0 \widetilde{\epsilon}_{\text{eff}} \frac{K(k_0)}{K(k'_0)}. \quad (\text{A.33})$$

The functions K are the complete elliptical integrals of the first kind, in which

$$\begin{aligned} k_0 &= \frac{s}{s + 2w} \\ k_1 &= \frac{\sinh\left(\frac{\pi s}{4h_1}\right)}{\sinh\left(\frac{\pi(s+2w)}{4h_1}\right)} \\ k_2 &= \frac{\sinh\left(\frac{\pi s}{4(h_1+h_2)}\right)}{\sinh\left(\frac{\pi(s+2w)}{4(h_1+h_2)}\right)} \\ k'_i &= \sqrt{1 - k_i^2} \quad \text{with } i = 0, 1, 2, \end{aligned}$$

where s is the central conductor width, w is the spacing to the ground plane, h_1 is the thickness of the top dielectric with relative permittivity ϵ_{r1} and h_2 is the thickness of the bottom dielectric with relative permittivity ϵ_{r2} see Fig. A.6.

With $s = 12.1 \mu\text{m}$, $w = 6.1 \mu\text{m}$, SiO_2 thickness $h_1 = 170 \text{ nm}$, Si thickness $h_2 = 500 \mu\text{m}$, SiO_2 permittivity $\epsilon_{r1} = 3.9$, Si permittivity $\epsilon_{r2} = 11.8$ and the vacuum permittivity $\epsilon_0 = 8.854 \times 10^{-12} \text{ F/m}$ we find $C_r = 153.9 \text{ pF/m}$. With

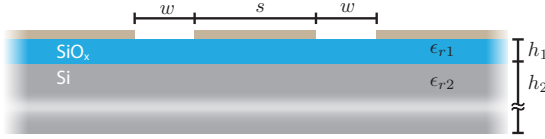


Figure A.6. Cross-section of a transmission line on a layered substrate.

this and the length of the TL $l = 7.54$ mm in combination with the resonance frequency $f_0 \approx 3.098029$ GHz we can now evaluate $Z_r = 69.54 \Omega$ with Eq. A.29, $C_p = 580$ fF with Eq. A.30 and $L_p = 4.548$ nH with Eq. A.31. Note that ϵ_{eff} describes purely the dielectric properties of the TL, whereas ϵ_{eff} also contains properties of the kinetic inductance.

A.4. Current within a $\lambda/4$ -resonator

In order to form a $\lambda/4$ -resonator the TL needs to be confined between two different ends. The so-called open end couples the TL via a coupling capacitance C_c to the measurement setup. Whereas the so-called shorted end terminates the TL via a load impedance Z_{load} to ground. Fig. A.7 shows a schematic of this circuit embedded in a measurement environment.

In an ideal $\lambda/4$ -resonator, where $C_c = 0$ and $Z_{\text{load}} = 0$, perfect reflection at both ports is provided. And one finds a current anti-node (node) and voltage node (anti-node) at the shorted (open) end. Thus, the first resonant mode has a wavelength $\lambda_0 = 4 \cdot l$, where l is the distance between the ports. With the phase velocity $v_p = \frac{c}{\sqrt{\epsilon_{\text{eff}}}}$ one can write the bare resonance frequency as

$$f_0 = \frac{c}{\lambda_0 \sqrt{\epsilon_{\text{eff}}}} = \frac{c}{4 \cdot l \cdot \sqrt{\epsilon_{\text{eff}}}}. \quad (\text{A.34})$$

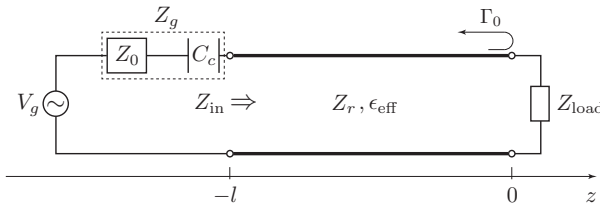


Figure A.7. Schematic of a loaded $\lambda/4$ -resonator with coupling capacitance C_c and load impedance Z_{load} connected to measurement set-up with impedance Z_0 .

In the non-ideal case ($C > 0$) the wave is leaking out through the open end, which results in a larger wavelength as compared to the ideal case and therefore the resonance frequency is slightly reduced.

Now we want to focus on the current amplitudes within a loaded $\lambda/4$ -resonator. Then we are interested in the magnetic field strength induced by the current within the resonator, since the resulting alternating magnetic field stimulates the nearby rf SQUID.

The total voltage and current waves on a terminated lossless transmission line can be written as

$$V(z) = V_0^+ [e^{-j\beta z} + \Gamma_0 e^{j\beta z}] \quad (\text{A.35a})$$

$$I(z) = \frac{V_0^+}{Z_r} [e^{-j\beta z} - \Gamma_0 e^{j\beta z}]. \quad (\text{A.35b})$$

Here Γ_0 is the reflection coefficient at the termination in a load impedance Z_{load} and reads:

$$\Gamma_0 = \frac{Z_{\text{load}} - Z_r}{Z_{\text{load}} + Z_r}. \quad (\text{A.36})$$

The input impedance looking from the coupling capacitance into the terminated TL is

$$Z_{\text{in}} = \frac{V(-l)}{I(-l)} = Z_r \frac{1 + \Gamma_0 e^{-2j\beta l}}{1 - \Gamma_0 e^{-2j\beta l}}. \quad (\text{A.37})$$

The voltage amplitude at this point can be expressed with the voltage division formula and reads with Eq. A.35a:

$$V(-l) = V_g \frac{Z_{\text{in}}}{Z_{\text{in}} + Z_g} = V_0^+ [e^{j\beta l} + \Gamma_0 e^{-j\beta l}]. \quad (\text{A.38})$$

Now one finds

$$V_0^+ = V_g \frac{Z_{\text{in}}}{Z_{\text{in}} + Z_g} \frac{1}{[e^{j\beta l} + \Gamma_0 e^{-j\beta l}]}. \quad (\text{A.39})$$

Here V_g is the peak generator voltage and Z_g is the generator impedance, which reads $Z_g = Z_0 + Z_c$. Here $Z_0 = 50 \Omega$ refers to the source's output impedance and $Z_c = 1/j2\pi f C_c$ corresponds to the coupling impedance. Finally, substituting Eq. A.39 into Eq. A.35b one finds an expression for the current amplitude distribution along the resonator:

$$I(z) = \frac{V_g}{Z_r} \frac{Z_{\text{in}}}{Z_{\text{in}} + Z_g} \frac{1}{[e^{j\beta l} + \Gamma_0 e^{-j\beta l}]} [e^{-j\beta z} - \Gamma_0 e^{j\beta z}]. \quad (\text{A.40})$$

With $Z_{\text{load}} = 0$ this simplifies to:

$$I_0(z) = \frac{V_g}{\sin(\beta l)} \frac{\tan(\beta l)}{j Z_r \tan(\beta l) + Z_g} \cos(\beta z). \quad (\text{A.41})$$

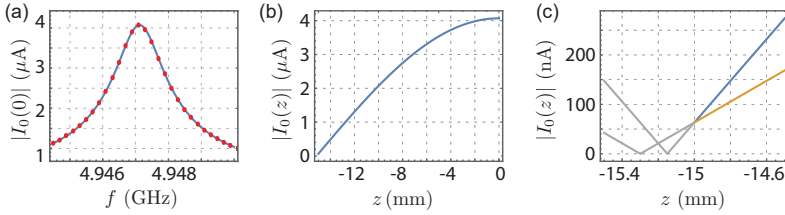


Figure A.8. (a) Blue line plots the absolute current $|I_0(0)|$ at the shorted end ($z = 0$) with $Z_{\text{load}} = 0$ as a function of frequency f provided by Eq. (A.41). The red points correspond to the results deduced from the circuit simulator. (b) Shows the current distribution along the TL Eq. (A.41) at the resonance frequency. (c) Shows the current distribution close to the capacitor for $C_c = 10$ fF (blue) and $C_c = 20$ fF (orange).

Now we compare the analytical result (visualized with Wolfram Mathematica 11.1.1) with the simulation result created within QUCS 0.0.19 (freeware). Note, the peak generator voltage V_g can be expressed as: $V_g = 10^{\frac{P[\text{dBm}]-10}{20}}$ [V], where the power at the sample reads $P = P_{\text{out}} - P_{\text{att}}$ with the VNA's output power P_{out} and attenuation $P_{\text{att}} \approx 70$ dBm. For the comparison following parameters were used: $P = -100$ dBm ($V_g = 3.16 \mu\text{V}$), $Z_0 = 50 \Omega$, $C_c = 10$ fF, $Z_r = 50 \Omega$, $\epsilon_{\text{eff}} = 1$, $l = 15$ mm and $Z_{\text{load}} = 0$. The blue curve in Fig. A.8(a) plots the absolute value of Eq. A.41 as a function of frequency f at the shorted end ($z = 0$). One finds the current maximum $|I_0(0)|_{\text{max}} = 4.07 \mu\text{A}$ at the resonance frequency $f_r = 4.94712$ GHz. This resonance frequency differs from the bare resonance calculated with Eq. A.34 by 49.4212 MHz. The red points in Fig. A.8(a) are provided by the simulation software and match the analytic expression perfectly.

Fig. A.8(b) shows the absolute value of Eq. A.41 as a function of z at resonance. A current anti-node is generated at the shorted and a current node at the open end. Fig. A.8(c) provides a zoom-in of the open end regime. One observes a non-zero current exactly at the capacitance and different leak-out distances for $C_c = 10$ fF (blue) and $C_c = 20$ fF (orange) resulting in different resonance frequencies. However, this is only a qualitative statement, since the model is only valid within the resonator ($-l \leq z \leq 0$).

B Fitting routines

B.1. Resonance curve fitting

Changing the flux biasing in the graphene rf SQUID coupled to the $\lambda/4$ -resonator influences the resonant behavior of the circuit as seen in the reflectance curve maps presented in Ch. 5.3. We implement a fitting routine, which is taking into account both the amplitude and the argument of Γ at once to insure a highly robust fitting procedure. An other advantage of the method is the clear distinction between the coupling quality factor Q_c and the effective quality factor Q_e . In the following we consider the resonance curve obtained at $I_{\text{flux}} = -74 \mu\text{A}$. From Fig. B.1(a) we observe that $|\Gamma|$ has a shallow asymmetric lineshape and from Fig. B.1(b) we observe that $\arg(\Gamma)$ develops a 2π -jump. In the IQ -plane, where $I = \text{Re}(|\Gamma|e^{j \arg(\Gamma)})$ and $Q = \text{Im}(|\Gamma|e^{j \arg(\Gamma)})$, the resonance curve generates here a circle surrounding the IQ -point $= (0,0)$ as shown in Fig. B.1(c). We fit both $|\Gamma|$ and $\arg(\Gamma)$ simultaneously with a least-square method with following combination of formulas [132]

$$\Gamma = \left[\frac{\Gamma_{\min} + 2jQ \frac{f-f_0}{f_0}}{1 + 2jQ \frac{f-f_0}{f_0}} - 1 \right] e^{j\phi} + 1, \quad (\text{B.1})$$

where $\Gamma_{\min} = \frac{Q_c - Q_e}{Q_c + Q_e}$ is the minimal reflection coefficient in the symmetric case ($\phi = 0$), $Q = (Q_c^{-1} + Q_e^{-1})^{-1}$ is the total quality factor, $Q_e = (Q_i^{-1} + Q_{\text{load}}^{-1})^{-1}$ is the effective quality factor, in which Q_{load} is the quality factor of the load, f is the probe frequency, f_0 is the resonance frequency and ϕ is the asymmetry angle, which causes a rotation of the resonance circle in the IQ -plane around the off-resonance point. In order to account for an offset and a slope in $|\Gamma|$ as well as in $\arg(\Gamma)$, we make use of following expression, which together with Eq. B.1 provides the complete fitting formula:

$$\Gamma_{\text{fit}} = |\Gamma| \cdot [a_{\text{off}} + a_{\text{slope}}(f - f_0)] \cdot e^{j[\arg(\Gamma) + p_{\text{off}} + p_{\text{slope}}(f - f_0)]}, \quad (\text{B.2})$$

where a_{off} describes an offset in the amplitude, a_{slope} describes a slope in the amplitude, p_{off} describes an offset in the argument and p_{slope} describes a slope in the argument. In Fig. B.1 the fit result (solid red) is overlain with the measurement data (blue crosses) and the complete set of fitting parameters is listed in Tab. B.1

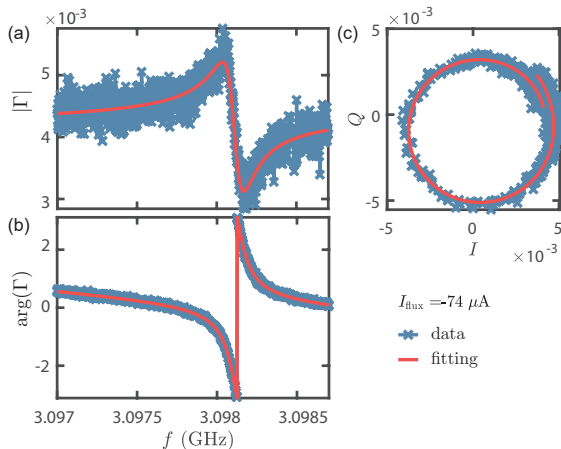


Figure B.1. Reflective response at $I_{\text{flux}} = -74 \mu\text{A}$ and $V_{\text{bg}} = 5 \text{V}$. (a)-(b) Resonance curve in $|\Gamma|$ and $\arg(\Gamma)$ as a function of probe frequency f . (c) Resonance curve in the I Q -plane. (a)-(c) The measured data is shown as blue crosses, while the fit result is presented as solid red line.

f_0	ϕ	Q_c	Q_e
3.0981 GHz	0.25 rad	23 800	669 800
a_{off}	a_{slope}	p_{off}	p_{slope}
4.3×10^{-3}	$5.1 \times 10^{-11} / \text{Hz}$	0.16 rad	$-4.7 \times 10^{-7} \text{ rad/Hz}$

Table B.1. Fit results at $I_{\text{flux}} = -74 \mu\text{A}$ and $V_{\text{bg}} = 5 \text{V}$. In the top the resonance frequency f_0 , asymmetry angle ϕ , coupling quality factor Q_c and effective quality factor Q_e . At the bottom the background offset and slope in the amplitude (a) and argument (p).

B.2. Curve fitting with screening correction

Following routine to correct the rf SQUID response for screening was developed together with Gergő Fülöp. Using Eqs. 5.5, 5.6 and 5.7 from Ch. 5.4, we express the shifted resonance frequency f_0 as a function of the junction phase φ ,

$$f_0(\varphi) = \left[\frac{8}{\pi^2} \frac{M^2}{L_p \left(\left(\frac{2\pi}{\Phi_0} \sum_{k=1}^{k_{\max}} (-1)^{k-1} A_k k \cos(k\varphi) \right)^{-1} + L_{\text{loop}} \right)} + 1 \right] f_{\text{bare}}. \quad (\text{B.3})$$

We fix the values of $M = 30.83$ pH, $L_{\text{loop}} = 211$ pH and $L_p = 4.546$ nH obtained from simulations, and treat A_k and f_{bare} as free fitting parameters. In the absence of current in the rf SQUID loop, the junction phase φ is solely determined by the external magnetic flux Φ in the loop, $\varphi = \varphi_{\text{ext}} = 2\pi\Phi/\Phi_0$. Taking into account the flux created by the circulating DC supercurrent yields

$$\varphi = \varphi_{\text{ext}} - \frac{2\pi}{\Phi_0} L_{\text{loop}} I_s(\varphi). \quad (\text{B.4})$$

This means, that the junction phase φ depends on the external flux and the CPR to-be-determined as well.

In the experiment the resonance frequency f_0 is measured as a function of the current in the flux line. Using the periodicity of the signal, we convert the flux current to the external phase φ_{ext} by applying a linear transformation. Next, to determine the CPR from the $(f_0, \varphi_{\text{ext}})$ data while taking into account the flux contribution of the supercurrent, we find the self-consistent solution of Eqs. B.3 and B.4 with an iterative method. The scheme is presented with the pseudocode in Algorithm 1. Essentially, it combines fixed-point iteration with Eq. B.4 and least-square fits to Eq. B.3. The procedure realizes the non-linear transformation of φ_{ext} to φ , and outputs the harmonic coefficients A_k and the bare resonance frequency f_{bare} .

Algorithm 1. Iterative procedure for curve fitting with screening correction

```

function FITWITHSCREENING( $f_0, \varphi_{\text{ext}}; M, L_p, L_{\text{loop}}, n_{\text{iter}} = 30, \alpha = 0.2 -$ 
 $0.4, k_{\max} = 10)$ 
   $\varphi = \varphi_{\text{ext}}$  ▷ Initialization
  for  $n_{\text{iter}}$  repetitions do
     $A_k, f_{\text{bare}} \leftarrow$  least-square fit of  $(f_0, \varphi)$  data points to Eq.B.3
     $I_s(\varphi) = \sum_{k=1}^{k_{\max}} (-1)^{k-1} A_k \sin(k\varphi)$  ▷ Substitution of  $A_k$  into Eq. 5.7
     $\varphi^{\text{new}} = \varphi_{\text{ext}} - 2\pi/\Phi_0 \cdot L_{\text{loop}} I_s(\varphi)$  ▷ Substitution of  $I_s$  into Eq. B.4
     $\varphi = \alpha\varphi^{\text{new}} + (1 - \alpha)\varphi$  ▷ Smooth update
  end for
  return  $A_k, f_{\text{bare}}, \varphi$ 
end function

```

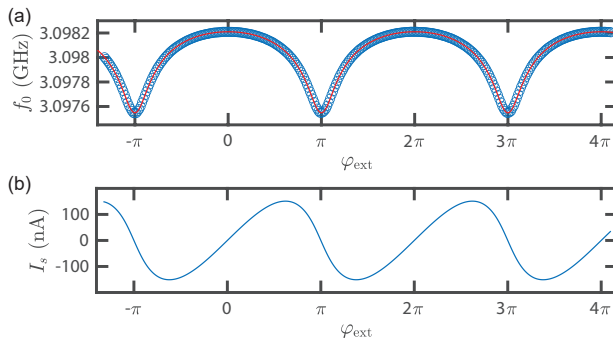


Figure B.2. (a) Measured resonance frequency f_0 (blue circles) as a function of external phase φ_{ext} at $V_{\text{bg}} = 6$ V. From the fit (solid red, Eq. B.3) one obtains the supercurrent $I_s(\varphi_{\text{ext}})$ as a function of external phase shown in (b).

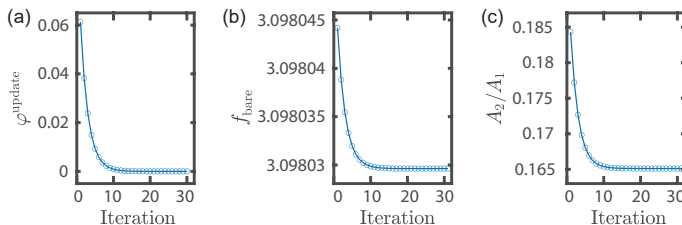


Figure B.3. Convergence of the iterative curve fitting method ($V_g = 6$ V, $\alpha = 0.4$). (a) The magnitude of the phase update, $\varphi^{\text{update}} = \langle |\varphi^{\text{new}} - \varphi| \rangle_{\text{avg}}$ converges to zero as the iteration progresses. (b-c) Convergence of the bare resonance frequency f_{bare} and the harmonic coefficient ratio A_2/A_1 .

In the following we illustrate the fitting routine with the experimental data obtained at $V_{\text{bg}} = 6$ V. In Fig. B.2 the initialization is shown, whereas the iteration and the outcome of the algorithm is illustrated in Figs. B.3-B.4. The convergence of the procedure has been checked manually for each gate voltage. The correctness of the final f_{bare} can be proven by the vanishing background slope in the CPR deduced by integrating the Josephson inductance L_J (obtained by directly solving Eq. 5.5) according to Eq. 5.6. Depending on the values of M and L_{loop} , manual tuning of the smoothing parameter α was necessary.

Figs. B.3(c) and B.4(c) show that neglecting the flux contribution of the supercurrent, and using the approximation $\varphi = \varphi_{\text{ext}}$ leads to overestimating the skewness of the CPR. While the apparent skewness parameter in this approx-

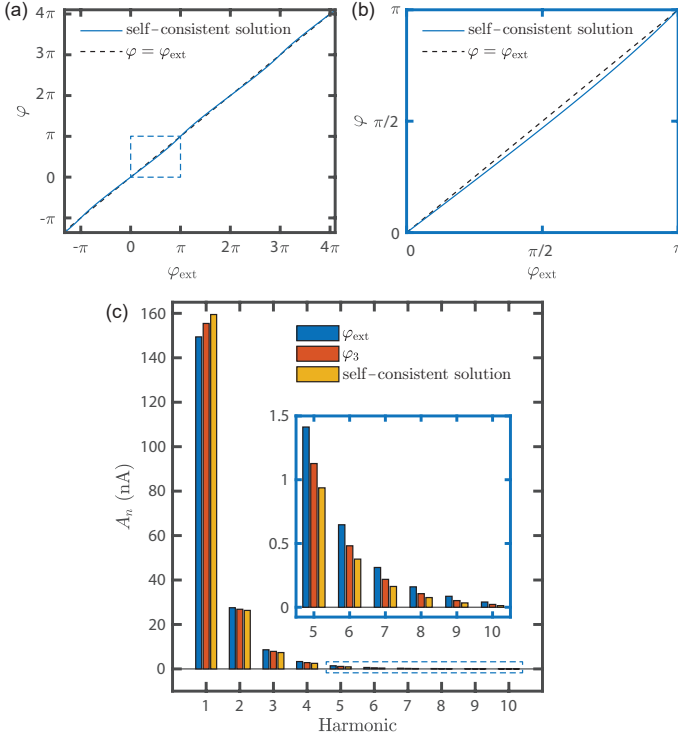


Figure B.4. Outcome of the iterative curve fitting method ($V_{\text{bg}} = 6$ V) (a-b) Junction phase φ as a function of the external phase $\varphi_{\text{ext}} = 2\pi\Phi/\Phi_0$. The self-consistent solution of the equation set (continuous, blue) deviates from the $\varphi = \varphi_{\text{ext}}$ line (dashed black). (c) Harmonic coefficients A_k at different stages of the iteration: initial solution (corresponding to the $\varphi = \varphi_{\text{ext}}$ approximation), solution at $n_{\text{iter}} = 3$ and $n_{\text{iter}} = 30$ (converged).

imation is $S_{\text{ext}} = 0.2434$, the self-consistent solution yields $S = 0.2168$. Similarly, the harmonic coefficient ratio reduces from $A_2/A_1 \approx 0.185$ to $A_2/A_1 \approx 0.165$ as the iteration converges.

C Temperature dependence of an rf SQUID

C.1. Theoretical predication

We numerically solve the time-dependent Usadel equation [117, 172], from which we infer the inductive B_J and dissipative G_s microwave response of short, diffusive Josephson junction. The theoretical predictions are based on characteristic energy scales: The electronic temperature T , the photonic energy irradiating on the junction hf , the relaxation rate γ , the superconducting gap Δ and the Thouless energy E_T .

In Fig. C.1, we fix $\Delta/E_T = 0.1$ and $hf/E_T = 0.01$. On the left axis the dissipative response normalized with the normal state conductance G_s/G_N is plotted (solid blue lines) and on the right axis the inductive response normalized with the normal state conductance B_J/G_N is plotted (dashed red lines).

In Fig. C.1(a) we fix $\gamma/E_T = 0.02$, while we sweep the temperature ratio kT/E_T . The wide onset of the dissipation peak even at low temperatures is mainly due to the non-vanishing relaxation ratio γ/E_T causing lifetime broadening of the ABS spectrum. With increasing temperature the conductance peak shrinks and becomes wider due to the dynamics of the thermally populated E_n^+ states. Additionally, a plateau like feature turning into a double wall can be recognized at $\varphi = \pi$. From the susceptance we observe that the conditions for $B_J/G_N = 0$ are moving away from $\varphi = \pi$ for increasing temperature and the absolute values of B_J/G_N at $\varphi = \pi$ and $\varphi = 0, 2\pi$ approach each other, which means that the CPR is becoming more sinusoidal.

For comparison we present in Fig. C.1(b) the numerical results for fixing $kT/E_T = 0.008$, while sweeping the relaxation ratio γ/E_T . We recognize a less evident change of the dissipation peak center as compared to the temperature sweep. Overall the conductance peak broadens accompanied with a shrinking of the height. Importantly, here the susceptance reveals as well a reduction of the CPR skewness. Note, that this plot is the same as Fig. 5.8(d), but globally normalized with G_N . Since the temperature effect seems to evolve differently from the relaxation rate dependence – both of these parameters should be accessible by comparing theoretical predictions with experimental data.

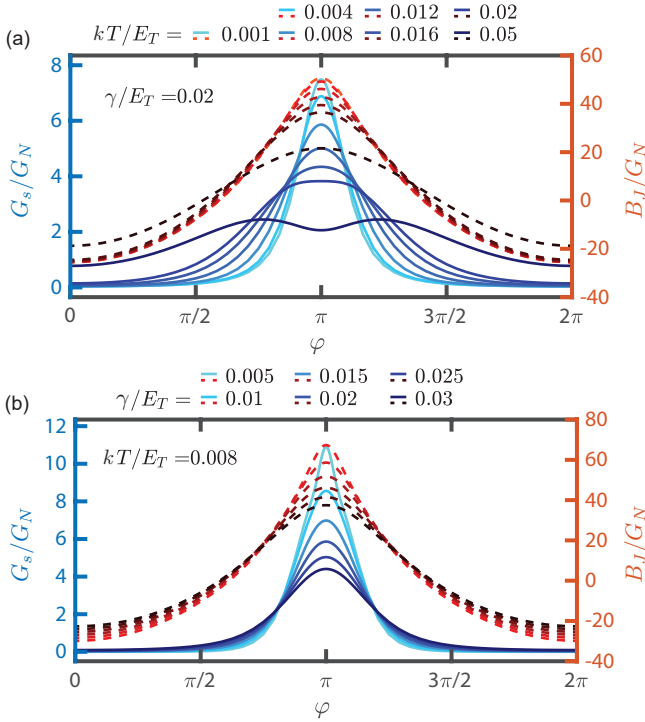


Figure C.1. Numerical simulations of the shunt conductance G_s/G_N and junction susceptance B_J/G_N both normalized with the normal state conductance G_N . Fixed parameters $\Delta/E_T = 0.1$ and $hf/E_T = 0.01$. (a) Dissipative (left) and inductive (right) microwave response for different temperatures but fixed relaxation rate. (b) Dissipative (left) and inductive (right) microwave response for different relaxation rates but fixed temperature.

C.2. Experimental results

From theory it is predicted that for increasing the temperature T the current-phase relation (CPR) becomes more and more sinusoidal, which is due to the balancing between E_n^+ - and E_n^- -states described by the Fermi-Dirac distribution. The population of E_n^+ -states further decrease the absorptivity of the ABS spectrum for bimodal channel transparency distribution. As a consequence the dissipation peak becomes smaller.

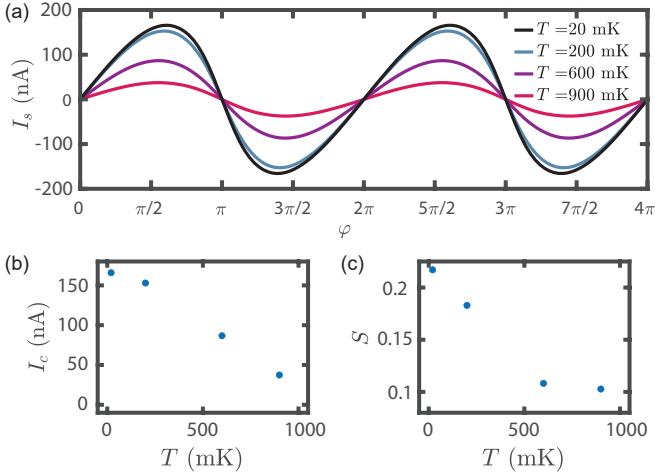


Figure C.2. Temperature T dependence at $V_{\text{bg}} = 12$ V. (a) Self-consistent CPR for different temperatures (see legend). (b) Critical current I_c as a function of T . (c) Skewness parameter S as a function of T .

In the following we probe the microwave response of the graphene JJ presented in Ch. 5 in terms of the CPR and the phase-dependent dissipation at $V_{\text{bg}} = 12$ V for different temperatures. We deduce the CPR and the shunt conductance with the same methods described above and in the maintext. In Fig. C.3(a) we illustrate the self-consistent CPR solution for different base temperatures adjusted by heating the mixing chamber plate. We observe a clearly skewed CPR for temperatures far below the critical temperature of Al ($T_c \approx 1.2$ K), while for $T \rightarrow T_c$ the skewness as well as the critical current I_c decreases as present separately in Figs. C.3(b) and C.3(c). These effects are attributed to: i) the washing out of the energetically low lying states (close to $E = 0$), which are responsible for the skewness due to their high transparency and ii) the closing of the superconducting gap. Measurements for $T > 900$ mK were suffering from strong temperature fluctuations.

As postulated by theory we obtain a counter-intuitive decreasing of the dissipations peak for increasing temperatures as seen in Fig. C.3(d). Not only the height is influenced by the temperature, but also the width, which is also a result from the theoretical predictions. We fit the different dissipation peaks with a Lorentzian function of the form $L = \frac{a(b/2)^2}{(\varphi-c)^2 + (b/2)^2} + d$, where a is a scaler for the peak height, b is the full-width-half-maximum (FWHM), c is a translation on the phase-axis and d describes a vertical offset. We find that

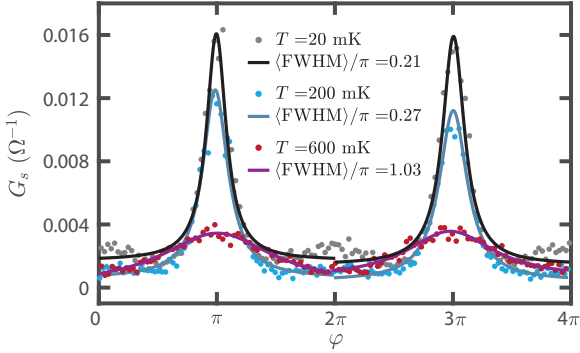


Figure C.3. Phase-dependent dissipation at different T for $V_{\text{bg}} = 12$ V. The peaks are fitted with Lorentzian function, which reveals a clear spreading of the width for increasing T .

the averaged FWHM of the two peaks measured at the same temperature is increasing $\langle \text{FWHM} \rangle \approx 0.2\pi \rightarrow \pi$ for temperatures $T = 20 \rightarrow 600$ mK, while the peak height shrinks by a factor of ~ 3 .

In contrast to the low temperature results shown in Ch. 5, we did not find combinations of kT/E_T and γ/E_T , which simultaneously reproduce the inductive and dissipative response. We attribute this to the finite parameter space used in the simulation. In order to describe the microwave behavior of the JJ at high temperatures – effects like highly enhanced relaxation rates, modifications in junction length limit and the gap closing would need to be considered.

D Extracting the charge carrier density

This chapter was mainly written by David Indolese and added for completeness. To convert the applied back gate voltage (V_{bg}) to charge carrier density (n_g) we used a plate capacitor model including the quantum capacitance of graphene [173], which results in

$$e(V_{\text{bg}} + V_{\text{off}}) = \frac{e^2 n_g d}{\epsilon_0 \epsilon_r} + \text{sgn}(n_g) \hbar v_F \sqrt{\pi |n_g|}, \quad (\text{D.1})$$

where $V_{\text{off}} = 0.44 \text{ V}$ is the offset voltage of the charge neutrality point with respect to 0 V, e is the electron charge, $d = 47.5 \text{ nm}$ the thickness of the gate dielectric, $\epsilon_0 = 8.854 \times 10^{-12} \text{ F/m}$ the vacuum permittivity, $\epsilon_r = 3.8$ the dielectric constant of hBN [174], \hbar the reduced Planck constant, and $v_F = 10^6 \text{ m/s}$ the Fermi velocity of graphene. The quantum capacitance corresponding to the second term on the right hand side of Eq.D.1 leads to minor deviations of the linear behavior on n_g with respect to V_{bg} around charge neutrality, as shown in Fig.D.1 (a). By using Eq.D.1 the previously extracted critical current $I_c(V_{\text{bg}})$ is plotted as a function of n_g in Fig. D.1 (b).

In previous works oscillations of $I_c(n_g)$ were observed for negative densities for high mobility and ballistic graphene Josephson junctions [175, 176]. They arise due to quantum interference of the electrons moving in a Fabry-Pérot cavity [177], which is formed by potential steps in the graphene. Namely, the

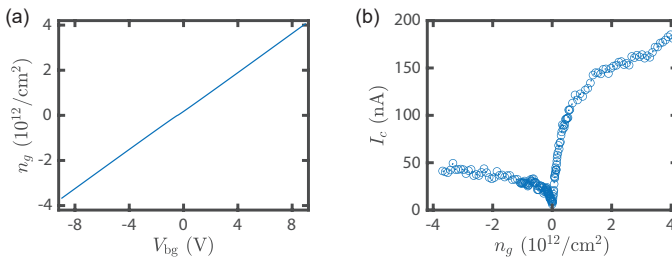


Figure D.1. (a) Charge carrier density n_g determined with Eq.D.1 as function of gate voltage V_{bg} . (b) Critical current I_c as function of n_g .

graphene is n' -doped with electrons close to the contacts given by the work function mismatch of the graphene and the Al boundary, while the bulk of graphene is p -doped with holes due to the negative applied V_{bg} . The oscillations show their m^{th} maxima at $\sqrt{n_g} = m\sqrt{\pi}/L$, where L corresponds to the length of the cavity. Nevertheless, no such oscillations were observed in our measurement of $I_c(n_g)$, which indicates that the electron transport is diffusive in our sample.

D